

(Award No.:AOARD-06-4066)

# FINAL REPORT

## DEVELOPMENT OF HEALTH MONITORING TECHNIQUES FOR COMPOSITE STRUCTURES

By Professor Hisao Fukunaga and Dr. Ning Hu

Department of Aerospace Engineering, Tohoku University,  
Aramaki-Aza-Aoba 6-6-01, Aoba-ku, Sendai 980-8579, Japan

### Abstract

The purpose of this project is to develop two kinds of composite structural health monitoring approaches. **One** is a “**passive element**” based on the impact force identification combined with a database. This database can quickly evaluate the impact-induced damages in composites by employing the identified impact force. It can be built up by using a powerful numerical model for impact damage evaluation with the help of experimental data. **Another** is an “**active element**” based on the Lamb wave. These two stable and reliable structural health monitoring techniques can then be used to more practical situations. The majority of the aims of this project have been successfully achieved. The major achievements of our group have been the following: 1) an efficient impact force identification technique without resort to numerical models has been developed; 2) a powerful numerical model based on the finite element method for predicting the impact-induced damages has been built up; 3) a Lamb wave based on structural health monitoring technique without baseline data has been developed which is used in metallic and composite structures

Report Documentation Page				Form Approved OMB No. 0704-0188	
Public reporting burden for the collection of information is estimated to average 1 hour per response, including the time for reviewing instructions, searching existing data sources, gathering and maintaining the data needed, and completing and reviewing the collection of information. Send comments regarding this burden estimate or any other aspect of this collection of information, including suggestions for reducing this burden, to Washington Headquarters Services, Directorate for Information Operations and Reports, 1215 Jefferson Davis Highway, Suite 1204, Arlington VA 22202-4302. Respondents should be aware that notwithstanding any other provision of law, no person shall be subject to a penalty for failing to comply with a collection of information if it does not display a currently valid OMB control number.					
1. REPORT DATE <b>07 NOV 2007</b>		2. REPORT TYPE		3. DATES COVERED	
4. TITLE AND SUBTITLE <b>Strcutrual Health Monitoring (SHM)</b>				5a. CONTRACT NUMBER <b>FA48690610076</b>	
				5b. GRANT NUMBER	
				5c. PROGRAM ELEMENT NUMBER	
6. AUTHOR(S) <b>Hisao Fukunaga</b>				5d. PROJECT NUMBER	
				5e. TASK NUMBER	
				5f. WORK UNIT NUMBER	
7. PERFORMING ORGANIZATION NAME(S) AND ADDRESS(ES) <b>Department of Aaerospace Engineering,Aramaki-aoba 6-6-01, Aoba-ku,Sendai ,jp,980-8579</b>				8. PERFORMING ORGANIZATION REPORT NUMBER <b>N/A</b>	
9. SPONSORING/MONITORING AGENCY NAME(S) AND ADDRESS(ES)				10. SPONSOR/MONITOR'S ACRONYM(S)	
				11. SPONSOR/MONITOR'S REPORT NUMBER(S)	
12. DISTRIBUTION/AVAILABILITY STATEMENT <b>Approved for public release; distribution unlimited.</b>					
13. SUPPLEMENTARY NOTES					
14. ABSTRACT <b>The purpose of this project is to develop two kinds of composite structural health monitoring approaches. One is a passive element based on the impact force identification combined with a database. This database can quickly evaluate the impact-induced damages in composites by employing the identified impact force. It can be built up by using a powerful numerical model for impact damage evaluation with the help of experimental data. Another is an active element based on the Lamb wave. These two stable and reliable structural health monitoring techniques can then be used to more practical situations. The majority of the aims of this project have been successfully achieved. The major achievements of our group have been the following: 1) an efficient impact force identification technique without resort to numerical models has been developed; 2) a powerful numerical model based on the finite element method for predicting the impact-induced damages has been built up; 3) a Lamb wave based on structural health monitoring technique without baseline data has been developed which is used in metallic and composite structures</b>					
15. SUBJECT TERMS					
16. SECURITY CLASSIFICATION OF:			17. LIMITATION OF ABSTRACT	18. NUMBER OF PAGES <b>152</b>	19a. NAME OF RESPONSIBLE PERSON
a. REPORT <b>unclassified</b>	b. ABSTRACT <b>unclassified</b>	c. THIS PAGE <b>unclassified</b>			

## Introduction

Over the last two decades, the techniques of structural health monitoring (SHM) have drawn much attention of people in academic and engineering fields. Although there have been a lot of improvements in this field, most of works have been limited to laboratory-scope testing for some simple specimens. There are a number of challenges for effective applications on practical structures, for example, the sensitivity, the simplicity, the stability and the robustness of current techniques are questionable. These challenges form an obvious gap between the current studies and their final applications to practical structures in operating states.

Here, the main purpose of the present research is to propose a new kind of system using strain-type sensors, such as PZT, to increase the sensitivity, stability and robustness of SHM. Our proposed system involves two elements which possesses “Active” and “Passive” characteristics when using the same sensor and actuator network.

### **1. “Passive” element: a stable health monitoring technique based on the identification of impact loads acting on structures and a reliable database of damage evaluation**

This element possesses a new concept for SHM, which basically includes two important research contents: (1) the identification method of external impact loads acting on structures; (2) a database for damage evaluation, which is constructed from the experimental data and effective theoretical or numerical models. This database can connect the identified impact force to the defined damage index or extent of structures with the help of some important structural and material properties, which can finally lead to effective evaluation of CAI strength. This system is schematically shown in Fig. 1.

Our achievements on this topic can be summarized in the following two aspects:

#### **1.1 Highly accurate identification of impact force history and impact force location**

Modern techniques of structural health monitoring are a possible resort to insure the safety of composite structures. The identification of the external impact forces is important for structural health monitoring and has been investigated by many researchers [1-8]. For instance, Wu *et al.* [1] reported the identification results of impact forces on various plates based on the relation between the impact force and the strain response. Seydel *et al.* [2] identified the location and history of the impact force acting on stiffened composite panels. The authors [3-8] proposed a technique to identify the location and history of impact forces based on a finite element method. However, it is difficult to construct a precise analytical model on complicated structures such as aircraft wings and fuselages. Then it is important to develop the impact force identification method using only experimental data *without resort to an analytical or numerical model* [9-10]. The present work examines an experimental identification method of impact

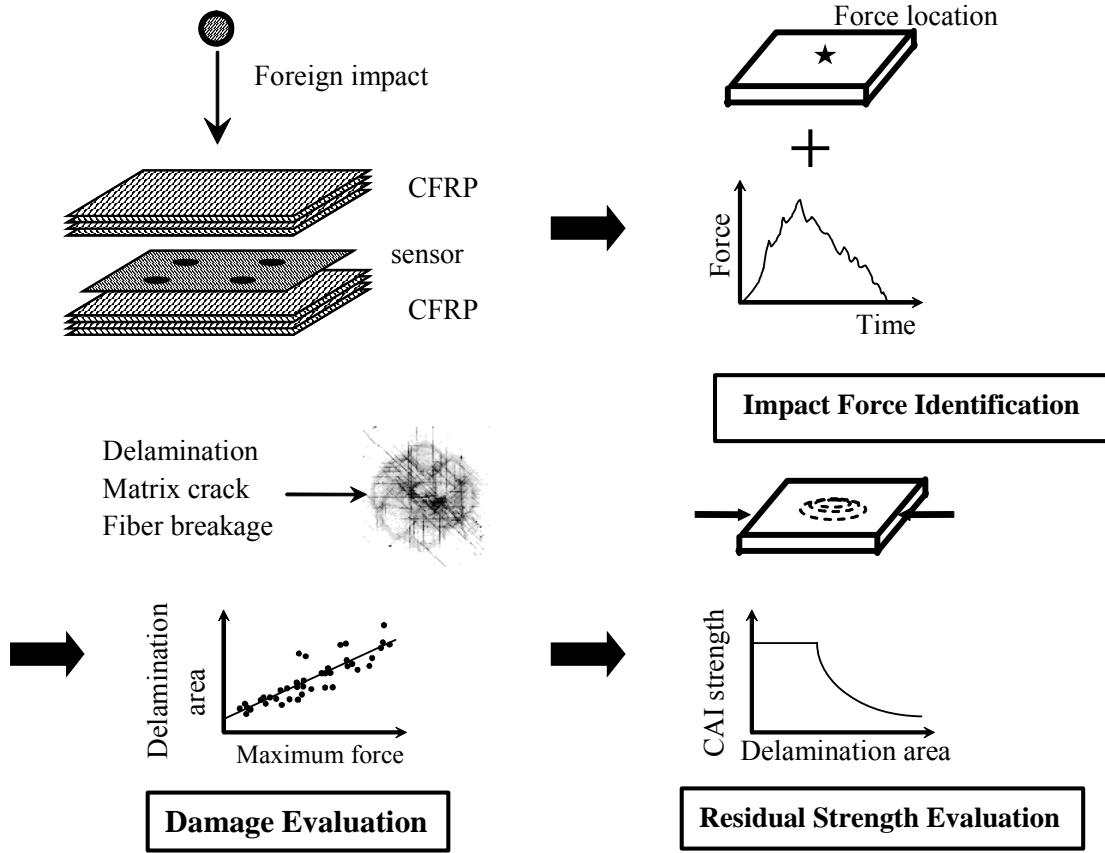


Figure 1. Schematic view of damage monitoring.

forces acting on CFRP structures. The key idea in this research is to construct the experimental relation between force histories and strain responses, i.e., the transfer functions, which is first determined by using measured force histories and the corresponding strain responses. The location and history of impact force is identified based on this relation. The validity of the present identification method has been verified through an impact test of a CFRP flat plate and a CFRP stiffened panel with an impulse hammer. The method is also applied to a drop-weight impact test of CFRP laminated plates involving impact damages.

### 1.1.1 Impact Force Identification of CFRP Stiffened Panel

#### a. Method

In a low-velocity impact event on a plate, the relation between an impact force history acting at the location  $(x_f, y_f)$  and a strain response observed at the location  $(x_o, y_o)$  can be expressed in the following algebraic equation:

$$\{\tilde{\varepsilon}\} = [G(x_f, y_f, x_o, y_o)]\{\tilde{f}\} \quad (1)$$

where the strain and force histories are expressed at a discrete time, and  $[G(x_f, y_f, x_o, y_o)]$  is a transform matrix composed of the Green's function at each time, which is a lower triangular matrix [1] as follows:

$$\begin{Bmatrix} \varepsilon_1 \\ \varepsilon_2 \\ \varepsilon_3 \\ \vdots \\ \varepsilon_n \end{Bmatrix} = \begin{bmatrix} g_1 & & & & \\ g_2 & g_1 & & & 0 \\ g_3 & g_2 & g_1 & & \\ \vdots & \vdots & \vdots & \ddots & \\ g_n & g_{n-1} & g_{n-2} & \cdots & g_1 \end{bmatrix} \begin{Bmatrix} f_1 \\ f_2 \\ f_3 \\ \vdots \\ f_n \end{Bmatrix} \quad (2)$$

where  $g_i$  is a component of a transform matrix which is determined by the force location and the observation point of strain only, and is not influenced by the force history.

Eq. 2 is then transformed into the following equation:

$$\begin{Bmatrix} \varepsilon_1 \\ \varepsilon_2 \\ \varepsilon_3 \\ \vdots \\ \varepsilon_n \end{Bmatrix} = \begin{bmatrix} f_1 & & & & \\ f_2 & f_1 & & & 0 \\ f_3 & f_2 & f_1 & & \\ \vdots & \vdots & \vdots & \ddots & \\ f_n & f_{n-1} & f_{n-2} & \cdots & f_1 \end{bmatrix} \begin{Bmatrix} g_1 \\ g_2 \\ g_3 \\ \vdots \\ g_n \end{Bmatrix} \quad (3)$$

Eqs. 2 and 3 can be expressed as follows:

$$\{\tilde{\varepsilon}\} \equiv [G]\{\tilde{f}\} = [F]\{g\} \quad (4)$$

The components of a transform matrix,  $\{g\}$ , is determined using the force histories  $\{\tilde{f}\}$  and measured strain responses  $\{\tilde{\varepsilon}\}$  in an impact test with an impulse hammer. Several times of tests are performed to avoid measurement errors in the determination of  $\{g\}$ . Then the components of the transform matrix can be obtained by applying the least-squares method [7]:

$$\underset{\{g\}}{\text{minimize}} H = \sum_{k=1}^K \|\{\tilde{\varepsilon}\} - [F]\{g\}\|^2 \quad (5)$$

As the transform matrix in Eq. 1 is determined, the impact force acting on CFRP plates is determined using measured strains at the multi-point PZT sensors in the case of that the force location is known [3, 6]. The force history can be identified using a minimization problem as follows:

$$\begin{aligned}
& \underset{\{\tilde{f}\}}{\text{minimize}} & F = \sum_{i=1}^m \|\{\tilde{\varepsilon}_i\} - [G_i]\{\tilde{f}\}\|^2 \\
& \text{subject to} & \{\tilde{f}\} \geq 0
\end{aligned} \tag{6}$$

where  $\{\tilde{\varepsilon}_i\}$  is the strain responses measured by the  $i$ -th sensor located at  $(x_{oi}, y_{oi})$ ,  $[G_i]$  is the transform matrix relating  $\{\tilde{\varepsilon}_i\}$  to  $\{\tilde{f}\}$ , and  $m$  is the number of sensors. The constraint in Eq. 6 is to ensure the force to be compressive all the time. Then the force history identification is achieved by solving Eq. 7 by means of the quadratic programming method in this study.

Another issue is the determination of the force location. In the force history identification at the assumed location  $(x_e, y_e)$ , we can have a force history denoted by  $\{\tilde{f}_e\}$ . Then an error vector, which indicates the deviation between the estimated strains and measured strains, can be defined. The force location is determined by solving a minimization problem as follows:

$$\underset{x_e, y_e}{\text{minimize}} \quad E = \sum_{i=1}^m \frac{\|[G_i]\{\tilde{f}_e\} - \{\tilde{\varepsilon}_i\}\|^2}{\|\{\tilde{\varepsilon}_i\}\|^2} \tag{7}$$

Eq. 7 is solved by a nonlinear programming method [11]. In the minimization process, the force history  $\{\tilde{f}_e\}$  is updated using Eq. 7 for each force location.

### b. Example 1 (CFRP flat plate)

To verify the identification method stated in the previous section, we consider a cantilever CFRP composite plate [9]. The material properties of CFRP plate are shown in Table. 1. The impact test system consists of a measurement part and identification codes as shown in Fig. 2. The former part consists of a sensor network and several signal conditioners. The present study utilizes the SMART Layer developed in Stanford University as a part of the sensor network as

Table 1. Material properties of CFRP plates

Stacking sequence	Material properties of unidirectional lamina
[45 <sub>2</sub> /-45 <sub>4</sub> /45 <sub>2</sub> ] <sub>s</sub>	$E_1 = 114 \text{ GPa}$ , $E_2 = 9.20 \text{ GPa}$
[0 <sub>2</sub> /45 <sub>2</sub> /-45 <sub>2</sub> /90 <sub>2</sub> ] <sub>s</sub>	$G_{12} = 5.49 \text{ GPa}$
	$\nu_{12} = 0.30$ , $\rho = 1550 \text{ kg/m}^3$

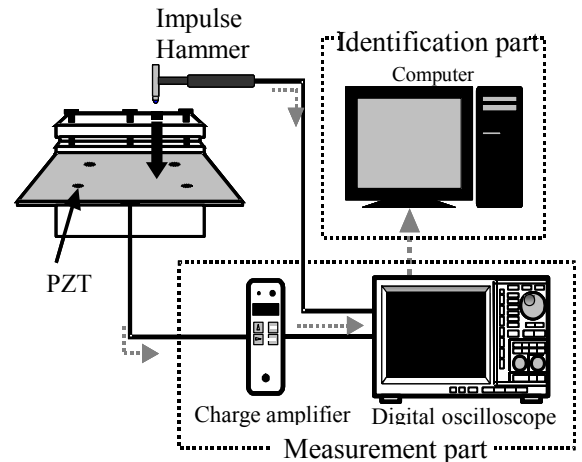


Figure 2. Impact test system

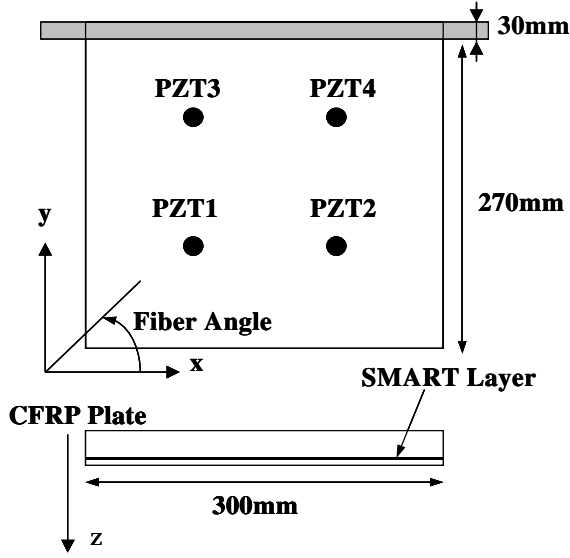


Figure 3. CFRP specimen with PZT sheet

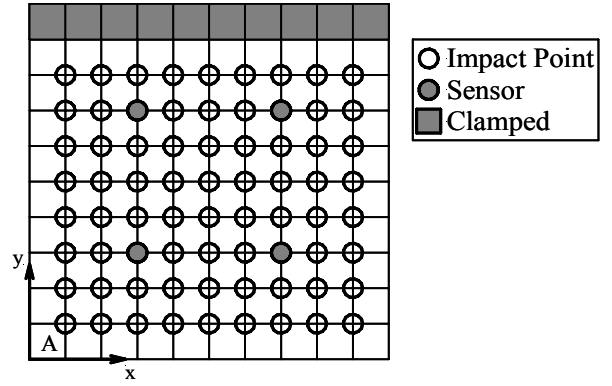
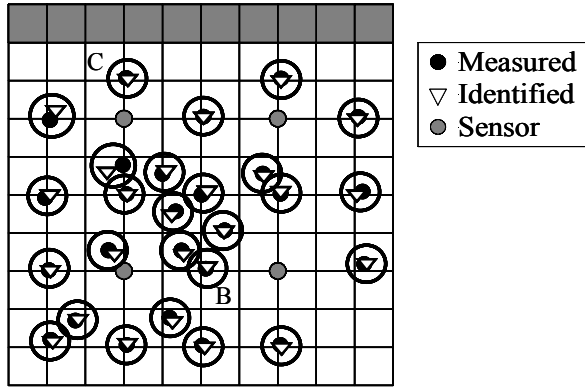
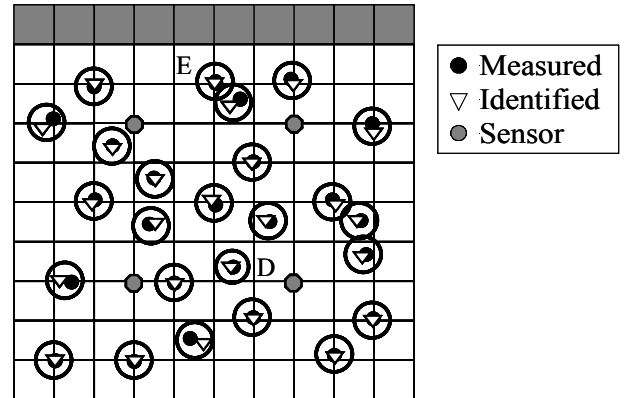


Figure 4. Impact points used to determine a transform matrix



(a)  $[45_2/-45_4/45_2]_s$  laminate

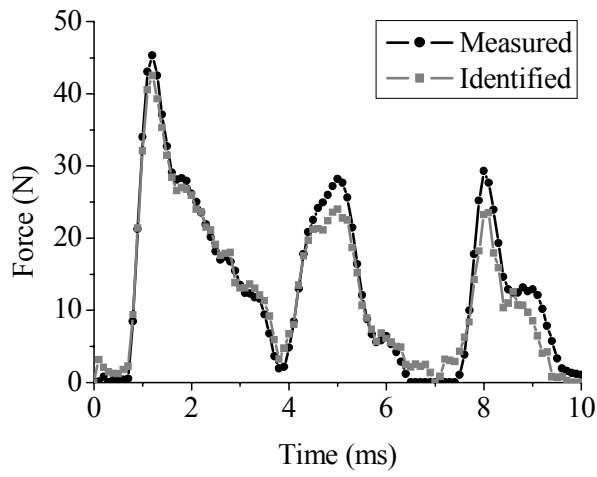


(b)  $[0_2/45_2/-45_2/90_2]_s$  laminate

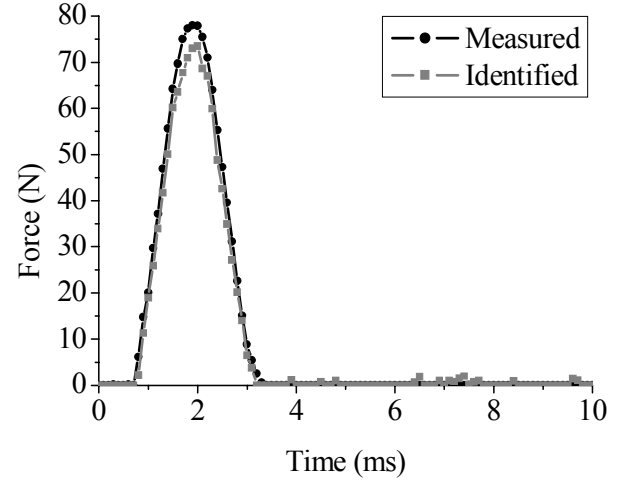
Figure 5. Identified force locations for CFRP laminated plates

shown in Fig. 3. Figure 4 shows the impact points used to determine the transform matrix in Eq. 1 where the number of sensors is 4. The transform matrix is constructed for each combination of impact point and sensor point through four times of impact tests with an impulse hammer. The components in the transform matrix at impact points are used to obtain the information of an arbitrary position using a shape function similar to one used in a finite element method.

The impact force is identified using the output of four PZT sensors embedded in CFRP laminates. The force location is determined by Eq. 7. Figure 5 shows the identification results of the force location for  $[45_2/-45_4/45_2]_s$  laminate and  $[0_2/45_2/-45_2/90_2]_s$  laminate. In Fig. 5, each circle involves the true (measured) and identified force locations. The average errors of the



(a) Point B

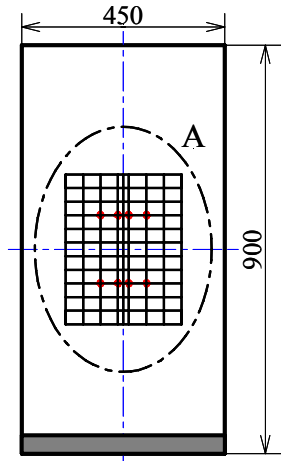


(b) Point C

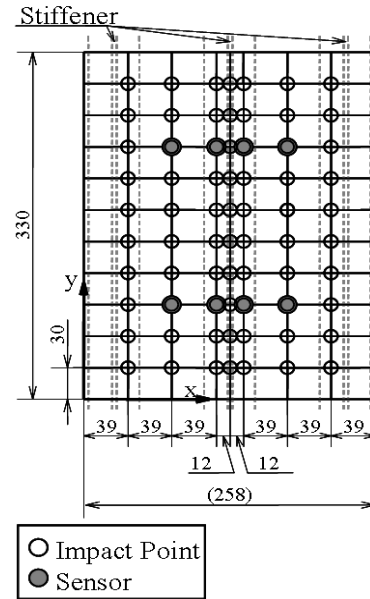
Figure 6. Identified force histories for  $[45_2/-45_4/45_2]_s$  laminate

Table 2. Laminate sequence of CFRP stiffened panel.

Laminate Sequence	
Stiffener	Skin
$[45/-45/-45/45/0_4/90/45_3]_s$	$[45/-45/-45/45/0/90]_s$



a) CFRP stiffened panel



(b) impact points and sensor locations  
(enlargement of the region A in (a))

Figure 7. Impact test of CFRP stiffened panel.

force location were 2.7 mm for  $[45_2/-45_4/45_2]_s$  laminate and 3.1 mm for  $[0_2/45_2/-45_2/90_2]_s$  laminate, respectively. These are around 1% of the plate size in length. The location error in the



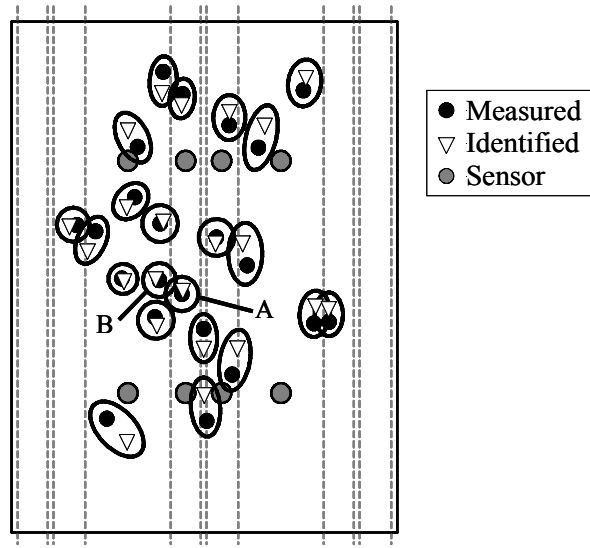


Figure 8. Identified force location for CFRP stiffened panel.

present method is smaller compared with 8.5 mm for  $[45_2/-45_4/45_2]_s$  laminate and 4.1 mm for  $[0_2/45_2/-45_2/90_2]_s$  laminate in the previous method based on FEM modeling [4] since the present method can avoid the modeling error in the construction of the transform matrix.

Figure 6 shows the identified force histories at the points B and C for  $[45_2/-45_4/45_2]_s$  plate in Fig. 5(a), respectively. In these cases, the force locations are identified near the true ones, and therefore the identified force histories agree well with the true ones.

### c. Example 2 (CFRP stiffened panel under single loading)

The second example is a Carbon/PEEK stiffened panel. The impact test for Carbon/PEEK stiffened panel has been performed as shown in Fig. 7. The impact point the sensor location are also shown in Fig. 7(b) where the impact point with the impulse hammer is located at the skin side

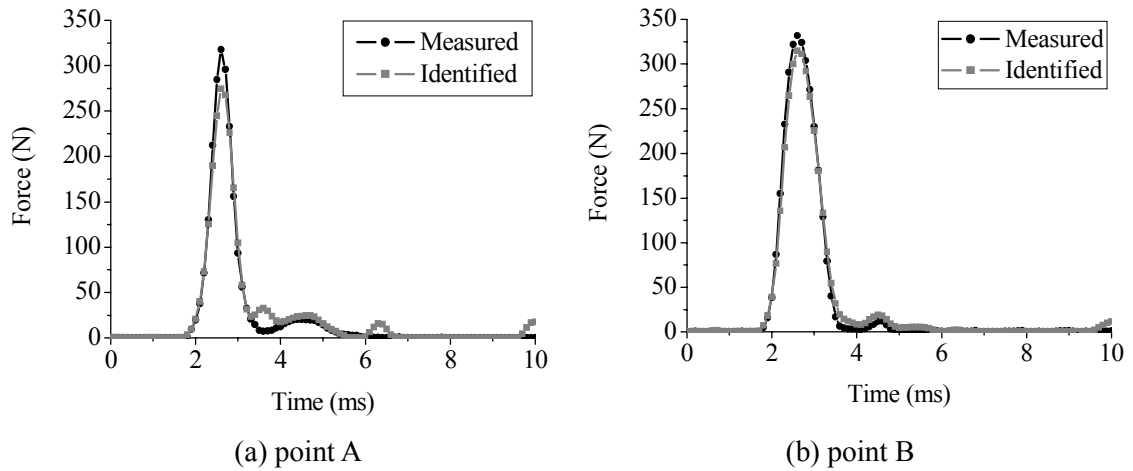


Figure 9. Identified force histories for CFRP stiffened panel.

and the strain responses are measured by using 8 biaxial strain gauges attached on the surface of the stiffener side. The transform matrix is determined using the measured force histories and strain responses in an impact test with an impulse hammer. Table 2 shows laminate sequence of the stiffener and skin in the stiffened panel.

Figure 8 shows the identification results of the force location. Each circle involves the true (measured) and identified force locations. The average errors of the force location were 9.2 mm. The location error at the point A with the stiffener is 11.5mm and that at the point B without the stiffener is 3.2mm. The difference of location errors with and without the stiffener is not so large. Figure 9 shows the identified force histories in the case of points A and B for CFRP stiffened panel in Fig. 8. The identification error of force history at the point A is a little large since the location error is relatively large. On the contrary, the identification error of force history at the point B is small, and the force history as well as the force location is accurately identified.

#### d. Example 3 (CFRP stiffened panel under multiple loading)

The above method can be easily extended into the cases of multiple-loading [10]. We consider the impact force identification for Carbon/Epoxy stiffened panel under multiple loading as shown in Fig. 10. The stiffened panel is clamped at the upper and lower edges. The sensor

Table 3. Laminate sequence

Skin	$[-45/0/45/90_2/-45/0/45/90]_s$
Flange	$[(-45/90/45/0/-45/90_2/45/90)_s/(-45/90/45)_s]$
Web	$[(-45/90/45/0/-45/90_2/45/90)_s]_s$

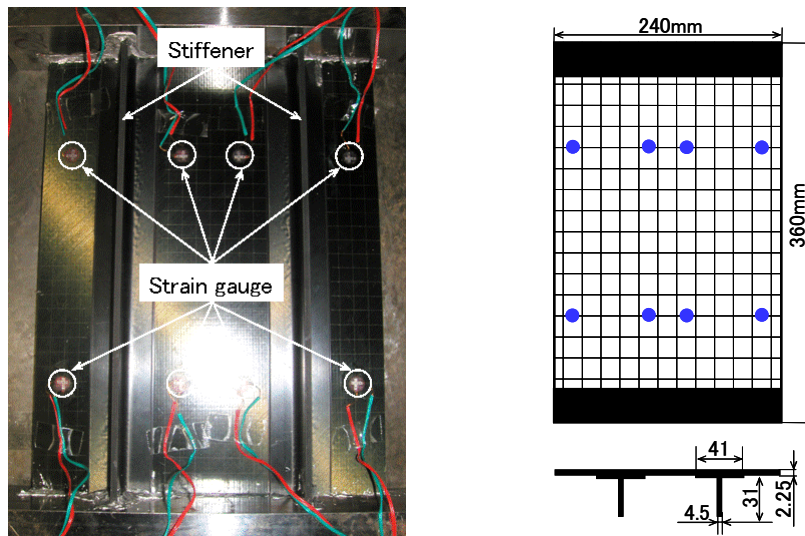


Figure 10. Carbon/Epoxy stiffened panel.

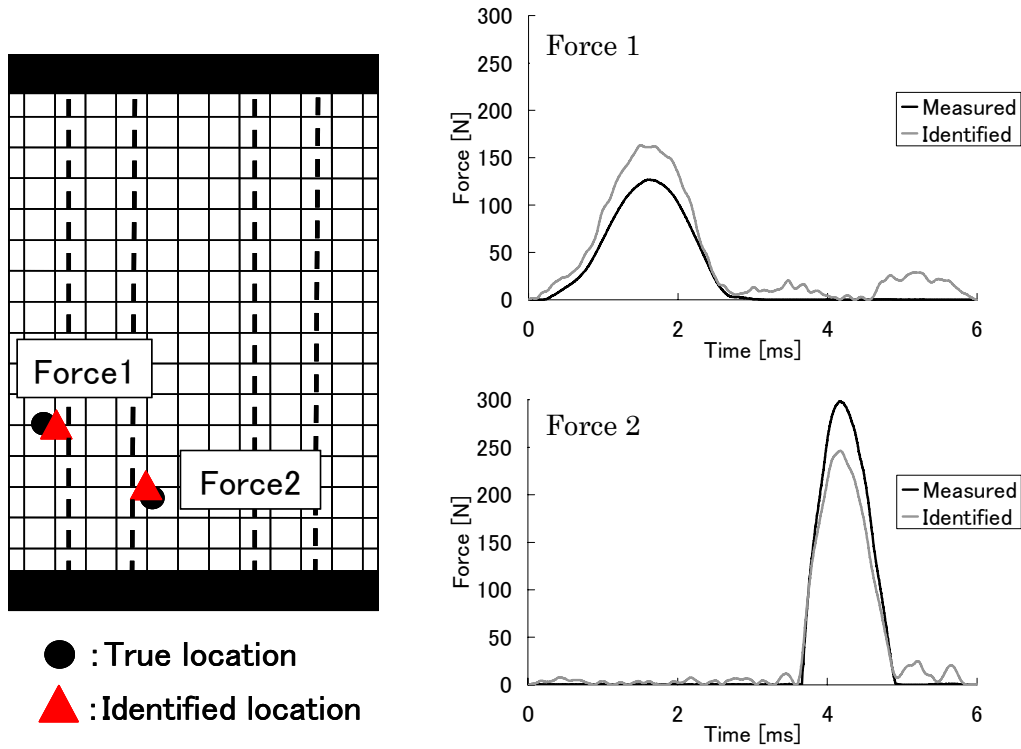


Figure 11. Identification results for case 1.

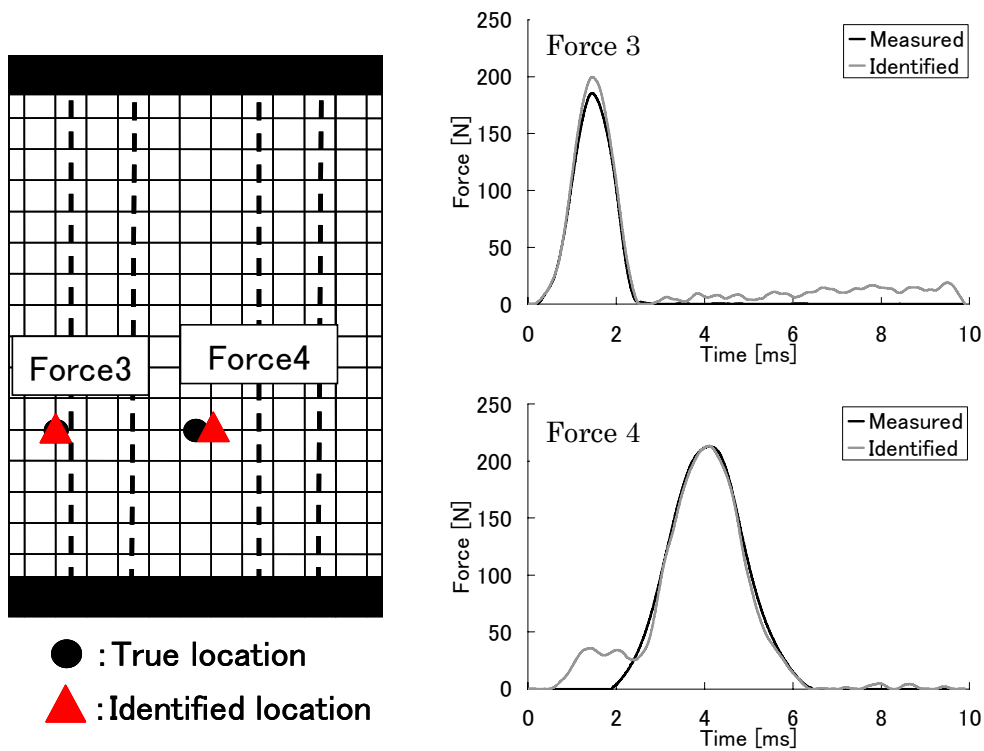


Figure 12. Identification results for case 2.

location is shown in Fig. 10 where the strain responses are measured by using 8 biaxial strain gauges attached on the surface of the stiffener side. The transform matrix is determined using the measured force histories and strain responses in an impact test with an impulse hammer. Table 3 shows laminate sequence of the stiffener and skin in the stiffened panel.

In the present impact test, we consider the two-point loading with impulse hammer, and two kinds of impactors are used as tip materials of impulse hammer, i.e., hard tip (aluminum) and soft-tip (plastic). Hard-tip impulse hammer is used to determine the transform matrix. In the two-point loading, two types of tip materials are used in order to examine the effect of tip stiffness on the force identification results as follows:

Case 1 : hard-tip + hard-tip

Case 2 : hard-tip + soft-tip

Figure 11 shows the identification results for the case 1 where the force location and the force histories of two loading, i.e., force 1 and force 2 are shown. The errors of the force location were 8.1mm for force 1 and 9.9mm for force 2. The errors of the maximum force were 29% for force 1 and 17% for force 2. The force location and the force histories are identified well although the results are not so good as compared with the single loading case. Figure 12 shows the identification results for the case 2 where the tip materials of impulse hammer with the different stiffness are used. The errors of the force location were 0.0mm for force 3 and 5.0mm for force 4. The errors of the maximum force were 8% for force 3 and 0% for force 4. The case 2 gives the better results both for the force location and the force histories.

### 1.1.2 Impact Force Identification in Drop-Weight Impact Test

In the present identification method, we assume that there is no damage in structures, and

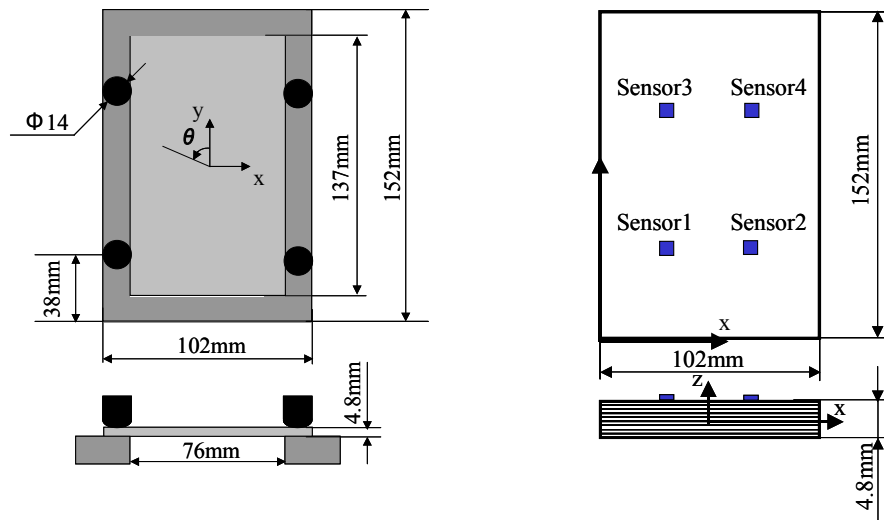


Figure 13. Specimen of drop-weight impact test.

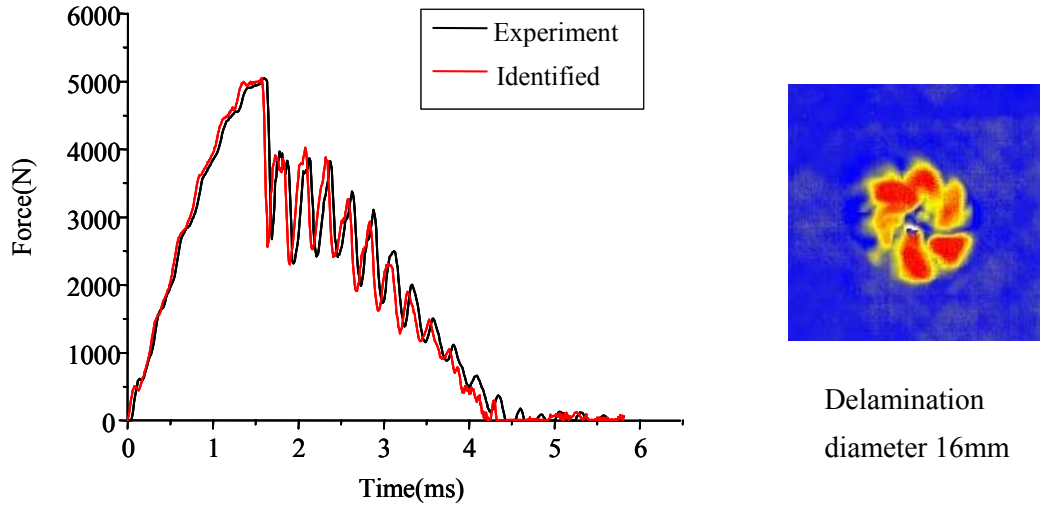


Figure 14. Identified force history for 4.8J impact energy.

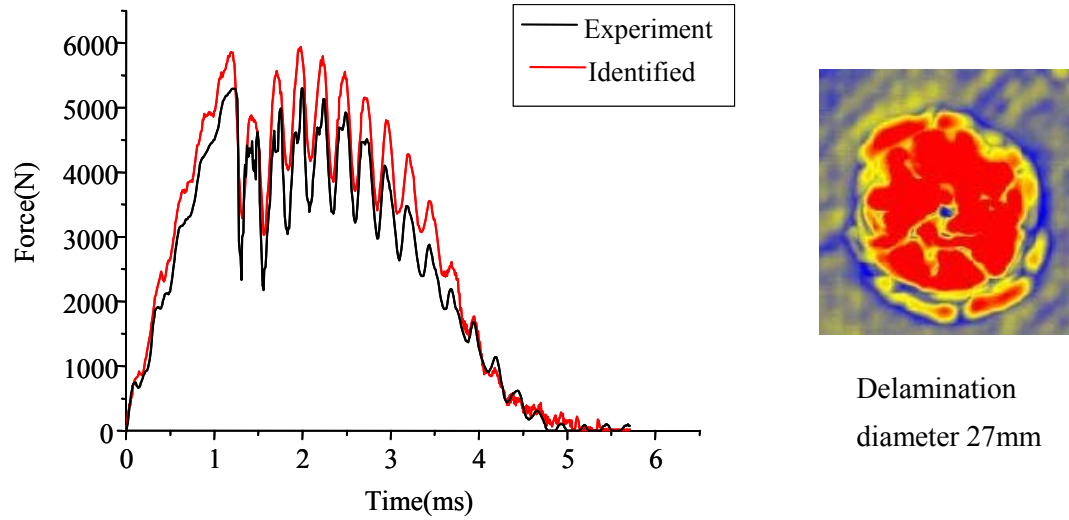


Figure 15. Identified force history for 7.2J impact energy.

we use a transform matrix of a healthy structure. The question is if this method is still valid for the cases where slight damages happen in practical cases. We consider the impact force identification in a drop-weight impact test where the impact damage such as delamination is induced within the laminate [8, 9].

Figure 13 shows the specimen of CFRP laminated plates used in drop-weight impact test where the laminate configuration of CFRP plates is  $[(45/0/-45/90)_4]_s$ , and the mass and the tip radius of an impactor is 4.7kg and 15.8mm, respectively. Four biaxial strain gauges are attached on the upper surface of the plate. As energy levels in an impact test, 3.0J, 4.8J and 7.2J were used where there was no damage in the laminate for the case of 3.0J impact energy. By employing the experimental transform matrix for the impact case of 3.0J, the impact force is identified using measured strains for the impact cases of 4.8J and 7.2J.

Figures 14 and 15 show the identified impact force histories for 4.8J and 7.2J cases, respectively. The identified force histories agree well with the true ones. The damage area by ultrasonic C-scan is also shown in the figures. The diameter of the damage area is 16mm for 4.8J case and 27mm for 7.2 J case, respectively, and is not so large in both cases. When impact damage is not so severe and the damage extent is not so large, we can identify the force history using a transform matrix of a healthy structure.

In this work, the experimental identification method of the impact force location and force history has been developed. The validity of the present method has been verified through impact tests for the CFRP flat plates and the stiffened panel, and a drop-weight impact test of CFRP laminated plates. The knowledge from these results is summarized as follows:

- (1) The accurate force location and force history can be identified using the present experimental identification method for both of CFRP flat plate and stiffened panel.
- (2) The present force identification method is based on the experimental transform matrix to relate the impact force and the measured strain. Thus the method can be applicable easily to complicated structures such as composite wing and fuselage structures.
- (3) The present force identification method is also effective for the cases of multiple-loading.
- (4) The present force identification method using a transform matrix of a healthy structure can be applicable to the case of that a small size of impact damage is induced.

Real-time monitoring of the impact events is very important for structural health monitoring. The present method of the force identification effectively predicts the location and history of the impact force acting on composite structures. The developed system takes a few seconds to identify the location and history for each case. Almost identification time is consumed in the force location identification. Therefore, we can get the information of impact events in real time. Once we can know the location and history of the impact force, we can evaluate the impact-induced damages as well as residual strength as shown in Fig. 1, using an analytical or experimental database of CFRP structures.

## Reference

1. E. Wu, J. C. Yeh and C. S. Yen. Identification of Impact Forces at Multiple Locations on Laminated Plates. *AIAA J.*, 32(12), 2433-2439, 1994.
2. R. Seydel and F. K. Chang. Impact Identification of Stiffened Composite Panels. *Smart Mater. Struct.*, 10, 354-369 & 370-379, 2001.
3. H. Fukunaga and N. Hu. Health Monitoring of Composite Structures Based on Impact Force Identification. *Proc. Second European Workshop on Structural Health Monitoring 2004*, C.

- Boller and W. J. Staszewski ed., DES Tech Pub., pp. 415-422, 2004.
4. M. Tajima, S. Matsumoto and H. Fukunaga. Impact Force Identification of CFRP Laminated Plates Using PZT Piezoelectric Sensors. *Trans. Japan Soc. Mech. Eng., Part A*, 70, 1566-1573 & 1747-1754 (in Japanese), 2004.
  5. N. Hu and H. Fukunaga. A New Approach for Health Monitoring of Composite Structures through Identification of Impact Force. *J. Advanced Science*, 17, 82-89, 2005.
  6. N. Hu, H. Fukunaga, S. Matsumoto, B. Yan and X. H. Peng. An Efficient Approach for Identifying Impact Force Using Embedded Piezoelectric Sensors. *Int. J. Impact Engineering*, 34, 1258-1271, 2007.
  7. Fukunaga, H. and N. Hu. Experimental Impact Force Identification of Composite Structures. *Proc. Third European Workshop on Structural Health Monitoring 2006*, A. Guemes ed., DES Tech Pub., pp. 840-847, 2006.
  8. N. Hu, S. Matsumoto, R. Nishi and H. Fukunaga. Identification of Impact Forces on Composite Structures Using an Inverse Approach. *STRUCTURAL ENGINEERING AND MECHANICS, An International Journal* (in press).
  9. M. Tajima, N. Hu and H. Fukunaga. Experimental impact force identification of CFRP stiffened panels. *Proc. of ICCM16, 223104 CD-ROM*, 2007.
  10. H. Fukunaga, T. Umino and N. Hu. Impact force identification of CFRP stiffened panel under multiple loading. *Int. Workshop on Structural Health Monitoring*, 2007 (in press).
  11. G. N. Vanderplaats and H. Sugimoto. A general purpose optimization program for engineering design. *Computers Structures*, 24, 13-21, 1986.

## 1.2 Highly accurate damage evaluation of CFRP under impact loads based on FEM

After obtaining the impact force, the second step is to determine the possible material damages caused by the impact event in this “Passive” element of structural health monitoring. To finish this step of the damage evaluation, a database which connects some important features of the impact force (such as maximum impact force) and the damage extents should be built up. This database will be constructed by using the experimental data and an efficient numerical model based on the finite element method. The numerical method for predicting the impact-induced damages will be described in this section.

It is well known that very complicated damage phenomena occur in composite laminated structures under the transverse impact loads. Generally, there are two main categories of various damages in composite laminates under the transverse impact loads. The first category consists of various kinds of in-plane damages, such as fiber failure and transverse matrix cracking etc. The second category includes the interface damages, i.e. delaminations between multiple

laminae, which are the dominant damages of laminates under transverse loads.

To predict the delaminations in laminates, some authors have proposed various stress-based criteria. For example, Brewer and Lagace [1] proposed a delamination criterion. Hou *et al.* [2] further modified this delamination criterion by taking into account the interaction between the out-of-plane compression and interlaminar shear. From many previous studies, it has been concluded that the stress-based criteria are enough to predict the initiation of various damages, especially for in-plane damages, such as fiber failure and matrix cracking. However, as pointed out by Davies and Zhang [3], in the stress-based criteria for delamination, the scale effects would not be exhibited as in a fracture model. To predict the delamination size or propagation, it almost certainly requires an energy release rate algorithm based on the knowledge of fracture mechanics. Besides the above stress-based criteria, some methods based on fracture mechanics have also been proposed. For instance, in Refs [4-6], the strain energy released rate of the mixed-mode at the delamination front is directly evaluated and used to predict the delamination propagation. However, this kind of methods cannot deal with the initiation of delaminations, therefore, some initial pre-existing small delamination areas are needed to be assumed. Furthermore, cohesive interface models, which can tackle the initiation and propagation of delamination simultaneously, are widely used to simulate the delamination propagation due to their inherent simplicity and efficiency [7-11]. However, when using comparatively coarse cohesive elements to simulate the interface damage propagations, such as delamination propagation, there are some very strong numerical instabilities [7-11]. Especially for those interfaces with high strength and high initial stiffness, this problem becomes more obvious when using coarse meshes. Some techniques have been proposed to date [11, 12] in which the artificial external work has been introduced into the computational process. In this work, we propose a new cohesive model termed as Adaptive Cohesive Model (ACM), which can overcome the drawbacks of previous techniques and stabilize the computational process [13].

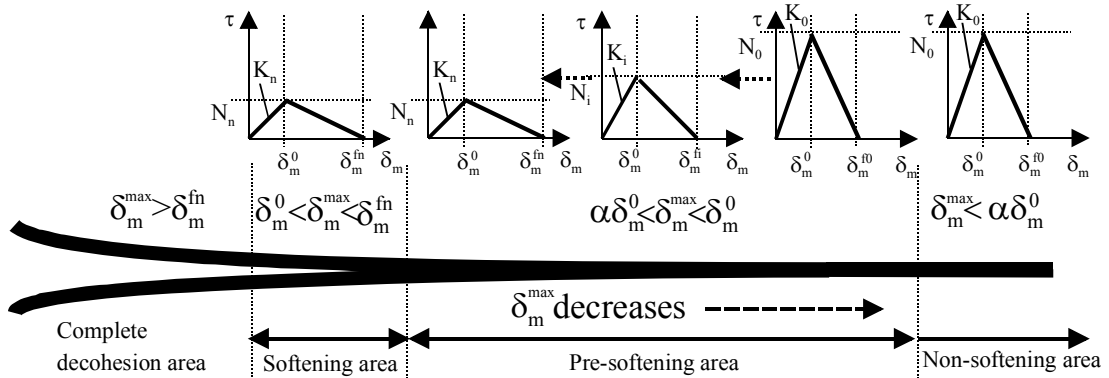


Figure 16. Schematic view of adaptive cohesive model ( $\alpha=0\sim1.0$ ).



### a. Method

As shown in Fig. 16, to stably simulate delamination propagations in composite laminates under transverse impact loads when using comparatively coarse cohesive elements for reducing the computational cost. In this model, in front of the original softening zone located at the delamination tip, we set up another pre-softening zone. In this pre-softening zone, with the increase of effective relative displacements, the initial stiffness of cohesive elements is gradually reduced as the interface strength decreases.

In Fig. 16, the interface stiffness  $K$  and the interface strength, e.g.,  $N$  for Mode I [7], are linearly reduced with the increase of relative opening displacement, i.e.,  $\delta_m^{\max}$  as follows

$$N_i = \frac{\delta_m^{\max}}{\delta_m^0} (N_{\min} - N_0) + N_0, \quad (N_0 > N_{\min}) \quad \text{and} \quad (\alpha \delta_m^0 < \delta_m^{\max} < \delta_m^0) \quad (8a)$$

$$K_i = \frac{\delta_m^{\max}}{\delta_m^0} (K_{\min} - K_0) + K_0, \quad (K_0 > K_{\min}) \quad \text{and} \quad (\alpha \delta_m^0 < \delta_m^{\max} < \delta_m^0) \quad (8b)$$

where  $N_0$  is the initial interface strength,  $N_{\min}$  the lower limit of interface strength,  $K_0$  the initial stiffness and  $K_{\min}$  is the lower limit of stiffness. It should be noted that  $\alpha$  in Eq. (8) is a parameter to define the size of pre-softening zone. When  $\alpha=1$ , the present ACM model degenerates into the traditional cohesive model.

Note that Eq. (8) also holds for  $S$  and  $T$  used in Mode II and III [7]. By choosing the proper ratio between the lower limits of strength and stiffness (e.g.,  $N_{\min}$  and  $K_{\min}$ ), from Eq. (8), the following relations can be realized easily:

$$\delta_3^0 = \frac{N_0}{K_0} = \frac{N_i(\delta_m^{\max})}{K_i(\delta_m^{\max})} = \frac{N_{\min}}{K_{\min}}, \quad \delta_2^0 = \delta_1^0 = \frac{S_0}{K_0} = \frac{S_i(\delta_m^{\max})}{K_i(\delta_m^{\max})} = \frac{S_{\min}}{K_{\min}} \quad (\text{for } S=T) \quad (9)$$

Therefore, from Eq. (9), the onset displacement  $\delta_m^0$  in the pre-softening zone is the same as that in the softening zone of the traditional cohesive model, which does change in the updating process of the interface stiffness and strength.

The fracture toughness of materials for determining the final displacement of complete decohesion is not changed. In the above adaptive model,  $N_0$  can be taken as the real interface strength. Therefore, it is crucial to define  $N_{\min}$  from the consideration of computational stabilization and accuracy. Here, by referring to this statement, for instance, for the case of Mode-I, the size of softening zone  $R$  was defined [8] as follows,

$$R = N_c R_n = \frac{\pi}{2} \frac{E_{\text{polymer}}}{1-\nu^2} \frac{G_{IC}}{N_{\min}^2} \quad (10)$$

where  $N_c$  is the number of elements in softening zone, which ranges from 2 to 5 from our

numerical experiences,  $R_n$  the element size, and  $E_{polymer}$  and  $\nu$  are the Young's modulus and Poisson's ratio of polymer.

Finally,  $N_{min}$ , which depends on the element size, can be calculated as follows,

$$N_{min} = \sqrt{\frac{\pi}{2} \frac{E_{polymer}}{1-\nu^2} \frac{G_{IC}}{N_c R_n}} \quad (11)$$

For the mixed mode, the similar formulation can be set up by simply replacing  $G_{IC}$  by  $G_c$ , which is equal to  $G_{IC} + (G_{IIC} - G_{IC}) \left( \frac{\beta^2}{1 + \beta^2} \right)^\eta$  [7].

The above ACM is of the engineering meaning when using coarse meshes for complex composite structures, which is, in fact, an '*artificial*' means for achieving the stable numerical simulation process. A reasonable explanation is that all numerical techniques are artificial, whose accuracy strongly depends on their mesh sizes, especially at the front of crack tip. To remove the factitious errors in the simulation results caused by the coarse mesh sizes in the numerical techniques, we artificially adjust some material properties in order to partially alleviate or remove the numerical errors. Otherwise, we have to resort very fine meshes, which may be computationally impractical for very complex problems from the capabilities of most current computers. Of course, the modified material parameters should be those which do not have the dominant influences on the physical phenomena. For example, the interface strength usually controls the initiation of interface cracks. However, it is not crucial for determining the crack propagation process and final crack size from the viewpoint of fracture mechanics. Moreover, there has been almost no clear rule to exactly determine the interface stiffness, which is a parameter determined with a high degree of freedom in practical cases. Therefore, the error caused by the modifications of interface strength and stiffness can be very small since the practically used onset displacement  $\delta_m^0$  for delamination initiation is remained constant in our model. For the parameters, which dominate the fracture phenomena, should be unchanged. For instance, in our model, the fracture toughness dominating the behaviors of interface damages is kept constant.

This cohesive model has been implemented in the explicit time integration scheme for evaluating the delamination propagations in composite laminates. Also, a stress-based criterion [14] is adopted for predicting various in-plane damages, such as matrix cracks, fiber breakage etc. Then, this numerical simulation method based on FEM is applied to the problems of DCB and CFRP laminated plates of 32 plies under transverse impact loads. To our best knowledge, till now, there has been successful numerical simulation for impact damages of laminates of 32 plies. The corresponding experiments of a drop-weight impact test have been carried out and the results are used to illustrate the validity of the present method.

### 1.2.1 A CFRP DCB problem

A DCB test specimen of a  $(0^\circ)_{24}$ , T300/977-2 carbon fiber-reinforced epoxy laminate, containing a thin insert at the mid-plane near the loaded end, is simulated (Camanho and Davila, 2002). As shown in Fig. 17, this specimen is 150 mm long, 20 mm wide, with two 1.98 mm thick plies, and with an initial crack length of 55 mm. The material properties are:  $E_{11}=150.0$  GPa,  $E_{22}=E_{33}=11.0$  GPa,  $G_{12}=G_{13}=6.0$  GPa,  $G_{23}=3.7$  GPa,  $\nu_{12}=\nu_{13}=0.25$ ,  $\nu_{23}=0.45$  and  $\rho=1444$  kg/m<sup>3</sup>. It is a static experiment [7]. As shown in Fig. 17, in our computations, the loading speed is taken as 10 mm/sec. From our numerical experiences, this low speed can yield sufficiently stable results without obvious inertia effects. Moreover, the tensile strength  $N$ , Mode-I fracture toughness  $G_{IC}$ , and the initial stiffness of cohesive zone  $K$  are defined in Table 4. The mesh size and predicted  $N_{\min}$  using Eq. (11) are listed in Table 5 when  $E_{\text{polymer}}=3.0$  GPa and  $N_c=3$  (three elements in softening zone). Note that  $\alpha=0$  in Fig. 16 is constantly used in all examples.

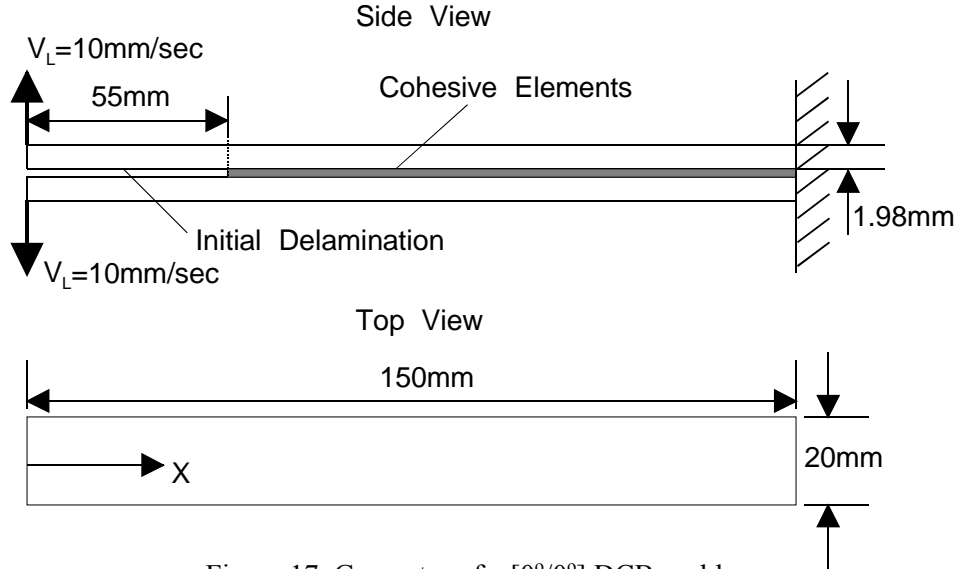


Figure 17. Geometry of a  $[0^\circ/0^\circ]$  DCB problem

Table 4. Properties of cohesive element

$N_0$	$K_0$	$G_{IC}$	$\delta_m^0$	$\delta_m^f$
(MPa)	(N/mm <sup>3</sup> )	(kJ/m <sup>2</sup> )	(mm)	(mm)
45	$3.0 \times 10^4$	0.378	0.0015	0.0119

Table 5. Mesh size and predicted  $N_{\min}$  in Eq. (11)

Mesh size $R_n$ (mm)	Initial $N_0 \rightarrow N_{\min}$ (MPa)
1.0	45.0 $\rightarrow$ 22.5
2.0	45.0 $\rightarrow$ 15.0

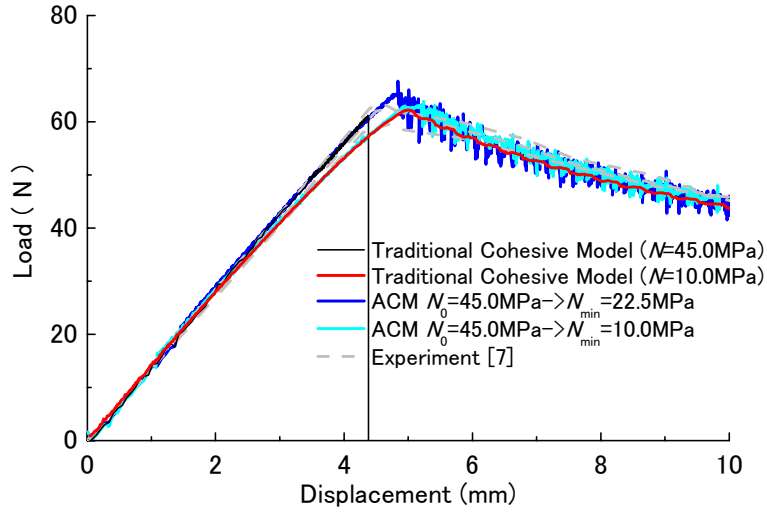


Figure 18. Results of traditional cohesive element, ACM and experiments (mesh size  $R_n=1$  mm)

The various results are shown in Figs 18 and 19 for cohesive mesh size of 1 mm. First, the comparison of the results of traditional cohesive element, ACM and experiment [7] is shown in Fig. 18 for the mesh size of 1mm. From it, we can find that when the practical interface strength is used in the traditional cohesive model, i.e., 45.0 MPa, the result of traditional cohesive model has a sudden stop and the computation is forcefully terminated due to very strong numerical instability. With the decrease of interface strength to 10.0 MPa in the traditional model, the result is very stable, however, the slope of loading curve before the peak load is obviously lower than those of experimental ones [7]. For the results of ACM, when  $N_{\min}$  is 22.5 MPa predicted by Eq. (11), very good result can be obtained by comparing with the experimental ones. However, when  $N_{\min}$  is taken as 10.0 MPa in ACM, the same result as that of traditional cohesive model of the

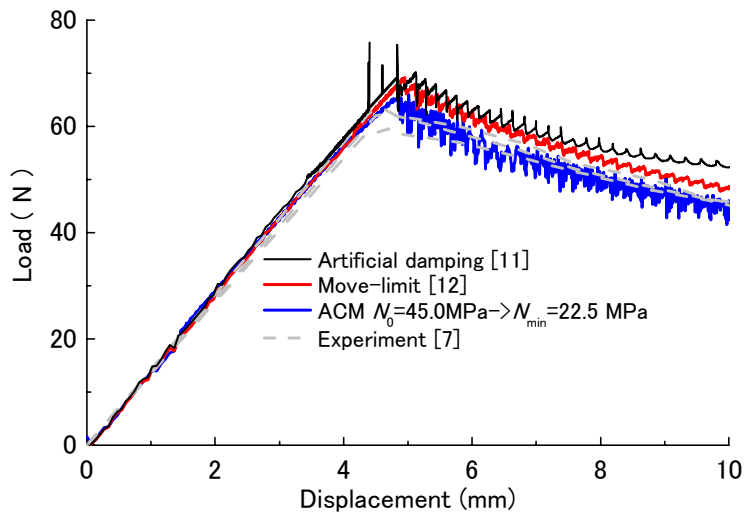


Figure 19. Results of traditional cohesive element, ACM and experiments (mesh size  $R_n=1$  mm)

same interface strength is obtained. In Fig. 19, the results of the artificial damping [11] and the move-limit technique [12] for stabilizing the numerical computations are plotted. From this figure, we can find that both techniques work stably, however, the peak loads predicted by these techniques are slightly higher than the experimental ones. However, in Fig. 19, the error in the peak load of ACM is much smaller than those predicted by the stabilization techniques [11,12]

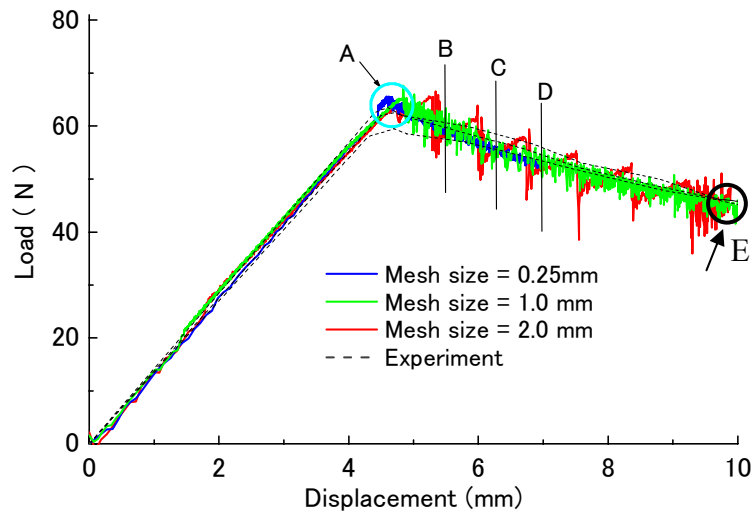


Figure 20. Comparison of load histories of different mesh sizes

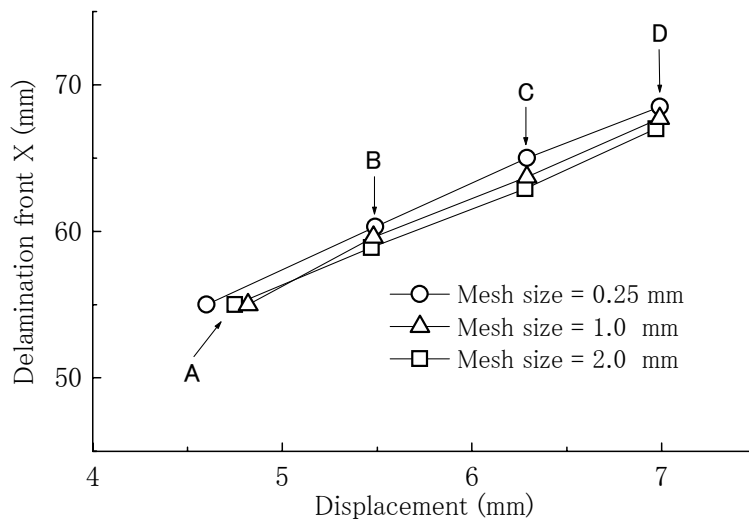


Figure 21. Comparison of positions of delamination tips of different mesh sizes

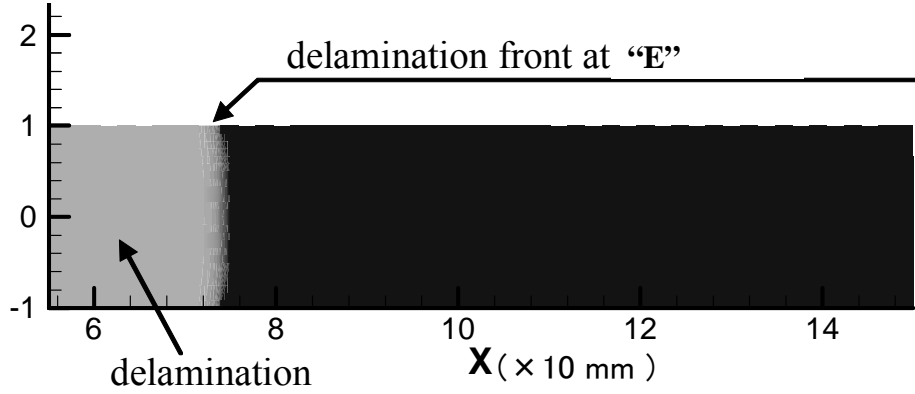


Figure 22. Delamination shape at the point E in Fig. 16

due to the proper decrease of interface stiffness. From the above discussions, we can find that ACM can yield very good results from the aspects of the peak load and the slope of loading curve if  $N_{\min}$  is properly defined.

The comparison of results obtained from the different mesh sizes is illustrated in Fig. 20. In this figure, it should be noted that for the case of mesh size of 0.25 mm, the conventional cohesive model can produce the stable and converged results. Only for the mesh sizes of 1 mm and 2 mm, the present ACM is employed. From this figure, it can be found that the different mesh sizes result in almost the same loading curves. For the different stages shown in Fig. 20, i.e. A, B, C and D, the delamination tip positions for various mesh sizes are shown in Fig. 21, which demonstrates that the delamination propagation speeds are almost the same for various mesh sizes. Finally, the correct and typical thumbnail delamination shape at the point E in Fig. 20 is shown in Fig. 22.

### 1.2.2 A CFRP plate under low-velocity impacts

The second example is a low-velocity impact problem, and the experiments are performed by the present authors using a weight-drop impact test machine of Dynatup 9250HD. The experimental setup is shown in Fig. 23. The specimens are prepared according to the SACMA standard of CAI test. As shown in Fig. 24, a quasi-isotropic CFRP laminated plate of 32 plies as  $[(45^\circ/0^\circ/-45^\circ/90^\circ)_4]_s$  is put on the bottom frame with four fixed points. This plate is impacted by an impacting body of a lower semi-spherical shape and the mass of 4.6kg. As shown in Table 6, we have performed 8 tests for 4 impact energy levels, i.e. 3.0J, 4.8J, 6.0J and 7.2J. Two tests have been carried out for each energy level. When the impact energy is 3.0J, there is no impact-induced damage in Table 6. It is interesting to note that for the impact energy of 4.8 J, the damages occur in one specimen, but does not occur in another one. Therefore, the impact energy of 4.8 J can be thought of as the threshold of impact energy, which induces the possible damages in CFRP laminates. When the impact energy is higher than 4.8 J, e.g., 6.0 J and 7.2 J, there are obvious

impact-induced damages in four specimens. The ultrasonic results of specimen after impact for these two energy levels will be shown later. From the ultrasonic results, it can be found that the damage area in the impacted side is larger than that of the opposite side of impact. Although the extent of the delamination is not quantified, it increases with depth and a typical conical shape is obtained with the top surface located close to the impact point.

First, in our numerical model, the following material properties of lamina of CF/Epoxy are used:  $E_1=135.0$  GPa,  $E_2=E_3=10.0$  GPa,  $G_{12}=G_{13}=5.50$  GPa,  $G_{23}=4.50$  GPa,  $\nu_{12}=0.0183$ ,  $\nu_{13}=0.45$ ,  $\nu_{23}=0.25$ ,  $\rho=1489$  kg/m<sup>3</sup>. Also, the properties for damage simulations are listed as follows:  $N_0=85.0$  MPa,  $S_0=T_0=106.0$  MPa,  $N_{\min}=76.5$  MPa,  $S_{\min}=T_{\min}=95.4$  MPa,  $G_{IC}=0.5$  kJ/m<sup>2</sup>,  $G_{IIC}=G_{IIIC}=1.0$  kJ/m<sup>2</sup>. To deal with the possible the in-plane damages, the strength parameters of CFRP material [12] are adopted. However, the fiber breakage has not been considered in the present model since from the experimental observations, no fiber breakage has been identified. Also, as shown in Fig. 25 for the indentation  $\alpha_c$  between a ball and a laminate, the modified Hertz contact law [14] is employed to deal with the contact between the ball and the laminate, which is listed as follows,

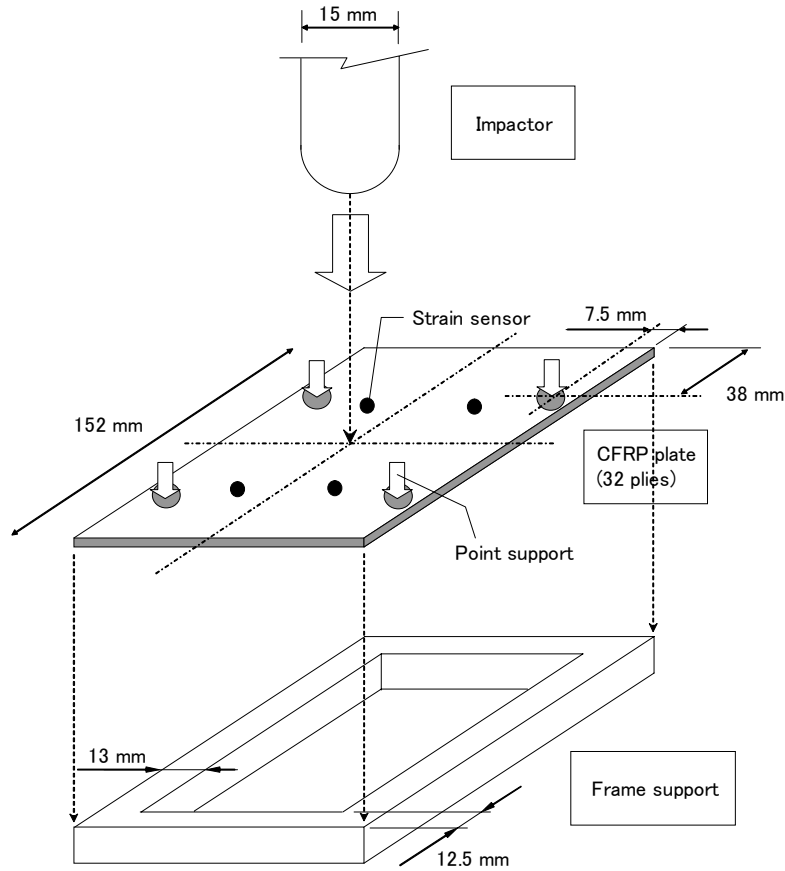


Figure 23. Weight-drop experimental setup.

- Loading

$$F = \kappa \alpha_c^{1.5}, \quad 0 < \alpha_c \leq \alpha_m \quad (12a)$$

- Unloading

$$F = F_m \left( \frac{\alpha_c - \alpha_0}{\alpha_m - \alpha_0} \right)^q \quad (12b)$$

where  $\alpha_m$  is the maximum indentation in the loading stage,  $F_m$  is the maximum contact load before unloading, and  $\alpha_0$  is permanent indentation and defined as

$$\alpha_0 = \begin{cases} \beta(\alpha_m - \alpha_{cr}) & \text{if } \alpha_m > \alpha_{cr} \\ 0 & \text{if } \alpha_m < \alpha_{cr} \end{cases} \quad (13)$$

where  $\beta$  and  $\alpha_{cr}$  are experimental constants.  $\kappa$  and  $q$ , which depend on the shape of the ball and material properties of the laminate and the ball. All of these parameters are taken from the work of Tan and Sun [15], and listed in Table 7.

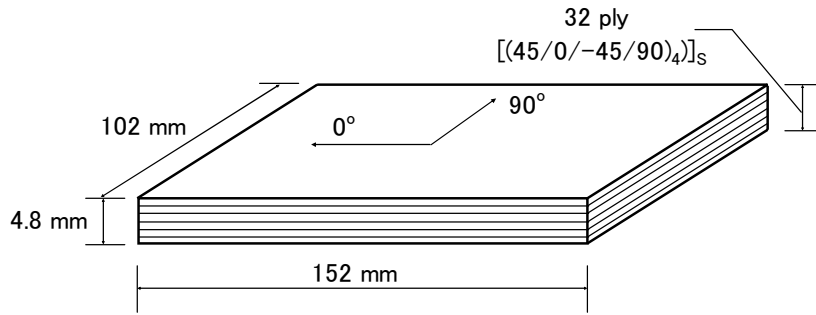


Figure 24. Specimen of 32 plies quasi-isotropic CFRP plates

Table 6. Results of impact tests for various impact energies

Case No.	Impact energy (J)	Damage
1	3.0	none
2	3.0	none
3	4.8	none
4	4.8	damaged
5	6.0	damaged
6	6.0	damaged
7	7.2	damaged
8	7.2	damaged



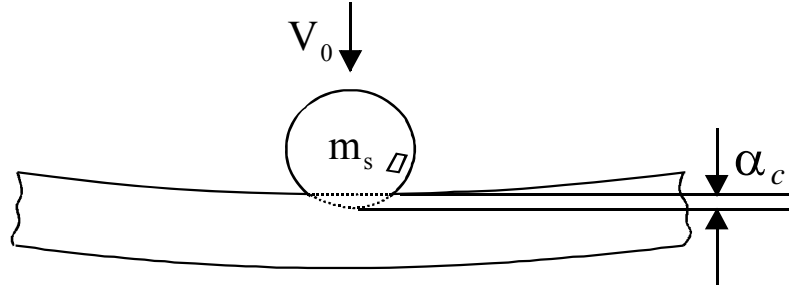


Figure 25. Contact model between a rigid ball and laminates

Table 7. Constants used in modified Hertz contact model

Indentation constants
$\beta=0.094$ , $\alpha_{cr}=0.1667$ mm, $\kappa=1.423 \times 10^6$ N/cm <sup>1.5</sup> , $q=2.5$

Some efforts have been performed to reduce the computation cost when modeling this complex problem with 32 plies. The whole plate needs to be modeled due to the existence of  $\pm 45^\circ$  plies. The plate is divided into three portions. In the central area of 35mm $\times$ 35mm, along the thickness direction, 32 brick elements at 32 plies are placed plus 30 cohesive elements at 30 interfaces since the maximum size of delaminations is smaller than 30mm $\times$ 30mm from experimental

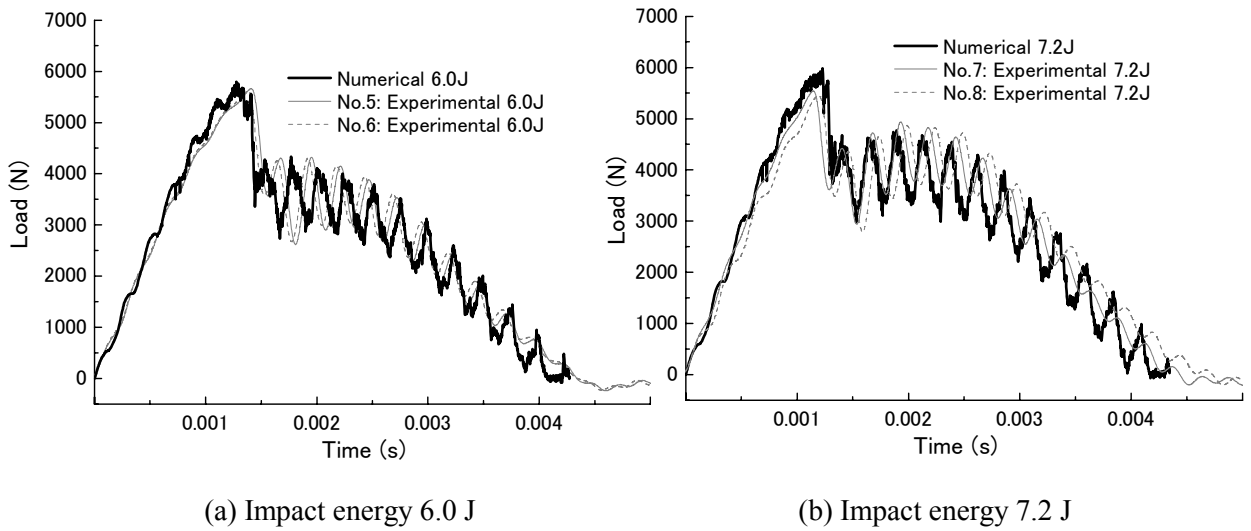


Figure 26. Results of impact force history

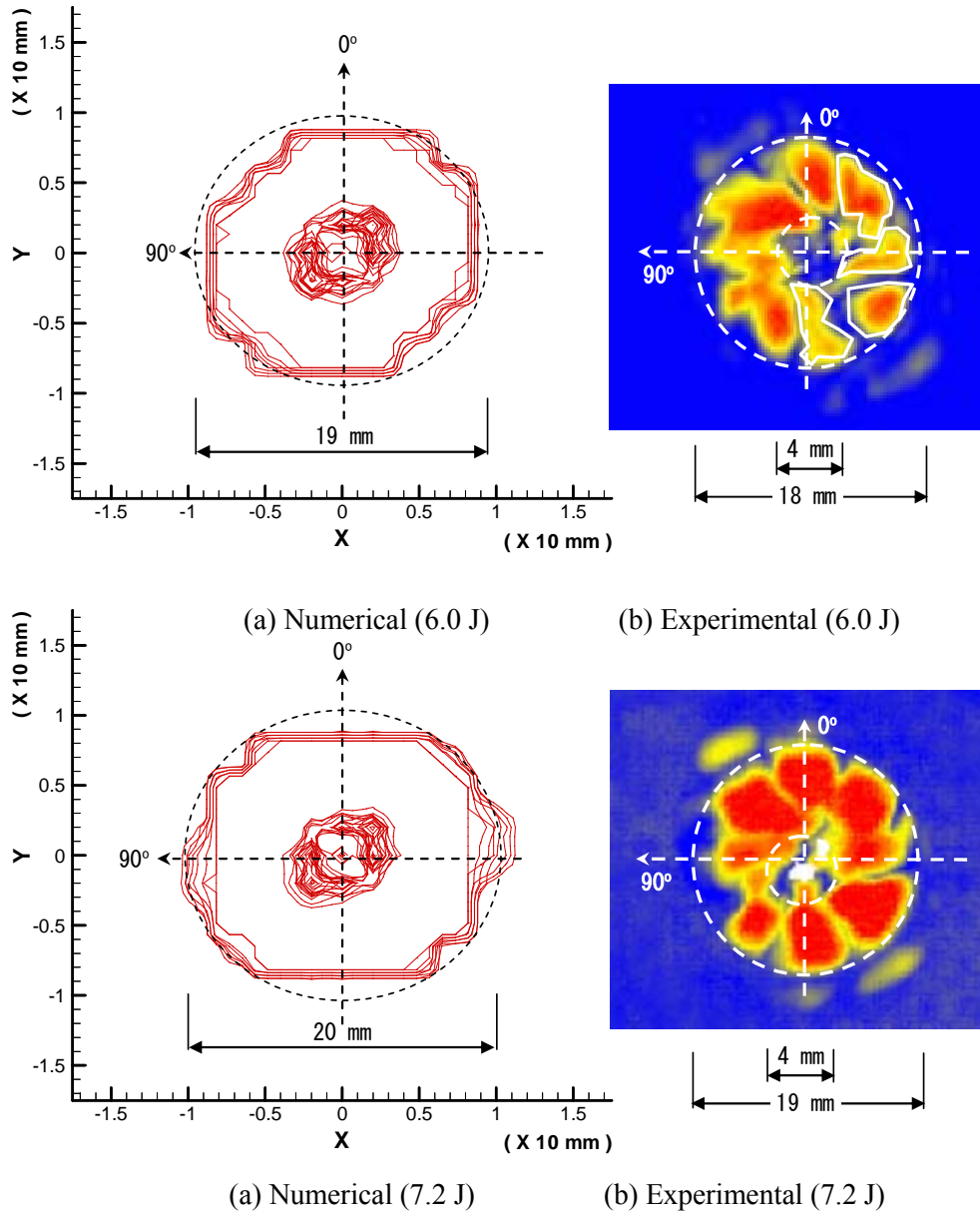


Figure. 27. Delaminations at the side of impact on specimen

observations. Also, at the interface of middle two plies  $90^\circ/90^\circ$ , there is no need to insert cohesive interface element. The mesh size in this central area is  $2.5\text{mm} \times 2.5\text{mm}$ . In the outer region, the cohesive elements at 30 interfaces are omitted, and only 32 brick elements at 32 plies are placed along the thickness direction. In the outermost area, only one brick element along the thickness direction is placed. The equivalent material properties of the outermost one layer are determined from the comparison of first three natural frequencies of a cantilevered specimen, which are obtained from vibration tests and numerical computation of a one-layer model, respectively. With the assumption of linear distribution of in-plane displacements along the thickness direction,

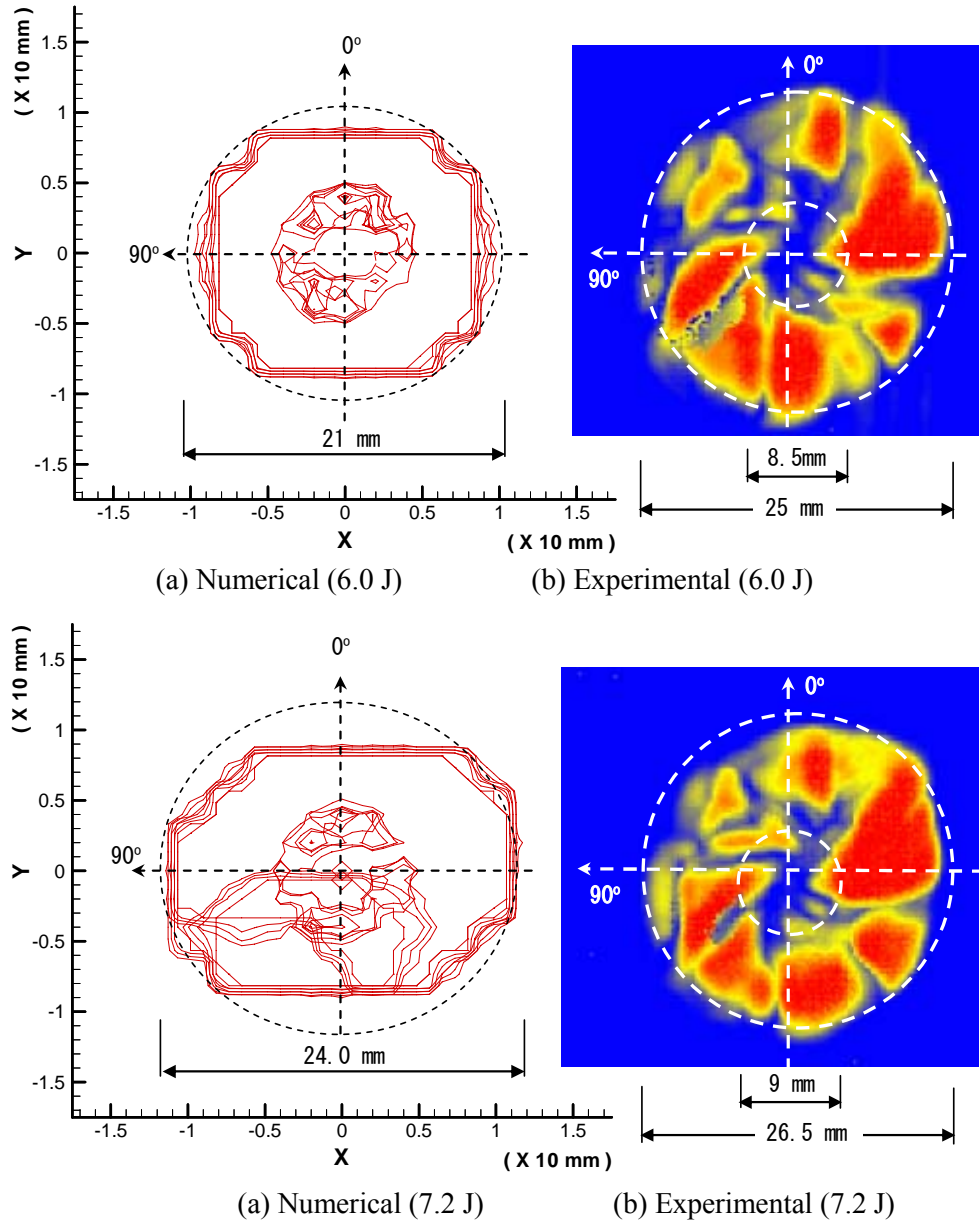


Figure. 28. Delaminations at the opposite side of impact on specimen

some strong springs are inserted at the boundary between the 32-layer region and the one-layer region to enforce the continuity of displacements. Finally, the total number of elements including the cohesive elements is 24696. The contact force between the ball and CFRP laminates is simulated by a distributed load applied on a 4mm×4mm central square area of plate since it is observed that there is an approximate circular unrecoverable indentation area of radius of around 2.0 mm~2.5 mm on specimens after impacts.

For cases of impact energies of 6.0 J and 7.2 J, the impact force histories versus time are demonstrated in Fig. 26, respectively. First, from Fig. 26(a), it can be found that the numerical result agree with two experimental results very well. The repeatability of two experimental results

is very good. After the peak load, there is a sudden drop in the load history. After this drop, the impact load decreases gradually. From Fig. 26(b), we can find that the impact load in 7.2 J is basically similar to that of 6.0 J. However, after the sudden drop from the peak load, the impact load does not decrease immediately as that shown in Fig. 26(a) for 6.0 J. For the case of 7.2 J, after the point of sudden drop, there is a platform, where the impact load keeps constantly. After this platform, the impact load decreases gradually. The numerical result reproduces this feature very well compared with the experimental results in Fig. 26(b).

The delaminations on the side of impact and opposite side of impact, which are obtained from numerical computations and ultrasonic inspections respectively, are shown in Figs 27~28. very well although the maximum sizes of delaminations are a little smaller than that of experimental ones. Furthermore, for the delamination distribution along the thickness direction from the top surface to the bottom surfaces of specimen, the delaminations at various interfaces obtained numerically can capture the main features of conical delamination distribution along the thickness direction observed from experiments.

After constructing this powerful numerical model [13], we can easily evaluate internal damages in CFRP materials using the identified impact force history and the FEM numerical model with the verification of the experimental results. Therefore, with the identified impact force history, the internal damages can be predicted. To realize the purpose of the on-line structural monitoring, a database can be built up by using the numerical model and limited experimental data. Then, the relationship between the damage extents and features of impact force, such as the maximum impact force, can be set up. Finally, by integrating the identification system of impact force with the constructed database, the structural health monitoring system can be finally accomplished.

## Reference

1. J.C. Brewer and P.A. Lagace. Quadratic stress criterion for initiation of delamination. *J. Compos. Mater.*, 22, 1141-1155, 1988.
2. J.P. Hou, N. Petrinic and C. Ruiz. A delamination criterion for laminated composites under low-velocity impact. *Compos. Sci. Technol.*, 61, 2069-2074, 2001.
3. G.A.O. Davies and X. Zhang. Impact damage prediction in carbon composite structures. *Int. J. Impact Eng.*, 16(1), 149-170, 1995.
4. S. Zheng and C.T. Sun. A double-plate finite-element model for the impact-induced delamination problem. *Compos. Sci. Technol.*, 53, 111-118, 1995.
5. C.F. Li, N. Hu, Y.J. Yin, H. Sekine and H. Fukunaga. Low-velocity impact-induced damage of continuous fiber-reinforced composite laminates. Part I. An FEM numerical model.

- Compos. Part A*, 33, 1055-1062, 2002.
6. C.F. Li, N. Hu, J.G. Chen, H. Fukunaga and H. Sekine. Low-velocity impact-induced damage of continuous fiber-reinforced composite laminates. Part II. Verification and numerical investigation. *Compos. Part A*, 33, 1063-1072, 2002.
  7. P.P. Camanho and C.G. Davila. Mixed-mode decohesion finite elements for the simulation of delamination in composite materials. *NASA/TM-2002-211737*, 2002.
  8. P.H. Geubelle and J.S. Baylor. Impact-induced delamination of composites: a 2D simulation. *Compos. Part B*, 29B, 589-602, 1998.
  9. Jr E.D. Reddy, F.J. Mello and T.R. Guess. Modeling the Initiation and Growth of Delaminations in Composite Structures. *J. Compos. Mater.*, 31(8), 812-831, 1997.
  10. Y. Mi, M.A. Crisfield, G.A.O. Davis. Progressive delamination using interface element. *J. Compos. Mater.*, 32(14), 1246-1272, 1998.
  11. Y.F. Gao, A.F. Bower. A simple technique for avoiding convergence problems in finite element simulations of crack nucleation and growth on cohesive interfaces. *Modelling and Simul Mater Sci Eng*, 12, 453-463, 2004.
  12. N. Hu, Y. Zemba, H. Fukunaga, H. H. Wang and A. M. Elmarakbi. Stable numerical simulations of propagations of complex damages in composite structures under transverse loads. *Compos. Sci. Technol.*, 67, 752-765, 2007.
  13. N. Hu, Y. Zemba, T. Okabe, H. Fukunaga and A. M. Elmarakbi. A new cohesive model for simulating delamination propagation in composite laminates under transverse loads. *Mechanics of Materials* (submitted for publication)
  14. J.P. Hou, N. Petrinic, C. Ruiz and S.R. Hallet. Prediction of impact damage in composite plates. *Compos. Sci. Technol.*, 60, 273-281, 2000.
  15. T.M. Tan and C.T. Sun. Use of statistical indentation laws in the impact analysis of laminated composite plates. *J. Appl. Mech.* 52, 5-12, 1985.

## **2. “Active” element: an active monitoring technique based on a multi-functional sensor/actuator system**

Over the last two decades, the Lamb wave technique has been studied widely. To date, many developed Lamb wave-based techniques detect damage, with the aid of a two-stage prediction model to find the difference in the signals between defective structure and benchmark, i.e. intact structure, for defining the *residual error* no matter what kind of information inherited in signals is used, such as the information in the time domain [1, 2] or the information in the frequency domain [3, 4]. Therefore, a benchmark or baseline signal is essential for comparison in this kind of techniques. Also, tremendous efforts [5-7] have been done to solve the damage

identification problem as an inverse pattern recognition problem through comparison between theoretical results and experimentally captured signals, such as artificial neural network etc. Most of these techniques do not need the baseline data of intact structures although they may also be used, e.g. in [7]. This kind of techniques needs to carefully verify the effectiveness of the theoretical or numerical models by comparing with experimental data to increase its reliability and accuracy. Another important issue is the proper selection of Lamb mode. Another problem is that, in recent, utilization of  $A_0$  mode is increasing due to its smaller wavelength and sensitivity to small damages. However, it is not an easy task to dominantly generate  $A_0$  mode when using simple and cheap PZT elements although it possesses many merits, such as wide frequency responses, easy integration, excellent mechanical strength, low power consumption and acoustic impedance, as well as low cost. For this purpose, some studies have been performed. For instance, a multi-element transducer set-up was proposed for composite laminated beams [8]. Through carefully choosing the distance between two PZT elements, the normal displacement of  $A_0$  mode can be maximized and that of  $S_0$  mode can be minimized.

Although there have been a lot of studies in this field, some further efforts are still needed to apply for the Lamb wave-based techniques for some more complex structures with higher reliability and accuracy. With the previous background in mind, two important issues will be focused on in this research. The first one is about the baseline data of intact structures. A damage identification technique without using the baseline data, what will be studied here, is preferred for some aging structures. We have shown that by directly using experimental data, it is possible to detect the damages in metallic and composites structures without the sensor data of pre-damaged structures [9, 10]. Another issue is to generate  $A_0$  mode conveniently using piezoelectric actuators. In this study, for the damage identification in metallic structures, we have experimentally developed two kinds of  $A_0$  mode generation techniques using piezoelectrics [9]. In the first one, we attach two PZT actuators with opposite applied voltages on both sides of structures. In the second one, a kind of grease lubricant between the bottom surface of one actuator and the surface of specimens is used. Both techniques can generate comparatively pure  $A_0$  mode Lamb wave. For beam-like aluminum structures with transverse cracks, the first kind of  $A_0$  mode generation technique with two actuators and one sensor is employed. For aluminum plate structures, the second kind of  $A_0$  mode generation technique is employed. In this case, a kind of transducer set containing three sensors and one actuator is developed. A small hole and a very short crack in the plate are considered. The numerical simulations using FEM are also carried out. It has been found that the numerical results agree with the experimental ones very well. For composite laminated beams [10],  $S_0$  mode Lamb wave is used for delamination identification. The scattering between the propagating wave and the delamination is studied in detail. The detailed place in the delamination where the strongest reflections are generated is

identified. This information can help us identify the detailed delamination position.

Finally, compared with some existing techniques using Lamb waves, an important merit of the proposed technique is that there is no need for the benchmark data or the data of intact structures before damages if we know the information of structural dimensions and wave propagation speed from which we can separate the reflection from damage and reflections from structural boundaries.

## 2.1 Metallic structures [9]

### a. Beam problem

First, when attaching two PZT actuators with applied out-of-phase voltages on both sides of an aluminum beam with one-sided or two-sided transverse cracks shown in Fig. 29, we can generate very pure  $A_0$  mode Lamb wave. We also perform the numerical computation using FEM. In Fig. 30(a), we have compared the numerical results with the experimental results when there is no crack. We can find that the very pure  $A_0$  mode Lamb wave can be excited. In Fig. 30(b) and Fig. 30(c), we have shown the wave signals when there is one-sided transverse crack

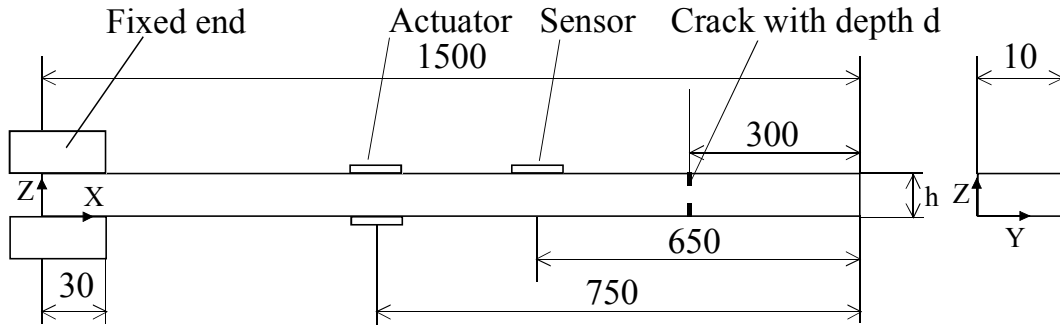
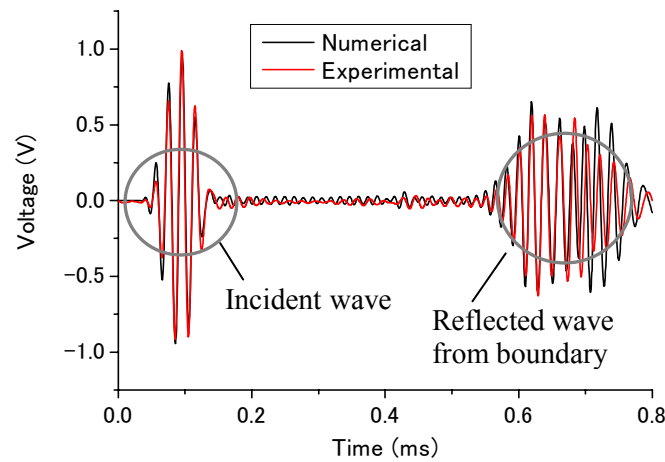
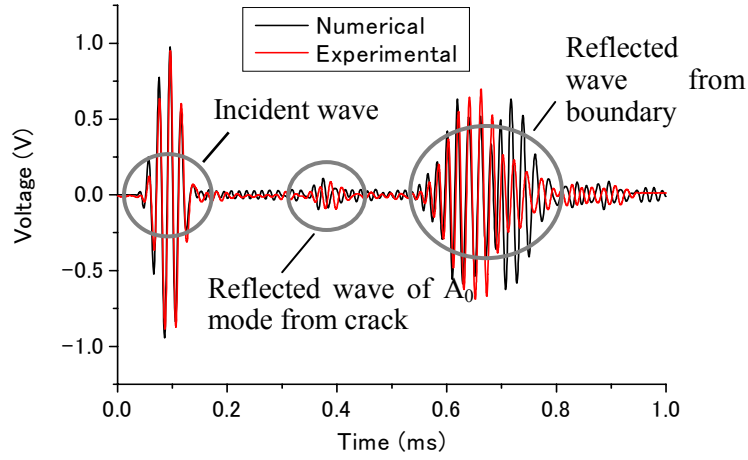


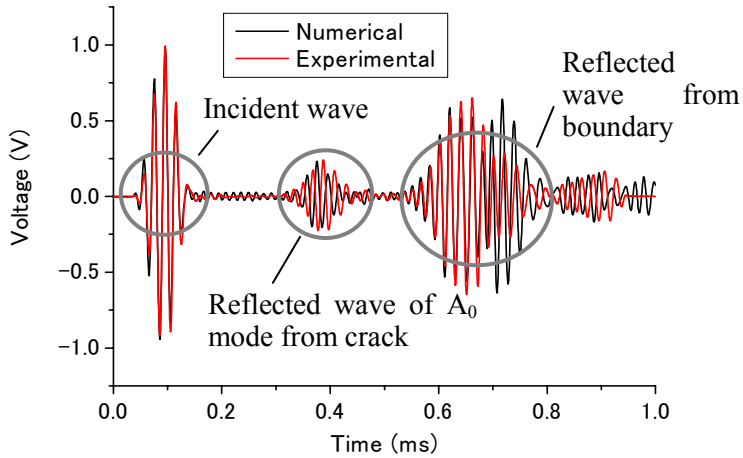
Figure 29. Schematic view of aluminum beams with cracks (length unit: *mm*)



a) Numerical and experimental results of intact beam



b) Numerical and experimental results of beam with 1.25 mm single crack on one side



c) Numerical and experimental results of beam with 1.25 mm double cracks on two sides

Figure 30. Comparison of numerical and experimental results for aluminum beam of 5 mm thickness

Table 8. Results of identified crack position for 3 mm and 5 mm beams

	Thickness [mm]	Group velocity [m/s]	Arrival time [ms]	Position [mm]	Error [%]
Calculate	3	2068.5	0.354	1216.1	1.3
	5	2449.5	0.285	1199.1	0.1
Experimental	3	2068.5	0.349	1211.0	0.9
	5	2449.5	0.291	1206.4	0.5



or there are two-sided transverse cracks. From these figures, we can find that there is a very clear reflected wave blob from cracks, which is located between the incident wave and reflected waves from boundaries. By employing the wavelet transformation technique, we can calculate the arrival time of the reflected wave from cracks, and with the experimentally obtained or theoretically evaluated wave propagation speed, we can identify the damage location very accurately as shown in Table 8.

#### **b. Two-dimensional plate problem**

As stated in the above example, in this study, an important feature is to catch the reflected waves from damages directly without referring the data of pre-damaged state. Therefore, the intensity of the reflected waves from damages is a key factor for accurately identifying the positions of damages. For 2-dimensional plate problems, to investigate the intensity of the reflected waves from damages, first, the numerical computations are performed. As shown in Figure 31, for an aluminum plate with a hole of 20.0 *mm* in diameter, when the sensors are arranged around the hole, we compute the intensity of reflected waves from damages. The circular PZT actuator and sensor fixed on the surface of the plate are of 10 *mm* in diameter and 0.5 *mm* in thickness. The excitation signal is of 200 kHz frequency and 5 cycles. The configurations of wave propagation at the different time steps are shown in Figure 32, from which, we can identify the reflected wave from the hole very clearly. In this computation, both  $S_0$  and  $A_0$  modes are observed to exist. The amplitudes of the reflected wave from the hole for the sensors located on the different angles are obtained from the difference of wave signals ( $S_0$  mode) of the same plate without a hole and the plate with a hole. The maximum amplitude of the reflected wave from the hole at one sensor is used to normalize the others. The normalized intensity of reflected waves from the hole is shown in Fig. 33. This result illustrates that when the angle between the line connecting the actuator and the damage and the line connecting the damage and the sensor is very small, the intensity of reflected wave from the hole is very high. However, with the increase of this angle, the intensity drops very rapidly. Since the position of damage is unknown beforehand, a kind of transducer set is designed, which contains a centered actuator and three sensors located at the outer circumference as shown in Fig. 34 and 35. The distance between the actuator and the sensor was small, i.e. 50 *mm*. The angle between the line connecting the actuator to one sensor and the line connecting the actuator to another sensor was 120°. Therefore, no matter where the damage was located, comparatively strong reflected waves from damages were captured at one sensor at least. As shown later, an important merit of this transducer set is that it can be moved freely in a large area for damage detection purpose. For the case shown in Fig. 35, the distance from the actuator to damage is assumed as  $s$ , and the distances from sensors A, B and C to damage are assumed as  $a$ ,  $b$  and  $c$ , respectively. At first, we define the following variables,

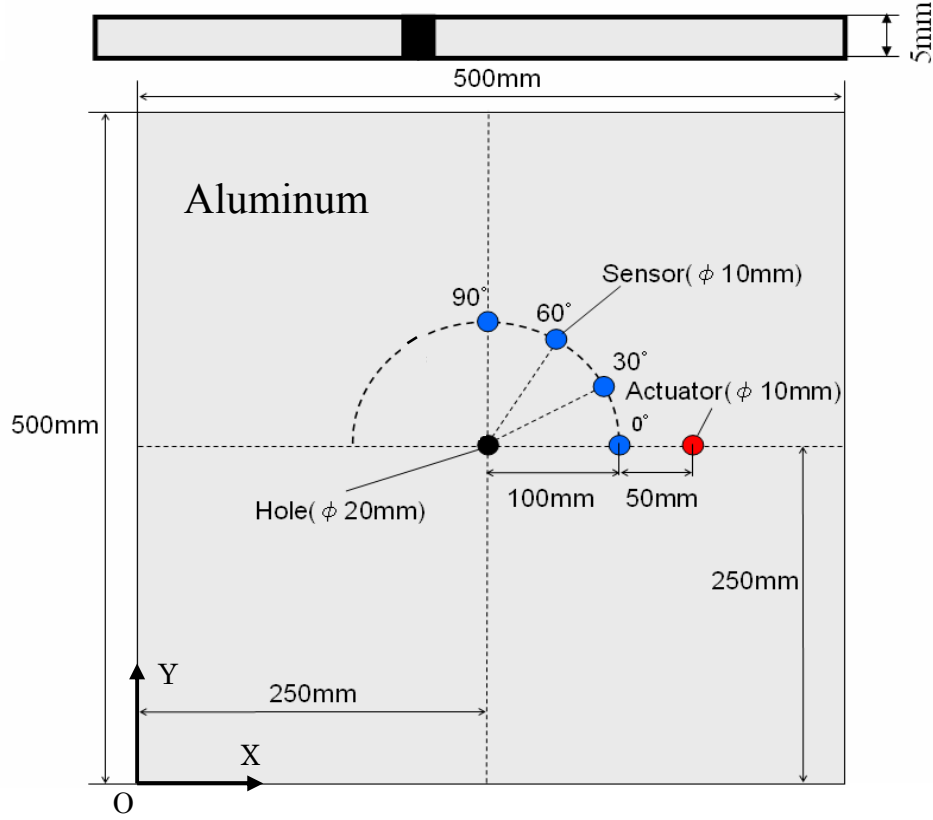


Figure 31. Schematic view of aluminum plate for FEM computation

$$a' = a + s \quad (14a)$$

$$b' = b + s \quad (14b)$$

$$c' = c + s \quad (14c)$$

From the measured experimental data using three sensors, the arrival times of the reflected waves from damages were obtained from the wavelet transformation, and then the distances  $a'$ ,  $b'$  and  $c'$  were calculated by virtue of wave propagation velocity. Finally, the unknown parameters  $a$ ,  $b$ ,  $c$  and  $s$  could be obtained easily. For example,  $s$  can be expressed as follows

$$s = \frac{a'^2 + b'^2 + c'^2 - 3r^2}{2(a' + b' + c')} \quad (15)$$

where  $r$  is the distance from the actuator to the sensor in Fig. 35 with the known value.

Finally, after determining the parameters of  $a$ ,  $b$ ,  $c$  and  $s$ , three circles with the centers of three sensors respectively can be drawn and the intersection of them is namely the position of damage.

To generate  $A_0$  mode of Lamb waves more conveniently, besides the technique with double-sided attached actuators in Fig. 29, a simpler technique has also been developed. In this technique, we applied a kind of grease lubricant under the bottom surface of actuator. The mechanism of this technique is to generate the vertical pressure from the actuator on the plate

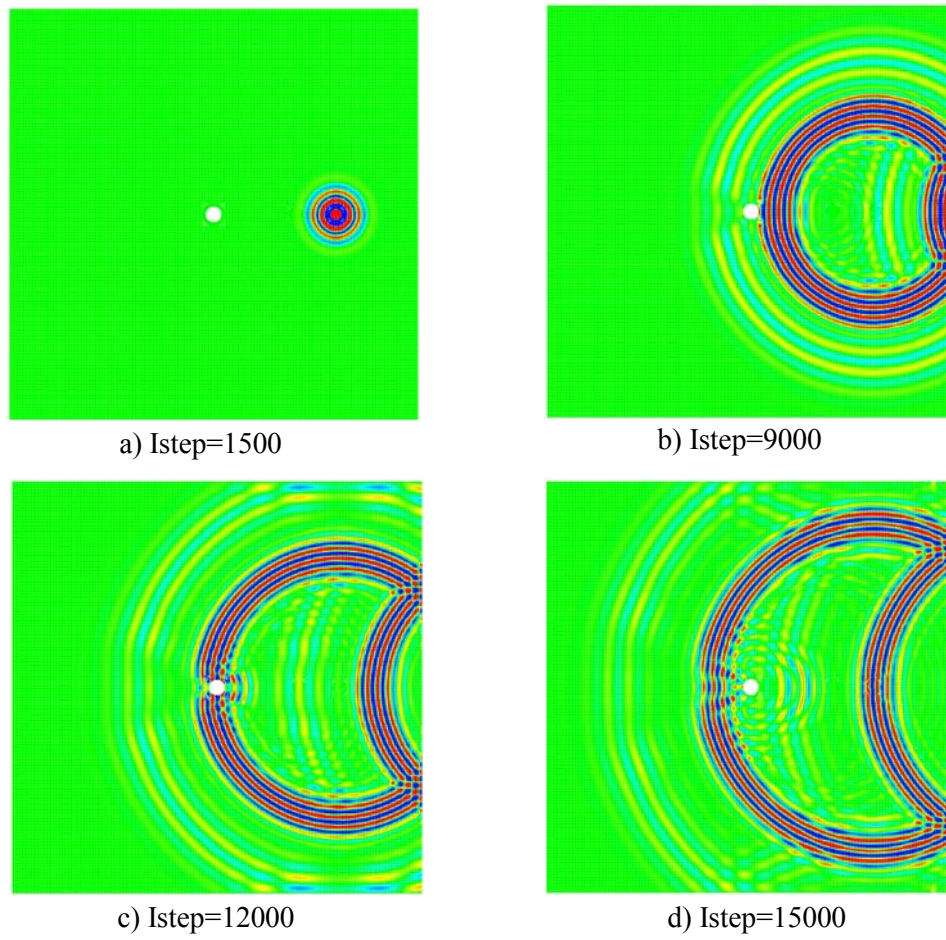


Figure 32. Configurations of wave propagation at various time steps

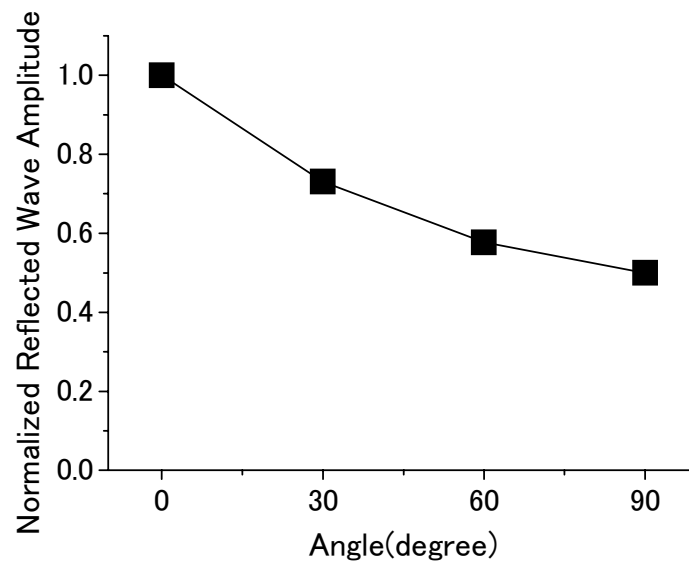


Figure 33. Normalized intensity of reflected wave from the hole versus angle of sensor

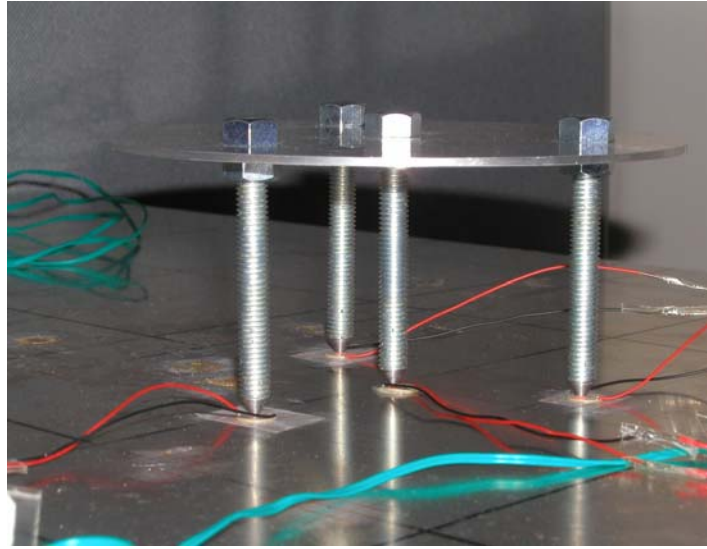


Figure 34. A removable transducer set

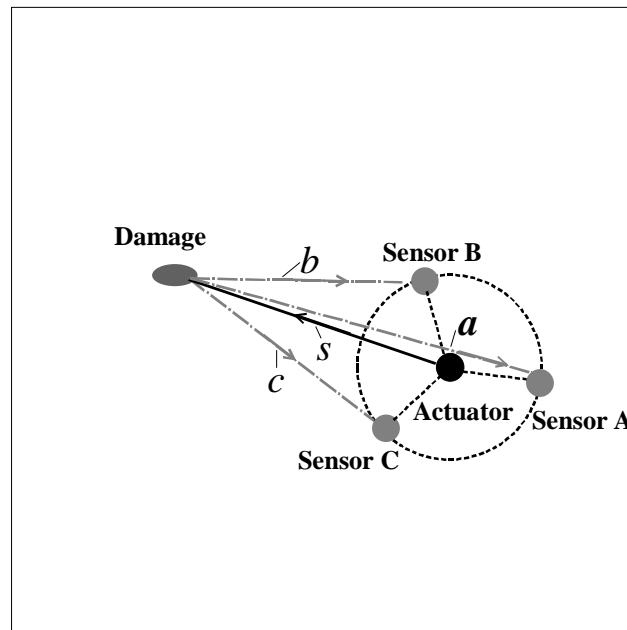
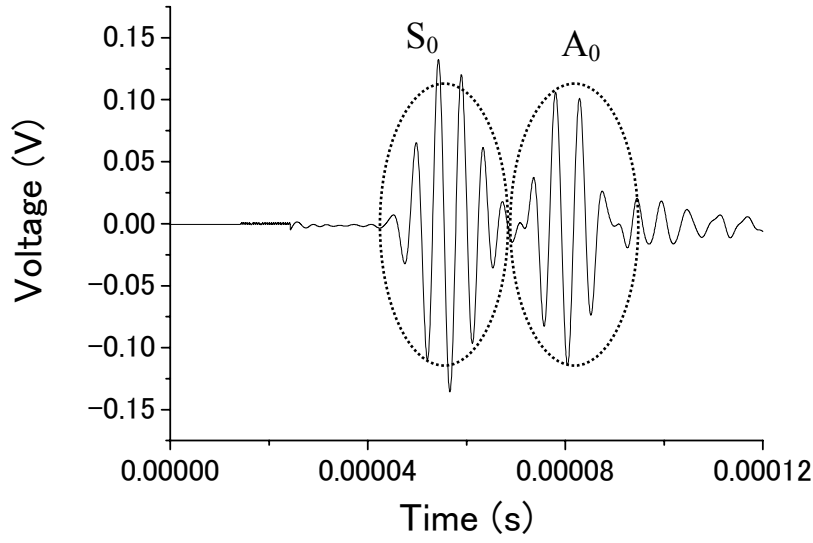
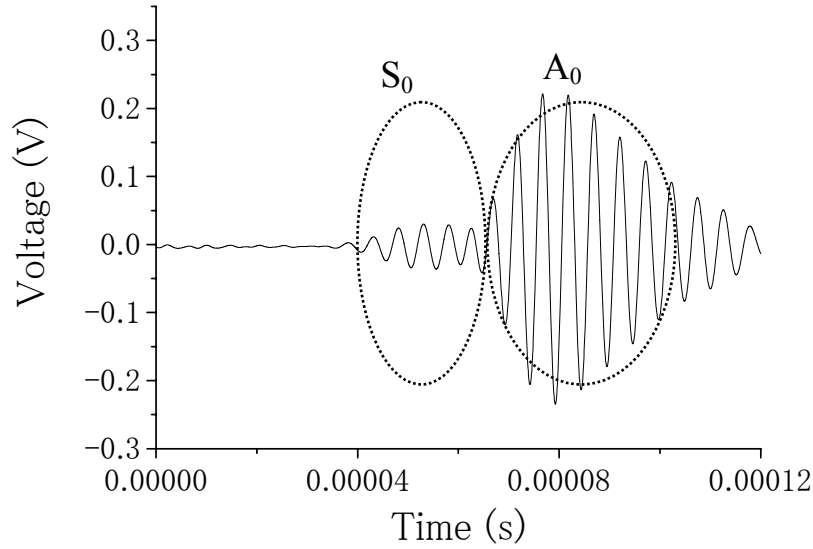


Figure 35. Schematic view of transducer set and damage

to excite *A* mode, and the strong shear force between the actuator and the plate is remarkably weakened since this shear force can excite *A* and *S* modes simultaneously when the actuator is not located on the mid-plane of plate. Also, due to the existence of the grease as wave propagation media, the signal from actuator does not attenuate significantly. To move the sensor freely, a kind of two-sided tape made of polypropylene film with weak acrylic adhesive was used between the bottom surface of sensor and the top surface of plate.



a) Strong adhesive used for actuator and sensor



b) Grease lubricant used for actuator and two-sided tape used for sensor

Figure 36. Comparison of wave forms for three kinds of bonding methods

By employing the above technique, very pure  $A_0$  mode of Lamb waves can be generated. The comparison of wave forms, when using three bonding methods between the bottom surface of actuator and sensor, and the top surface of plate, is shown in Fig. 36. The distance between the actuator and the sensor was 200 mm and the excitation signal was of 200 kHz frequency and 5 cycles. By referring to Fig. 36(a), for this excitation frequency, both  $S_0$  mode and  $A_0$  mode are generated using strong adhesive. From Fig. 36(b), we can find the grease lubricant used for actuator and the two-sided type used for sensor can remove  $S_0$  mode effectively although the excited  $A_0$  mode seems to have more cycles due to the usage of grease, which however has been

observed to have tiny influence on identification accuracy. Of course, this technique leads to the slightly shorter wave propagation distance compared with the first technique in beams. However, it is still enough to cover the large area ranging up to several hundreds *mm* depending on the excitation frequency. A very simple technique to enhance the signal in this case was to apply a constant vertical pin-load on a small area of the center of sensors. It has been found that the signal amplitude of sensor was enlarged by several times compared with that without applying such a vertical pin-load.

The above technique is applied to the transducer set as shown in Fig. 34, which contains the centered actuator and three surrounding sensors. Four screws passing through a top circular plate possessed a very small flat bottom tip, where the PZTs were attached. The screws can adjust the positions of PZTs along the vertical directions of specimen for possible curved structures. This set can be moved on the surface of specimen freely, and the vertical load on sensors can be increased conveniently by putting some weights on the top circular plate. From our experiences, it is better to avoid the strong vertical load applied on the actuator for obtaining the clear wave form. However, a suitable vertical load on sensors is preferred, which can increase the signal amplitudes. This can be easily realized by adjusting the positions of four

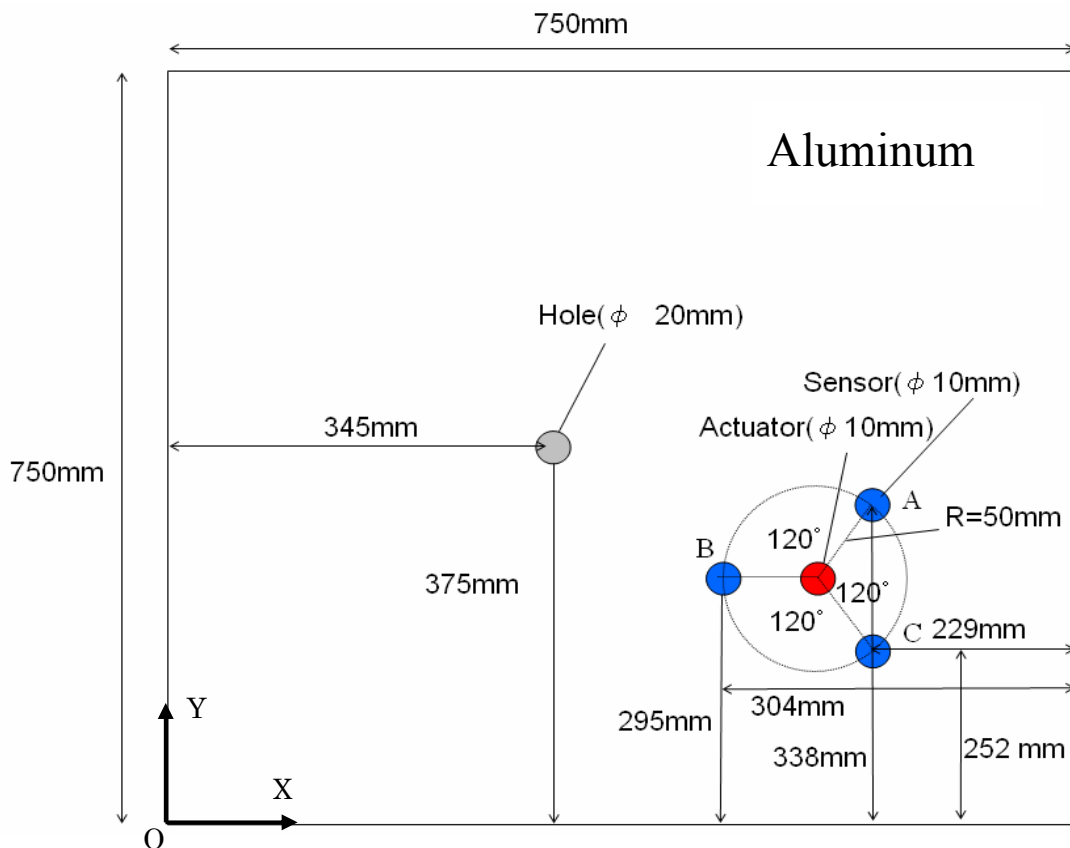


Figure 37. Schematic view of a plate with a hole and a transducer set

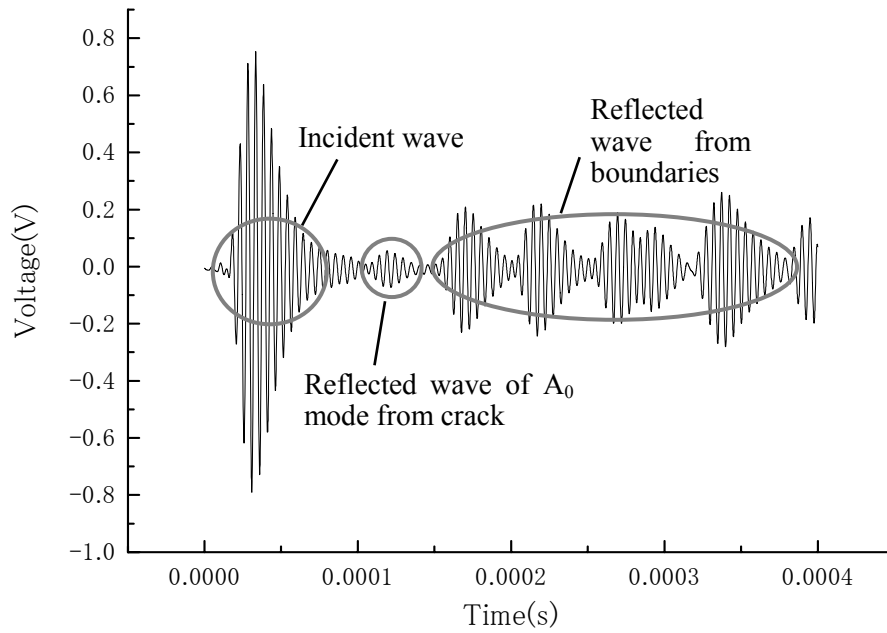


Figure 38. Signal of sensor A for a plate with a hole

screws along the vertical direction. It should be noted that without this equipment, by only directly placing the actuator and sensors on the surface of plate, sufficiently good signals could still be captured.

To verify the effectiveness of the above technique, first, for an aluminum plate of thickness

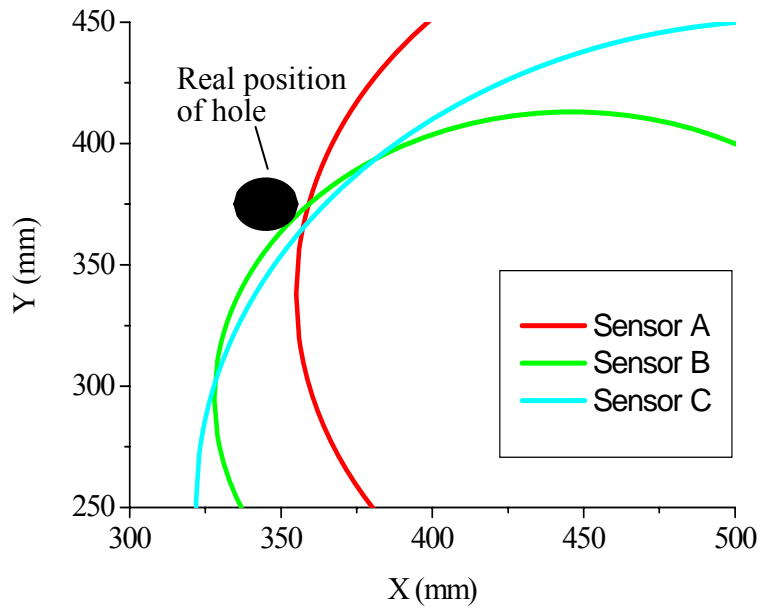


Figure 39. Identified position of hole using three circles

Table 9. Numerical results of identified hole position

	Correct values (mm)	Experimental (mm)	Error(%)
$s$	161	156	3.1
$a$	170	166	2.4
$b$	119	118	0.8
$c$	204	199	2.5

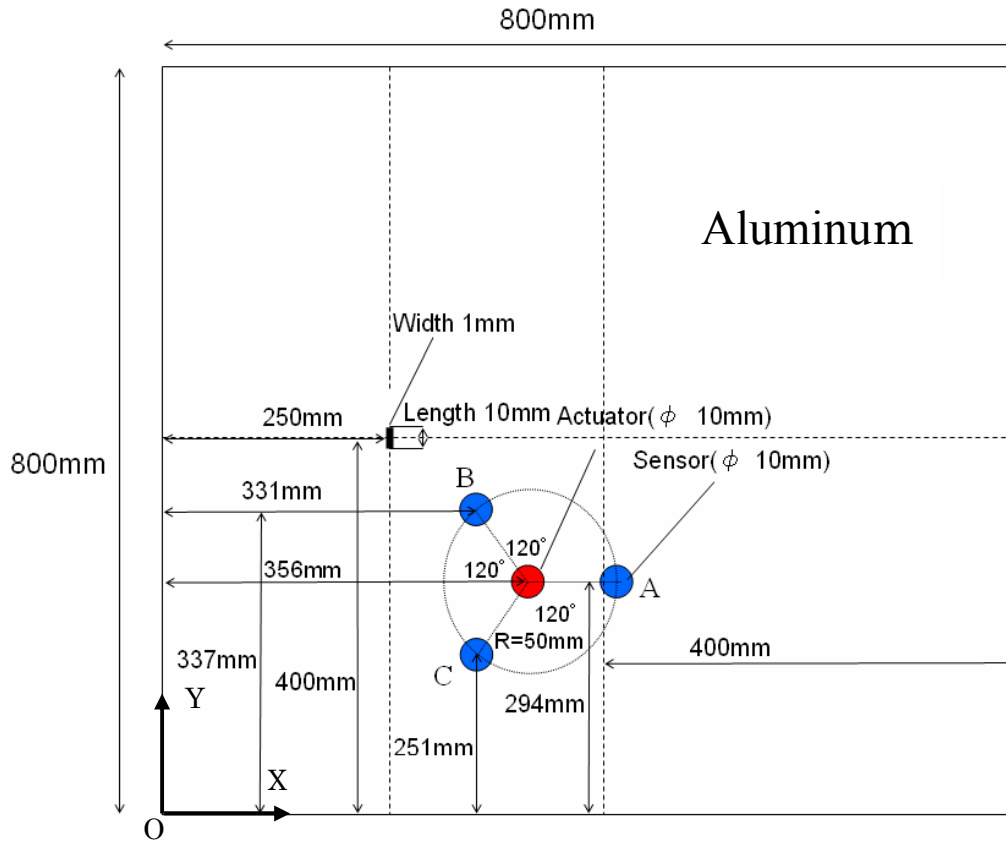


Figure 40. Schematic view of an aluminum plate with a transverse crack

5 mm, a hole of 2 cm diameter is shown in Fig. 37. The wave signal of sensor A is shown in Fig. 38, from which we can find pure  $A_0$  mode is excited. The reflected wave from the hole can be identified. For the identified hole positions in Fig. 39 using three circles centered by three sensors are shown in Table 9, where very accurate results are obtained.

Second, for a plate containing a very short crack shown in Fig. 40, the wave signal of sensor A is shown in Fig. 41, where the clear reflected wave from this small crack is shown. The identified crack positions in Fig. 42 are shown in Table 10, where very accurate results are obtained. The above technique has been applied to various cases for this crack when we move the transducer set.



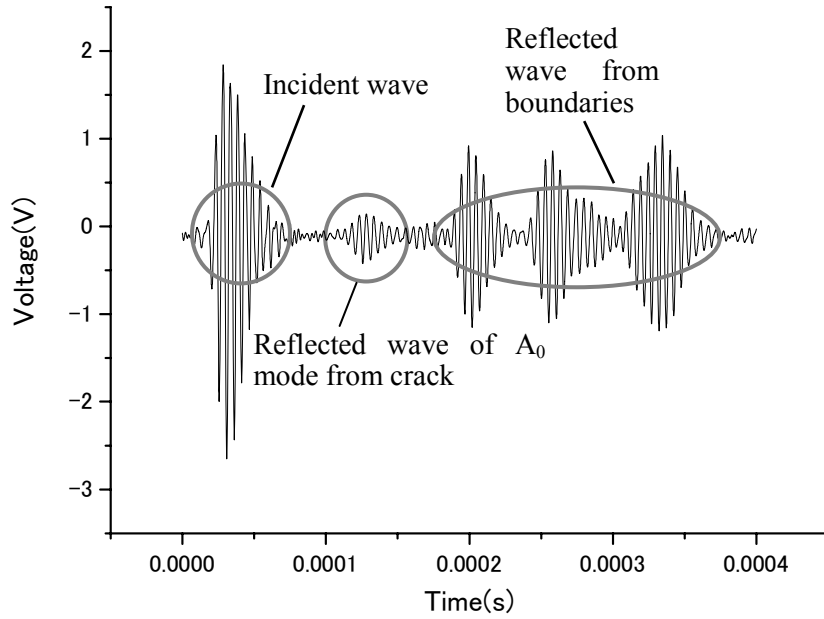


Figure 41. Signal of sensor A for a plate with a crack

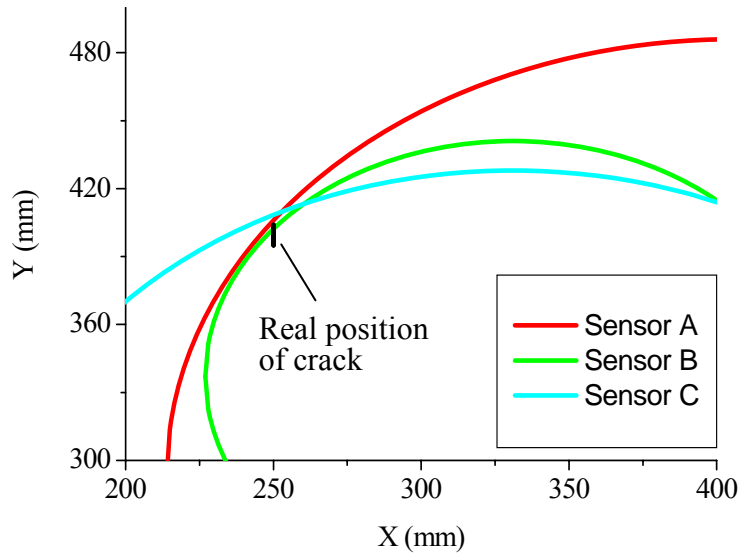


Figure 42. Identified position of crack using three circles when  $\theta=45^\circ$

It has been found that except that the transducer set is located on the vertical line parallel to the crack length direction, we can always detect the crack position very accurately. Due to the disappearance of  $S_0$  mode, the wave signal is very easily interpreted without using the sensor data of intact structures. Only when the damage is too close to the structural boundaries, where the reflected wave from the damage and the reflected wave from boundaries are overlapped, this technique becomes invalid.

Table 10. Comparison of the identified parameters and real ones

	Correct values (mm)	Experimental (mm)	Error(%)
$s$	150	154	2.7
$a$	189	192	1.6
$b$	103	104	1.0
$c$	170	177	4.1

## 2.2 Composite laminated beams [10]

By employing the similar technique without using the sensor data of intact structures, we can also identify the delamination in CFRP laminates. As shown in Fig. 43, a CFRP beam of stack sequence of  $[0_{10}/90_{12}/0_{10}]$ , which is of a man-made delamination through inserting Teflon sheet into CFRP material is used. In this case, we employ  $S_0$  mode Lamb wave.

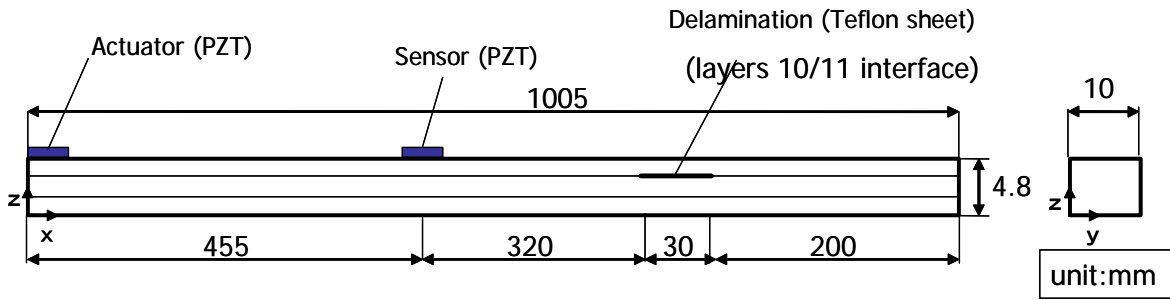


Figure 43. Schematic view of CFRP beam with a delamination (length unit: mm)

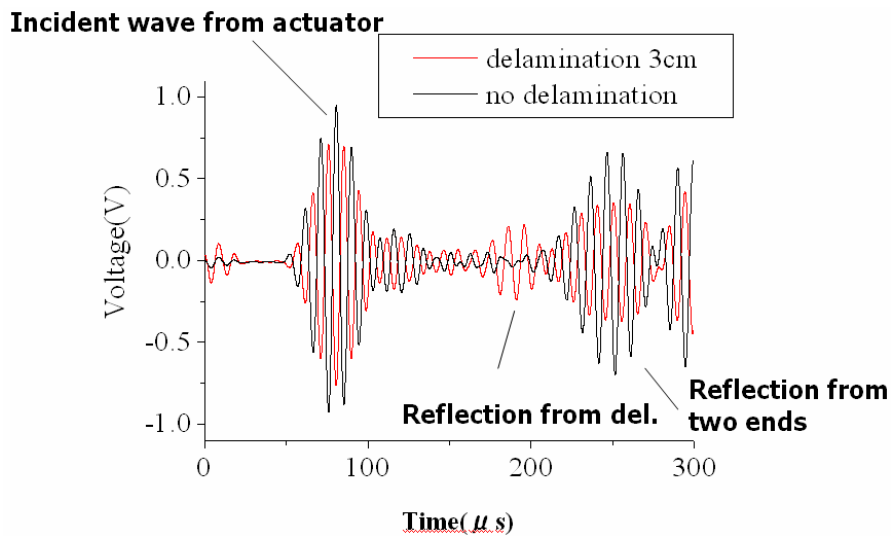


Figure 44. Comparison of experimental signals of intact and delaminated CFRP beam

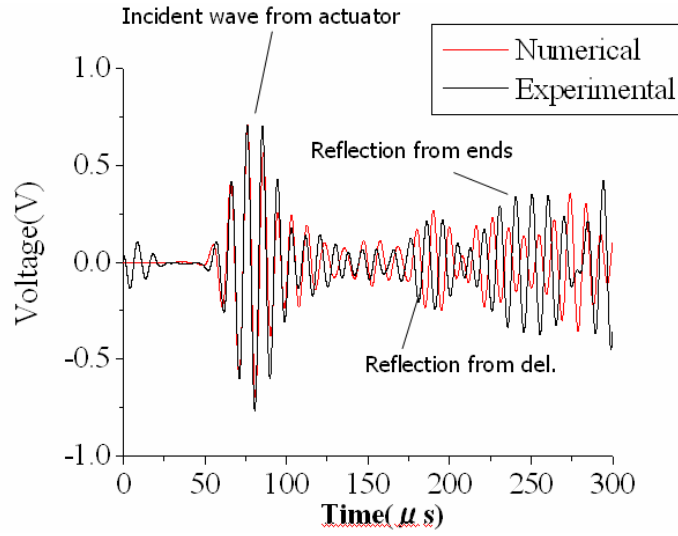


Figure 45. Comparison of experimental signals of intact and delaminated CFRP beam

Therefore, only one-sided attached actuator at the right end of beam is used. The comparison of experimental wave signals before and after delamination is shown in Fig. 44, from which the reflected blob from the delamination is clearly demonstrated. Figure 45 shows the comparison between the experimental results and FEM computational results, from which we can find that both results agree with each other very well. In this case, due to very fast wave speed of  $S_0$  mode, i.e. 6210m/s from experimental measurement, we employ it for delamination

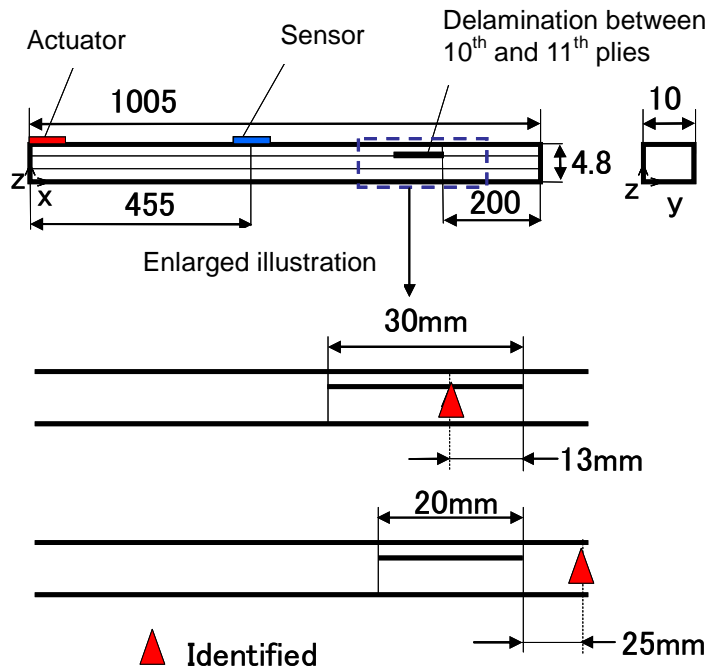
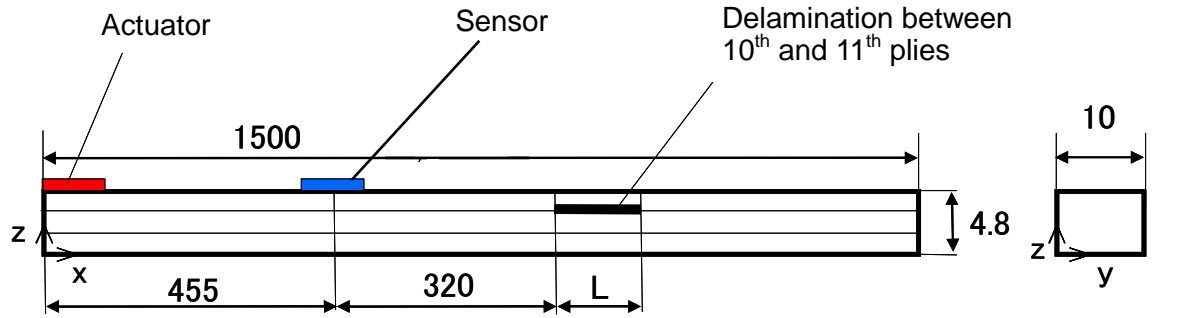
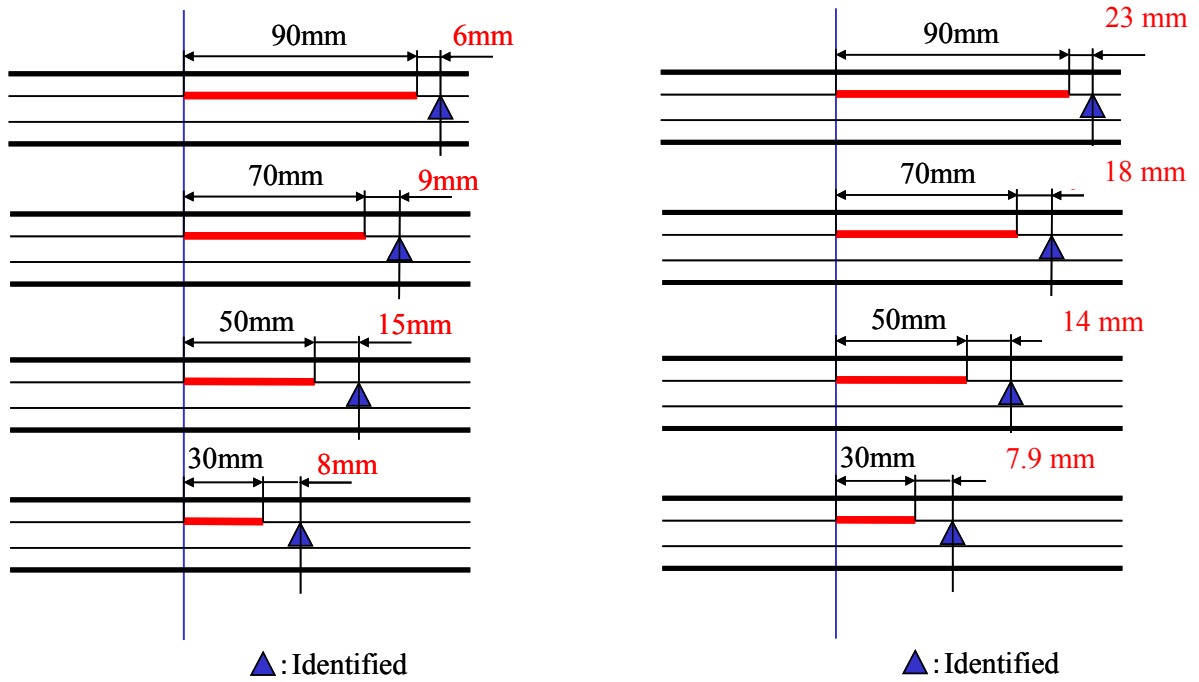


Figure 46. Experimentally identified delamination position



(a) Schematic view of the beam for numerical simulation (unit: mm)



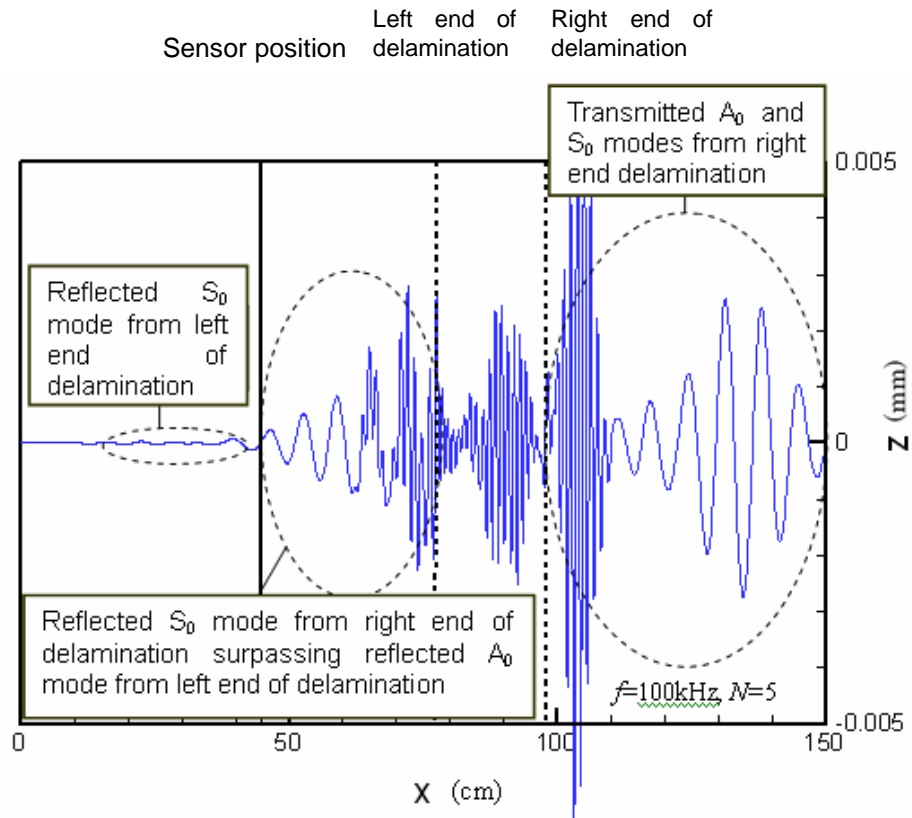
(b) Results using 6260 m/s

(c) Results using 8483 m/s in  $0^\circ$  delaminated layer

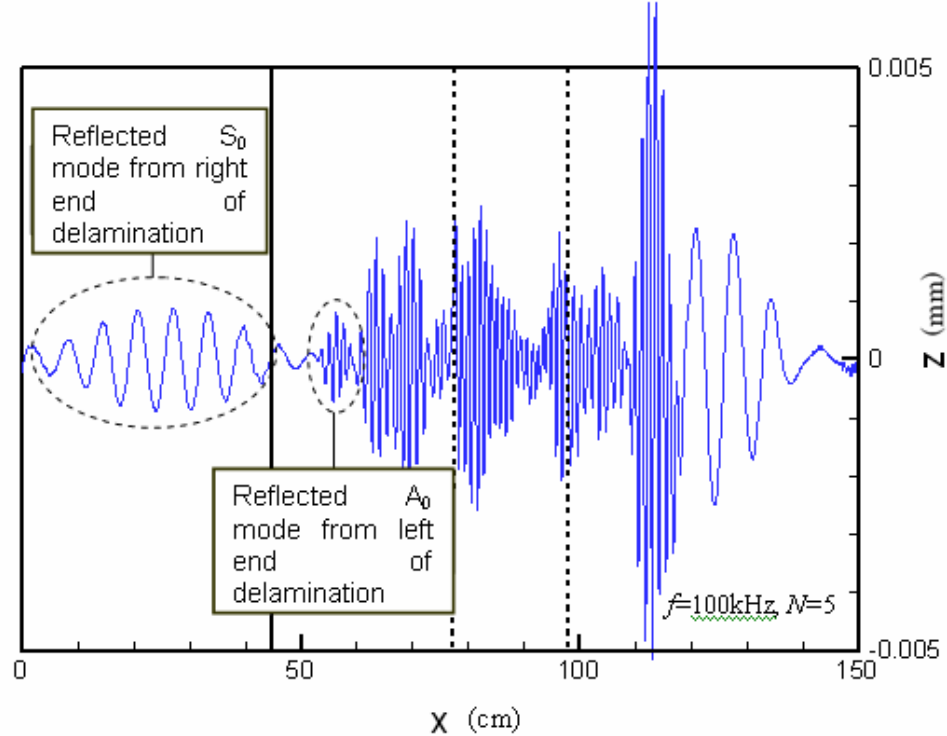
Figure 47. Numerical identification of positions of various delaminations

identification.  $A_0$  mode is too slower, which does not appear in these figures. The identified delamination position is shown in Fig. 46, from it, we can find the identified delamination position is very close to the true position. Also, we can find that the identified positions are close to the left end of the delamination in both cases.

To examine the capability of the numerical simulation to identify the location of a delamination, the length of delamination  $L$  (Fig. 47(a)) was increased from 30 to 90 mm. The length of the beam was also increased up to 1500 mm. Under a condition of  $f=100$  kHz and  $N=5$ , the propagation speed of  $S_0$  mode was firstly calculated in an intact beam with two sensors. The estimated propagation speed was 6260m/s, which is very close to the experimental measurement. Based on this speed, the numerically identified positions for various delamination lengths are



(a) 236  $\mu$ s (difference of wave signals of intact and delaminated beams)



(b) 303  $\mu$ s (difference of wave signals of intact and delaminated beams)

Figure 48. Scattered wave signals of a beam with a delamination of length of 200 mm (signal differences of intact and delaminated beams)

shown in Fig. 47(b). It is surprising to note that all predicted positions are beyond the right end of the delaminations. It has been demonstrated that a higher propagation speed of  $S_0$  mode in the delaminated  $0^\circ$  layer can make the predicted delamination positions behind the actual delaminations. From the FEM simulations, the estimated speed of  $S_0$  mode in the  $0^\circ$  delaminated layer was 8483 m/s. If we use this speed in the delaminated region only (in the intact region, we still use 6260 m/s), with the known left end of the delamination, the predicted delamination positions or the reflected positions of  $S_0$  mode are shown in Fig. 47(c). Comparing it with Fig. 47(b), we can find that there is no obvious difference in the delamination positions for short delaminations, e.g. 30 and 50 mm. However, for a longer delamination (70 and 90 mm), an increased deviation from the actual delamination is observed when 8483 m/s was used in the prediction. It implies that the use of the actual wave speed in the delamination area can not improve the prediction and a reflected wave with observable intensity is normally from the right end of the delamination.

To gain a better understanding of this complex interaction, a beam with a length of 1500 mm and a 200 mm long delamination was examined using the numerical simulation. Under a condition of  $f=100$  kHz and  $N=5$ , at two time points, the subtraction between the wave signals from the intact and the delamination-containing beams is shown in Fig. 48. This subtraction can amplify the scattered wave signals from the delamination. The transverse deflections at various mesh points on the top surface of the beam are used as wave signal. The typical sensor signal for accurately evaluating the arrival times of various waves is shown in Fig. 49.

Corresponding to 236  $\mu$ s, the reflected  $S_0$  mode from the left side of the delamination has already passed through the sensor, Fig. 48(a). However, at the same time point in Fig. 49, this reflected  $S_0$  mode cannot be detected by the sensor due to its small amplitude. Also, the reflected  $S_0$  mode from the right end of the delamination, which is surpassing the reflected  $A_0$  mode from the left end of the delamination, can be observed, as shown in Fig. 48(a). A new transmitted  $A_0$  mode and the transmitted  $S_0$  mode from the right end of the delamination can be clearly observed, Fig. 48(a). At 303  $\mu$ s, as shown in Fig. 48(b), the reflected  $S_0$  mode from the right end of the delamination completely surpasses the reflected  $A_0$  mode from its left end. This reflected  $S_0$  mode has already passed through the sensor position. From Fig. 49, the arrival time of the reflected wave from the delamination is identified as around 275  $\mu$ s. Therefore, the reflected wave signal detected clearly by the sensor is considered to be the reflected  $S_0$  mode from the right end rather than the left end of the beam, due to its higher intensity. Based on the numerical simulations above, the very complex interaction between the different signal modes and the boundaries of a delamination can be identified. When only a single  $S_0$  mode passes through a delamination, four modes will be generated at one end of the delamination, including two transmitted  $A_0$  and  $S_0$  modes, and two reflected  $A_0$  and  $S_0$  modes. However, the reflected  $S_0$

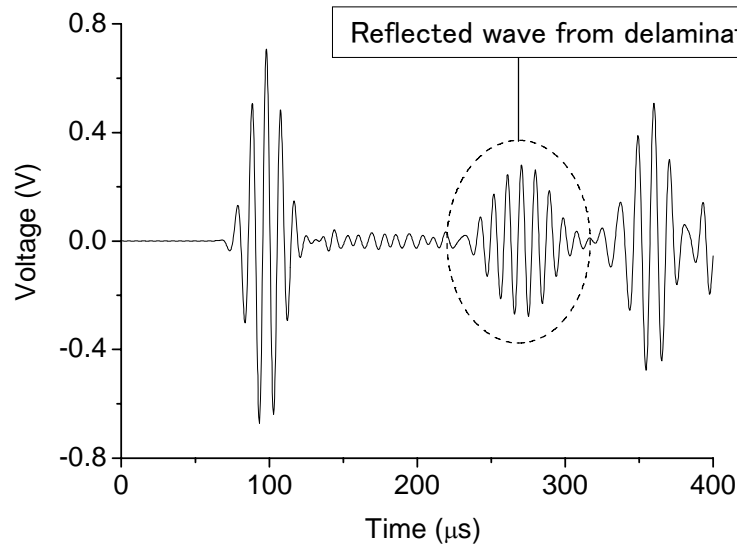


Figure 48. Sensor signal for a delamination of length of 200 mm

mode received by a sensor is from the right end of the delamination. Further study is required to understand why the stronger reflections are from the right end of a delamination. One possible explanation is that the delaminated region is of lower bending stiffness, which can be considered to be a softer region. When a wave propagates from a harder or intact region into a softer region, the reflections become weak. In contrast, when the wave propagates from a softer region into a harder one, a stronger reflection is expected.

In this work, a structural health monitoring technique has been proposed. The baseline data of the intact structures are not needed in the present technique. This method is applied to the damage identification, e.g. crack and delamination, in metallic and composite structures. The complex interaction between the delamination and propagating wave has been investigated in detail. It has been found that the reflection from the end of the delamination where the wave propagates out is the highest one, which can be measured by sensor practically.

Besides the above mentioned research in this project, a kind of numerical technique, which is used for simulating the wave propagation in elastic media, has been proposed for one-dimensional [11] and two dimensional structures [12]. This numerical method can be used to study the interaction between various damages and wave propagations in the future.

## Reference

1. S.H.D. Valdes and C. Soutis. A structural health monitoring system for laminated composites. *Proceedings of DETC*, Pittsburgh, PA, USA, 2001.
2. H. Sohn and C.R. Farrar. Damage diagnosis using time series analysis of vibration signals. *Smart Materials and Structures*, 10, 1-6, 2001.
3. J.B. Ihn and Fu-Kuo Chang. Built-in diagnostics for monitoring crack growth in aircraft structures. In: Chang, Fu-Kuo (ed.), *Proceedings of the international workshop on structural health monitoring*. Stanford University, USA, 2001.
4. S. Hurlerbaas, M. Niethammer, L.J. Jacobs and C. Valle. Automated methodology to locate notches with Lamb waves. *Acoustics Research Letters Online*, 2, 97-102, 2001.
5. U. Bork, R.E. Challis. Artificial neural networks applied to Lamb wave testing of T-form adhered joints. In: Saffari, N. (ed.), *Proceedings of the Conference on the Inspection of Structural Composites*, Bentham Press, 1994.
6. Z. Su, and L. Ye. Lamb wave propagation-based damage identification for quasi-isotropic CF/EP composite laminates using artificial neural algorithm, Part-I: methodology and database development. *Journal of Intelligent Material Systems and Structures*, 16, 97-111, 2004.
7. C. Zang, M.I. Friswell and M. Imregun. Structural damage detection using independent component analysis. *Structural Health Monitoring: An International Journal*. 3(1), 69-83, 2004.
8. S. Grondel, C. Paget, C. Delebarre, J. Assaad, and K. Levin. Design of optimal configuration for generating  $A_0$  Lamb mode in a composite plate using piezoelectric transducers. *Journal of the Acoustical Society of America*, 112, 84-90, 2002.
9. N. Hu, T. Shimomukai, H. Fukunaga and Z. Su. Damage Identification of Metallic Structures Using  $A_0$  Mode of Lamb Waves. *Structural Health Monitoring: An International Journal* (in press)
10. N. Hu, T. Shimomukai, C. Yan and H. Fukunaga. Delamination detection of cross-ply laminated composite beams using  $S_0$  Lamb mode. *Compos. Sci. Technol.* (in press)
11. N. Hu, H. Fukunaga, M. Kameyama, D. Roy Mahapatra and S. Gopalakrishnan. Analysis of Wave Propagation in Beams with Transverse and Lateral Cracks using a Weakly Formulated Spectral Method. *J. Appl. Mech. (ASME)*, 74, 119-127, 2007.
12. N. Hu, H.H. Wang, B. Yan, H. Fukunaga, D. Ray Mahapatra and S. Gopalakrishnan. The partition of unity finite element method for elastic wave propagation in Reissner-Mindlin plates. *Int. J. Numer. Meth. Engrg.*, 17(12), 1451-1479, 2007.



## Conclusions

In this project, two structural health monitoring techniques have been developed:

**One** is a “**passive element**” based on the impact force identification combined with a database. An efficient impact force identification technique without resort to numerical models has been developed. This identification technique for impact force history and location has been verified for various cases, such as CFRP flat plates, CFRP stiffened panels under simple and multiple-loading. This technique is also effective when there are some small impact-induced damages. To construct the database for predicting the impact-induced damages, a powerful numerical model based on the finite element method for predicting the impact-induced damages has been built up. This numerical method has been used to predict the delamination propagations in a DCB problem and low-velocity impact problem. Then, a database can be set up easily by using the powerful numerical model with the help of experimental data. This database can quickly evaluate the impact-induced damages in composites by employing the identified impact force.

**Another** is an “**active element**”, i.e., a Lamb wave based structural health monitoring technique without baseline data, has been developed which is used in metallic and composite structures.  $A_0$  mode is used for metallic structures with cracks or hole and two kinds of generating methods of  $A_0$  mode have been proposed.  $S_0$  mode has been used for composite laminated beam with a delamination. The damage position can be exactly identified when using the reflected wave from the damage and wave propagating speed. For the case of composites, the complex interaction between the delamination and the propagating wave has been investigated in detail, and the position of delamination where the strongest reflections happen has been clarified.

. These two stable and reliable structural health monitoring techniques will be applied to practical situations in our future research.

## Technical Papers

1. M. Tajima, N. Hu and H. Fukunaga. Experimental impact force identification of CFRP stiffened panels. *Proc. of ICCM16, 223104 CD-ROM*, 2007.
2. H. Fukunaga, T. Umino and N. Hu. Impact force identification of CFRP stiffened panel under multiple loading. *Int. Workshop on Structural Health Monitoring*, 2007 (in press).
3. N. Hu, S. Matsumoto, R. Nishi and H. Fukunaga. Identification of Impact Forces on Composite Structures Using an Inverse Approach. *STRUCTURAL ENGINEERING AND MECHANICS, An International Journal* (in press).
4. N. Hu, T. Shimomukai, H. Fukunaga and Z. Su. Damage Identification of Metallic Structures Using  $A_0$  Mode of Lamb Waves. *Structural Health Monitoring: An International Journal* (in press)
5. N. Hu, T. Shimomukai, C. Yan and H. Fukunaga. Delamination detection of cross-ply laminated composite beams using  $S_0$  Lamb mode. *Compos. Sci. Technol.* (in press)

# EXPERIMENTAL IMPACT FORCE IDENTIFICATION OF CFRP STIFFENED PANELS

Masanori Tajima\*, Ning Hu\*\*, Hisao Fukunaga\*\*  
 \*ESTECH Corp., \*\*Tohoku University

**Keywords:** identification, stiffened panel, impact force, experiment, drop-weight test, delamination

## Abstract

An experimental identification method of impact force location and history acting on CFRP laminated plates is presented. The relation between force histories and strain responses is first determined experimentally by using measured force histories and the corresponding strain responses at the discrete points. By employing this relation, the location and history of impact force is identified using measured strain responses based on the mathematical programming method. The validity of the present identification method has been verified through the impact test of CFRP laminated plate with embedded PZT piezoelectric sensors and CFRP stiffened panel using biaxial strain gauges attached on the surface of the panel. The method is also applied to the impact force identification of CFRP plate involving impact damages such as delamination.

## 1 Introduction

External impact events give severe damage to composite structures and may cause a catastrophic fracture of structures. The mechanical properties of composite structures such as compression-after-impact (CAI) strength [1] may degrade severely after external impact events. Modern techniques of structural health monitoring are a possible resort to insure the safety of composite structures. The identification of the external impact forces is important for structural health monitoring and has been investigated by many researchers [2-8]. For instance, Wu et al. [2] reported the identification results of impact forces on various plates based on the relation between the impact force and the strain response. Seydel et al. [3] identified the location and history of the impact force acting on stiffened composite panels. The authors [4-7] proposed a technique to identify the location and history of

impact forces based on a finite element method. However, it is difficult to construct a precise analytical model on complicated structures such as aircraft wings and fuselages. Then it is important to develop the impact force identification method using only experimental data without resorting to an analytical model.

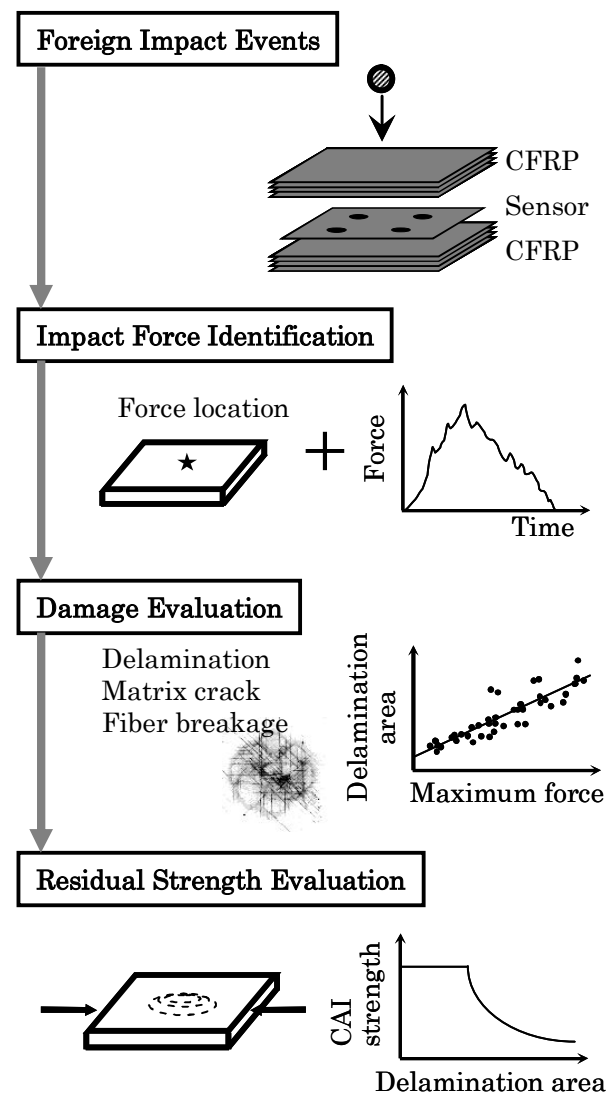


Fig. 1 Schematic view of damage monitoring

The present paper discusses a feasibility of a damage monitoring method of CFRP structures based on impact force identification as shown in Fig. 1. Especially this paper examines an experimental identification method of impact forces acting on CFRP structures. The experimental relation between force histories and strain responses is first determined by using measured force histories and the corresponding strain responses. The location and history of impact force is identified based on this relation. The validity of the present identification method has been verified through the impact test of CFRP flat plate and CFRP stiffened panel with an impulse hammer. The method is also applied to the drop-weight impact test of CFRP plate.

## 2 Identification Method

### 2.1 Force-Strain Relation

In a low-velocity impact event, the relation between an impact force history acting at the location  $(x_f, y_f)$  and a strain response observed at the location  $(x_o, y_o)$  can be expressed in the following algebraic equation:

$$\{\tilde{\varepsilon}\} = [G(x_f, y_f, x_o, y_o)]\{\tilde{f}\} \quad (1)$$

where the strain and force histories are expressed at a discrete time, and  $[G(x_f, y_f, x_o, y_o)]$  is a transform matrix composed of the Green's function at each time, which is a lower triangular matrix [2] as follows:

$$\begin{Bmatrix} \varepsilon_1 \\ \varepsilon_2 \\ \varepsilon_3 \\ \vdots \\ \varepsilon_n \end{Bmatrix} = \begin{bmatrix} g_1 & & & & \\ g_2 & g_1 & & & 0 \\ g_3 & g_2 & g_1 & & \\ \vdots & \vdots & \vdots & \ddots & \\ g_n & g_{n-1} & g_{n-2} & \cdots & g_1 \end{bmatrix} \begin{Bmatrix} f_1 \\ f_2 \\ f_3 \\ \vdots \\ f_n \end{Bmatrix} \quad (2)$$

where  $g_i$  is a component of a transform matrix which is determined by the force location and the observation point of strain only, and is not influenced by the force history.

Eq. 2 is transformed into the following equation:

$$\begin{Bmatrix} \varepsilon_1 \\ \varepsilon_2 \\ \varepsilon_3 \\ \vdots \\ \varepsilon_n \end{Bmatrix} = \begin{bmatrix} f_1 & & & & \\ f_2 & f_1 & & & 0 \\ f_3 & f_2 & f_1 & & \\ \vdots & \vdots & \vdots & \ddots & \\ f_n & f_{n-1} & f_{n-2} & \cdots & f_1 \end{bmatrix} \begin{Bmatrix} g_1 \\ g_2 \\ g_3 \\ \vdots \\ g_n \end{Bmatrix} \quad (3)$$

Eqs. 2 and 3 can be expressed as follows:

$$\{\tilde{\varepsilon}\} = [G]\{\tilde{f}\} = [F]\{g\} \quad (4)$$

The components of a transform matrix,  $\{g\}$ , is determined using the force histories  $\{\tilde{f}\}$  and measured strain responses  $\{\tilde{\varepsilon}\}$  in an impact test with an impulse hammer. Several times of tests are performed to avoid measurement errors in the determination of  $\{g\}$ . Then the components of the transform matrix can be obtained by applying the least-squares method [8]:

$$\underset{\{g\}}{\text{minimize}} H = \sum_{k=1}^K \|\{\tilde{\varepsilon}\} - [F]\{g\}\|^2 \quad (5)$$

In CFRP laminated plates, we use PZT piezoelectric sensors embedded in the plate as strain sensors. When we consider a thin circular PZT element attached on or embedded in structures, the output voltage  $V_{PZT}$  is proportional to the summation of in-plane strains,  $\varepsilon_x + \varepsilon_y$  as follows [4]:

$$V_{PZT}(t) = G_{PZT} \{\varepsilon_x(t) + \varepsilon_y(t)\} \quad (6)$$

where  $G_{PZT}$  is the sensitivity of PZT element as a strain sensor. The sensitivity of PZT sensors is calibrated using strain gauges through an impact test.

### 2.2 Force Identification

As the transform matrix in Eq. 1 is determined, the impact force acting on CFRP plates is determined using measured strains at the multi-point PZT sensors in the case of that the force location is known [4]. The force history can be identified using a minimization problem as follows:

$$\begin{aligned} \underset{\{\tilde{f}\}}{\text{minimize}} \quad & F = \sum_{i=1}^m \|\{\tilde{\varepsilon}_i\} - [G_i]\{\tilde{f}\}\|^2 \\ \text{subject to} \quad & \{\tilde{f}\} \geq 0 \end{aligned} \quad (7)$$

where  $\{\tilde{\varepsilon}_i\}$  is the strain responses measured by the  $i$ -th sensor located at  $(x_{oi}, y_{oi})$ ,  $[G_i]$  is the transform matrix relating  $\{\tilde{\varepsilon}_i\}$  to  $\{\tilde{f}\}$ , and  $m$  is the number of sensors. The constraint in Eq. 7 is to ensure the force to be compressive all the time. Then the force history identification is achieved by solving Eq. 7 by means of the quadratic programming method in this study.

Another issue is the determination of the force location. In the force history identification at the

assumed location  $(x_e, y_e)$ , we can have a force history denoted by  $\{\tilde{f}_e\}$ . Then an error vector, which indicates the deviation between the estimated strains and measured strains, can be defined. The force location is determined by solving a minimization problem as follows:

$$\underset{x_e, y_e}{\text{minimize}} \quad E = \sum_{i=1}^m \frac{\| [G_i] \{\tilde{f}_e\} - \{\tilde{\varepsilon}_i\} \|^2}{\| \{\tilde{\varepsilon}_i\} \|^2} \quad (8)$$

Eq. 8 is solved by a nonlinear programming method [9]. In the minimization process, the force history  $\{\tilde{f}_e\}$  is updated using Eq. 7 for each force location.

### 3 Identification Test

#### 3.1 Identification System

To verify the identification method stated in the previous section, the impact test for CFRP laminated plate and stiffened panel has been performed. The impact test system and the specimen utilized in this study are shown in Figs. 2 and 3, respectively. The impact test system consists of a measurement part and identification codes as shown in Fig. 2. The former part consists of a sensor network and several signal conditioners. The present study utilizes the SMART Layer developed in Stanford University as a part of the sensor network as shown in Fig. 3. The specimen is cantilevered and impacted by an impulse hammer. The strain response is measured using four PZT sensors for laminated plates.

The identification task is carried out intermittently. When the impact force is applied and the strain responses are induced, a trigger signal is sent to the computer from the oscilloscope. After

receiving the trigger signal, the computer imports the strain responses from the oscilloscope, then identify the impact force and monitor the strain responses again. In this test, the measurement time and the sampling time are  $10.0 \times 10^{-3}$  second and  $1.0 \times 10^{-4}$  second, respectively. The force history is also measured from the output of impulse hammer in order to verify an identified force history.

#### 3.2 Impact Test for CFRP Laminated Plates

The material properties of the specimen are shown in Table 1. In order to determine the sensitivity of the PZT sensors, the calibration is performed by comparing the output voltage of the PZT sensor with the output of the biaxial strain gauge located at the same point. The sensitivity  $G_{PZT}$  in Eq. 6 was determined by comparing the maximum and minimum peak values of the output voltages [4].

Fig. 4 shows the impact points used to determine the transform matrix in Eq. 1 where the number of sensors is 4. The transform matrix is constructed for each combination of impact point and sensor point through four times of impact tests with an impulse hammer. The transform matrix is interpolated at points except impact points using a shape function similar to one used in a finite element method.

Table 1. Material properties of CFRP plates

Stacking sequence	Material properties of unidirectional lamina
$[45_2/-45_4/45_2]_s$ $[0_2/45_2/-45_2/90_2]_s$	$E_1 = 114 \text{ GPa}$ , $E_2 = 9.20 \text{ GPa}$ $G_{12} = 5.49 \text{ GPa}$ $\nu_{12} = 0.30$ , $\rho = 1550 \text{ kg/m}^3$

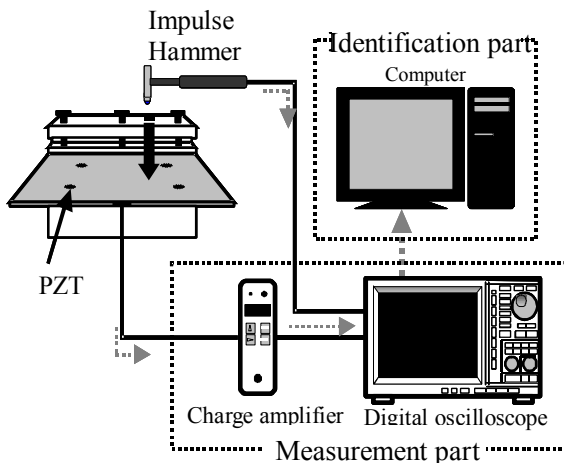


Fig. 2. Impact test system

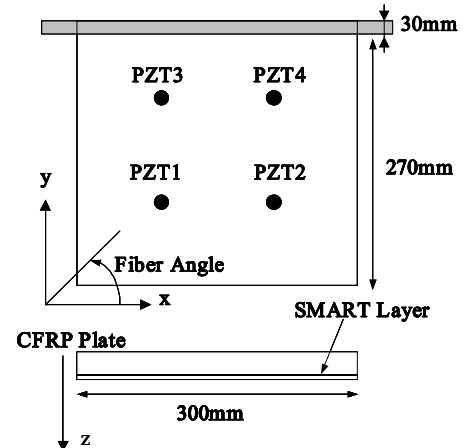


Fig. 3 CFRP specimen with PZT sheet

### 3.3 Identification Results

The impact force is identified using the output of four PZT sensors embedded in CFRP laminates. The force location is determined by Eq. 8. Fig. 5 shows the identification results of the force location for  $[45_2/-45_4/45_2]_s$  laminate and  $[0_2/45_2/-45_2/90_2]_s$  laminate.

In Fig. 5, each circle involves the true (measured) and identified force locations. The average errors of the force location were 2.7 mm for  $[45_2/-45_4/45_2]_s$  laminate and 3.1 mm for  $[0_2/45_2/-45_2/90_2]_s$  laminate, respectively. These are around 1% of the plate size in length. The location error in

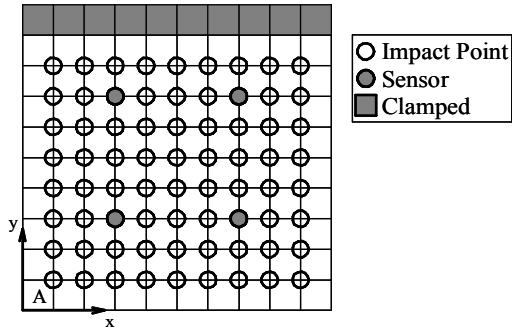
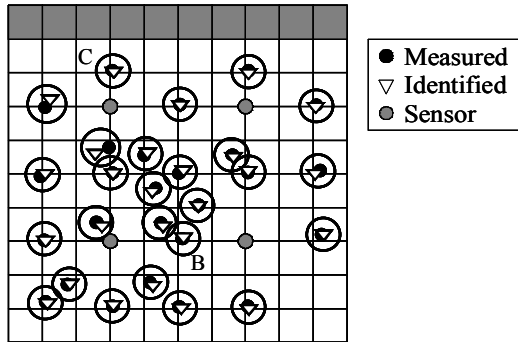
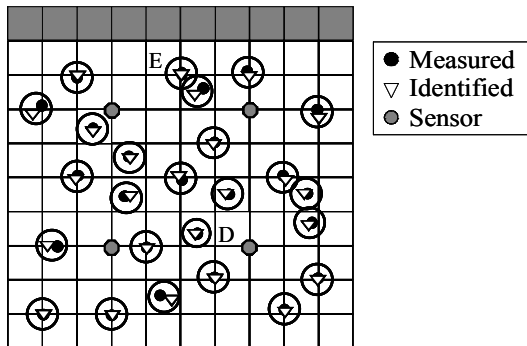


Fig. 4. Impact points used to determine a transform matrix



(a)  $[45_2/-45_4/45_2]_s$  laminate



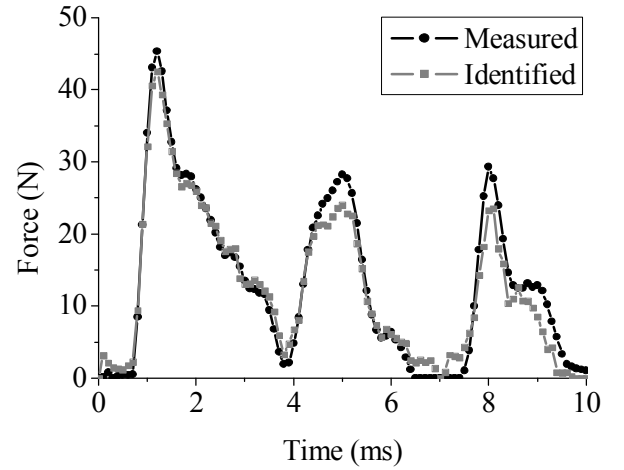
(b)  $[0_2/45_2/-45_2/90_2]_s$  laminate

Fig. 5. Identified force locations for CFRP laminated plates

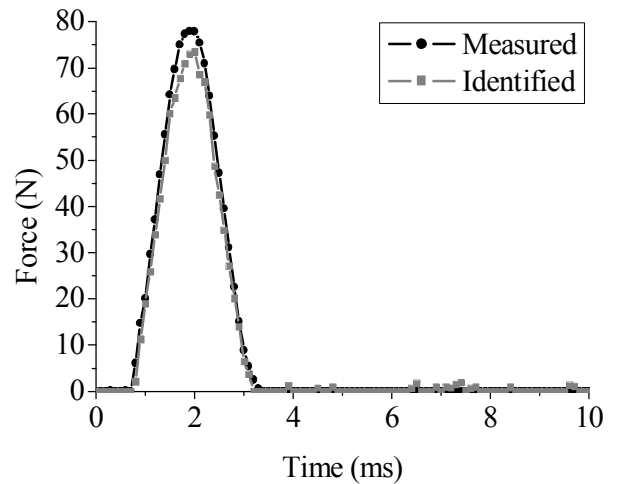
the present method is smaller compared with 8.5 mm for  $[45_2/-45_4/45_2]_s$  laminate and 4.1 mm for  $[0_2/45_2/-45_2/90_2]_s$  laminate in the previous method based on FEM modeling [4] since the present method can avoid the modeling error in the construction of the transform matrix.

Fig. 6 shows the identified force histories at the points B and C for  $[45_2/-45_4/45_2]_s$  plate, respectively. In these cases, the force locations are identified near the true ones, and therefore the identified force histories agree well with the true ones.

In the present force identification, it takes a few seconds to identify the location and history for each case. Almost identification time is consumed in the force location identification.



(a) Point B



(b) Point C

Fig. 6. Identified force histories for  $[45_2/-45_4/45_2]_s$  laminate

### 3.4 Impact Test for CFRP Stiffened Panel

Next we consider Carbon/PEEK stiffened panel as shown in Fig. 7. The laminate sequence of stiffener and skin are  $[45/-45/-45/45/0_4/90/45_3]_s$  and  $[45/-45/-45/45/0/90]_s$ , respectively. The impact points and the sensor locations are shown in Fig.8 where the impact point with the impulse hammer is located at the skin side and the strain responses are measured by using 8 biaxial strain gauges attached on the surface of the stiffener side. The transform matrix is determined using the measured force histories and strain responses in an impact test with an impulse hammer.

### 3.5 Identification Results

The force location is determined by Eq. 8. Fig. 9 shows the identification results of the force location. Each circle involves the true (measured) and identified force locations. The average errors of the force location were 9.2 mm, and those are 1% of the panel length or 3% of the region A in Fig. 7. The location error at the point B with the stiffener is 11.5 mm and that at the point C without the stiffener is 3.2 mm. The difference of location errors with and without the stiffener is not so large.

Figs. 10 and 11 show the identified force histories in the case of the points B and C for CFRP stiffened panel. The identification error of force history at the point B is a little large since the location error is relatively large. On the contrary, the identification error of force history at the point C is small, and the force history as well as the force location is accurately identified.

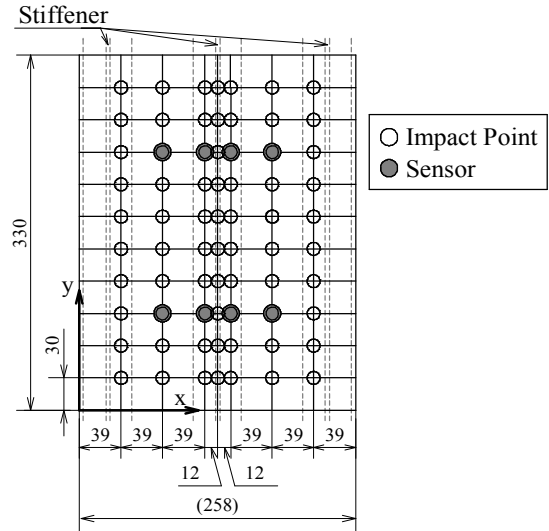


Fig. 8. Impact points and sensor locations (enlargement of the region A in Fig. 7)

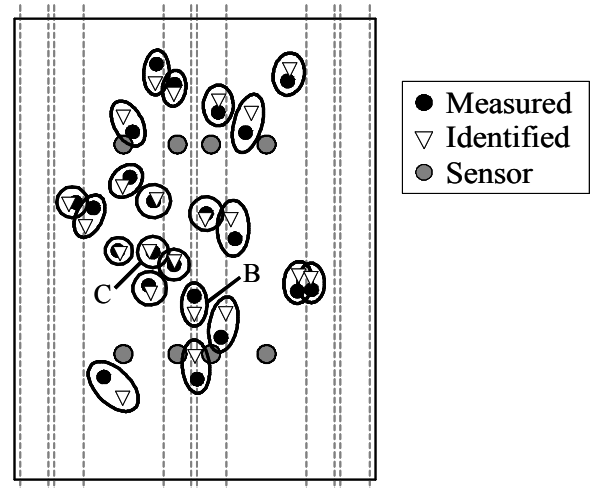


Fig. 9. Identified force location for CFRP stiffened panel

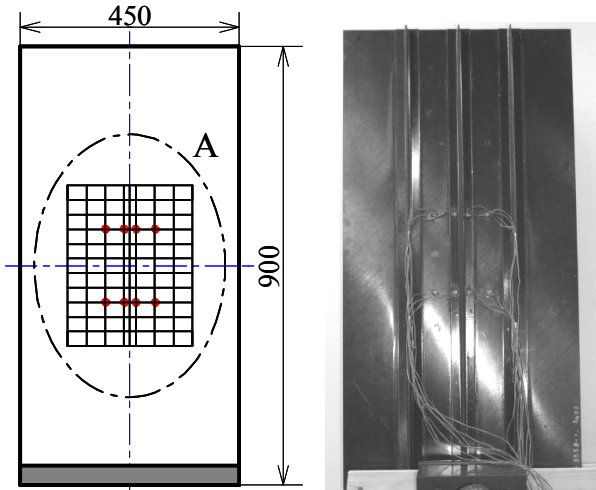


Fig. 7. Impact test of CFRP stiffened panel

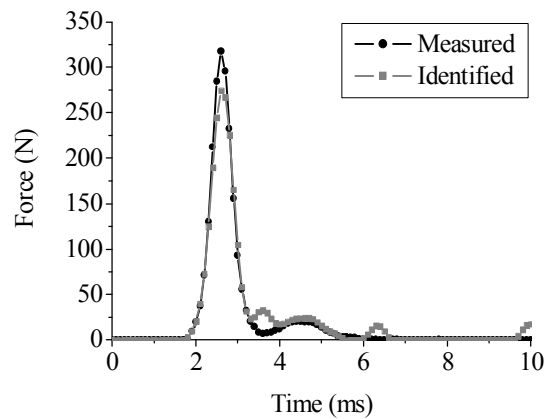


Fig. 10. Identified force history for CFRP stiffened panel (Point B)



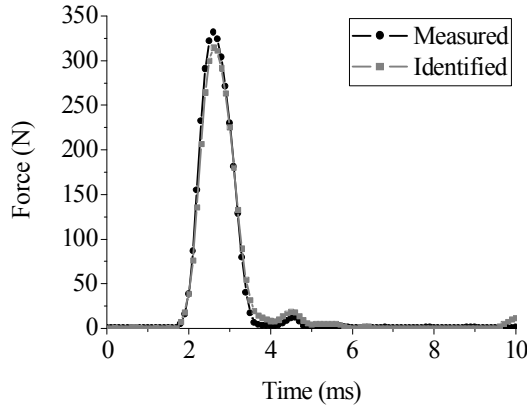


Fig. 11. Identified force history for CFRP stiffened panel (Point C)

#### 4 Identification in Drop-weight Impact Test

In the present identification method, we assume that there is no damage in structures, and we use a transform matrix of a healthy structure. We consider the impact force identification in a drop-weight impact test where the impact damage is induced within the laminate.

Fig. 12 shows the specimen of CFRP laminated plates used in drop-weight impact test where the laminate configuration of CFRP plates is  $[(45/0/-45/90)_4]_s$  and the mass and the tip radius of an impactor is 4.7 kg and 15.8 mm, respectively. The center of the plate is impacted by drop-weight. Four biaxial strain gauges are attached on the upper surface of the plate. As energy levels in an impact test, 3.0 J, 4.8 J and 7.2 J were used where there was no damage in the laminate for the case of 3.0 J impact energy. By employing the experimental transform matrix for the impact case of 3.0 J, the impact force is identified using measured strains for the impact cases of 4.8 J and 7.2 J.

Figs. 13 and 14 show the identified impact force histories for 4.8 J and 7.2 J cases, respectively. The identified force histories agree well with the true ones. The damage areas by ultrasonic C-scan are also shown in the figures. The diameter of the damage area is 16mm for 4.8 J case and 27 mm for 7.2 J case, respectively, and is not so large in both cases. When the damage extent is not so large, we can identify the force history using a transform matrix of a healthy structure.

Real-time monitoring of the impact events is one of the most important health monitoring. The present method of the force identification gives the location and history of the impact force acting on composite structures. We can get the information of impact events in real time since it takes only a few

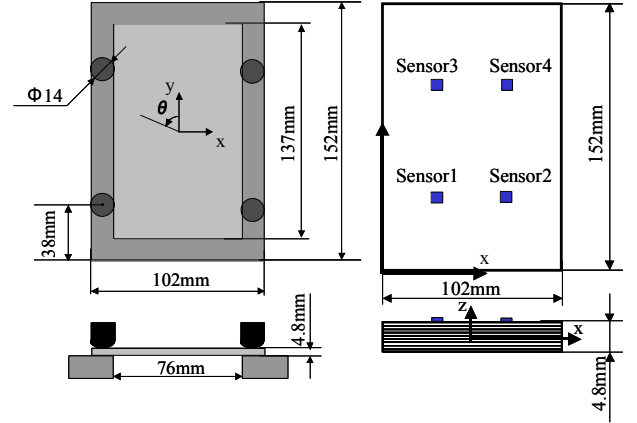


Fig. 12 Specimen of drop-weight impact test

seconds to identify impact events. When we can know the location and history of the impact force, we can evaluate the residual or strength as well as the damage state as shown in Fig. 1, using an analytical or experimental database of CFRP structures.

#### 5 Conclusions

In this paper, the experimental identification method of the impact force location and force history is developed. The validity of the present method is verified through impact tests for the CFRP flat plates and the stiffened panel, and a drop-weight impact test of CFRP laminated plates. The knowledge from these results is summarized as follows:

- (1) The accurate force location and force history can be identified using the present experimental identification method for both of CFRP flat plate and stiffened panel.
- (2) The present force identification method is based on the experimental transform matrix to relate the impact force and the measured strain. Thus the method can be applicable easily to complicated structures such as composite wing and fuselage structures.
- (3) The present force identification method using a transform matrix of a healthy structure can be applicable to the case of that a small size of impact damage is induced.
- (4) Using identified force location and force history, evaluation of the impact damage and the residual strength of composite structures is possible in real-time.



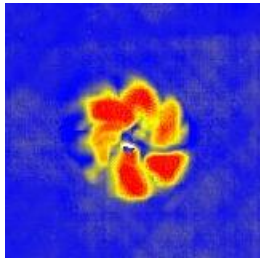
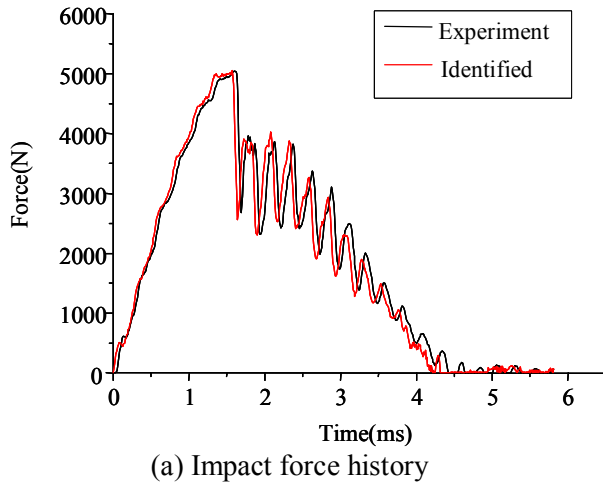


Fig. 13. Identified force history for 4.8 J case

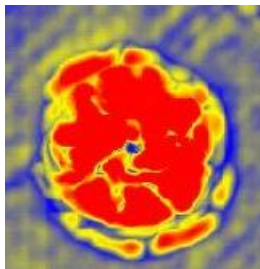
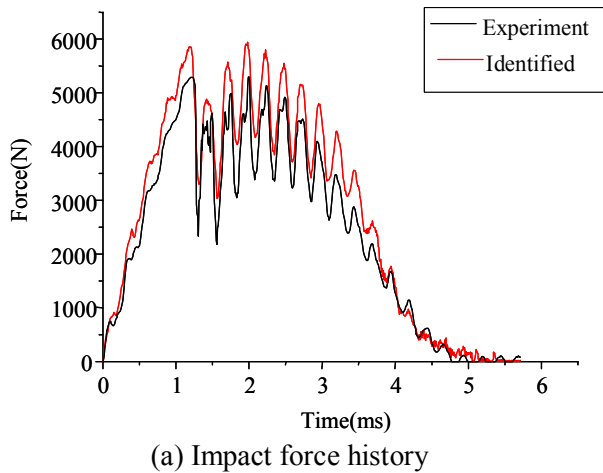


Fig. 14. Identified force history for 7.2 J case

### Acknowledgement

The authors wish to acknowledge the financial support provided for this ongoing research by AFOSR, AOARD-06-4066. They also acknowledge their experimental help of Mr. Eiichi Hara of Japan Aero Space Technology, Mr. Sunao Sugimoto and Mr. Masamichi Matsushima of Japan Aerospace Exploration Agency.

### References

- [1] Ishikawa, T., Sugimoto, S., Matsushima, M. and Hayashi, Y. "Some experimental findings in compression-after-Impact (CAI) tests of CF/PEEK (APC-2) and conventional CF/Epoxy flat plates". *Comp. Sci. Tech.*, Vol.55, pp 349-363, 1995.
- [2] Wu, E., Yeh, J. C. and Yen, C. S. "Identification of impact forces at multiple locations on laminated plates". *AIAA J.*, Vol.32, pp 2433-2439, 1994.
- [3] Seydel, R. and Chang, F. K. "Impact identification of stiffened composite panels". *Smart Mater. Struct.*, Vol.10, pp 354-369 & 370-379, 2001.
- [4] Fukunaga, H., Matsumoto, S. and Hu, N. "Real-time impact force identification of CFRP structures using piezoelectric sensors". *Proc. 24th ISTS*, pp 286-291, 2004.
- [5] Tajima, M., Matsumoto, S. and Fukunaga, H. "Impact force identification of CFRP laminated plates using PZT piezoelectric sensors". *Trans. Japan Soc. Mech. Eng., Part A*, Vol.70, pp.1566-1573 & 1747-1754 (in Japanese), 2004.
- [6] Hu, N. and Fukunaga, H. "A new approach for health monitoring of composite structures through identification of impact force". *J. Advanced Science*, Vol.17, pp 82-89, 2005.
- [7] Hu, N., H. Fukunaga, S. Matsumoto, B. Yan and X. H. Peng. "An efficient approach for identifying impact force using embedded piezoelectric sensors". *Int. J. Impact Engineering*, Vol.34, pp 1258-1271, 2007.
- [8] Fukunaga, H. and N. Hu. "Experimental impact force identification of composite structures". *Proc. Third European Workshop on Structural Health Monitoring 2006*, A. Guemes ed., DES Tech Pub., pp 840-847, 2006.
- [9] Vanderplaats, G. N. and Sugimoto, H. "A general purpose optimization program for engineering design". *Computers Structures*, Vol.24, pp 13-21, 1986.

## **Paper 2**

Title: Impact Force Identification of CFRP Stiffened Panel under Multiple Loading

Authors: Hisao Fukunaga  
Takao Umino  
Ning Hu

The 6th International Workshop on Structural Health Monitoring  
2007/9, Stanford University, in press

## **ABSTRACT**

An experimental identification method of impact force location and history acting on CFRP stiffened panels is presented. The relation between force histories and strain responses under single loading is first determined experimentally by using measured force histories with impulse hammer and the corresponding strain responses at the discrete points. By employing this relation, the locations and histories of multiple impact forces is identified using measured strain responses based on the mathematical programming method. The validity of the present identification method has been verified through the impact test of CFRP stiffened panels using biaxial strain gauges attached on the surface of the panel. The accurate force location and force history can be identified for both single and multiple loading.

## **INTRODUCTION**

External impact events give severe damage to composite structures and may cause a catastrophic fracture of structures. The mechanical properties of composite structures such as compression-after-impact (CAI) strength may degrade severely after external impact events. Modern techniques of structural health monitoring are a possible resort to insure the safety of composite structures. The identification of the external impact forces is important for structural health monitoring and has been investigated by many researchers [1-6]. For instance, Wu et al. [1] reported the identification results of impact forces on various plates based on the relation between the impact force and the strain response. Seydel et al. [2] identified the location and history of the impact force acting on stiffened composite panels. The authors [3-5] proposed a technique to identify the location and history of impact forces based on the relation between force histories and strain responses formulated by a finite element method. However, it is difficult to construct a precise analytical model on complicated structures such as aircraft wings and fuselages. Then it is

---

Hisao Fukunaga, Takao Umino and Ning Hu, Department of Aerospace Engineering,  
Tohoku University, Aramaki 01, Aoba-ku, Sendai 980-8579 JAPAN

important to develop the impact force identification method using only experimental data without resorting to an analytical model.

The present paper proposes an experimental identification method of impact force acting on CFRP stiffened panels. The experimental relation between force histories and strain responses is first determined by using measured force histories with impulse hammer and the corresponding strain responses [6]. The location and history of impact force is identified based on this relation. The validity of the present identification method has been verified through the impact test of CFRP stiffened panels under single and multiple loading.

## IDENTIFICATION METHOD OF IMPACT FORCE

### Relation between Impact Force and Measured Strains

In the low-velocity impact event, the relation between the impact force history acting at the location  $(x_f, y_f)$  and the strain response observed at the location  $(x_o, y_o)$  can be expressed in the following algebraic equation:

$$\{\tilde{\varepsilon}\} = [G(x_f, y_f, x_o, y_o)]\{\tilde{f}\} \quad (1)$$

where the strain and force histories are expressed at discrete time, and  $[G(x_f, y_f, x_o, y_o)]$  is a transfer matrix composed of the Green's function at each time, which is a lower triangular matrix [1] as follows:

$$\begin{Bmatrix} \varepsilon_1 \\ \varepsilon_2 \\ \varepsilon_3 \\ \vdots \\ \varepsilon_n \end{Bmatrix} = \begin{bmatrix} g_1 & & & & \\ g_2 & g_1 & & & 0 \\ g_3 & g_2 & g_1 & & \\ \vdots & \vdots & \vdots & \ddots & \\ g_n & g_{n-1} & g_{n-2} & \cdots & g_1 \end{bmatrix} \begin{Bmatrix} f_1 \\ f_2 \\ f_3 \\ \vdots \\ f_n \end{Bmatrix} \quad (2)$$

where  $\{g\}$  is a component of a transfer matrix which is determined by the force location and the observation point of strain only, and is not influenced by the force history.

Eq. (2) is transformed into the following equation:

$$\begin{Bmatrix} \varepsilon_1 \\ \varepsilon_2 \\ \varepsilon_3 \\ \vdots \\ \varepsilon_n \end{Bmatrix} = \begin{bmatrix} f_1 & & & & \\ f_2 & f_1 & & & 0 \\ f_3 & f_2 & f_1 & & \\ \vdots & \vdots & \vdots & \ddots & \\ f_n & f_{n-1} & f_{n-2} & \cdots & f_1 \end{bmatrix} \begin{Bmatrix} g_1 \\ g_2 \\ g_3 \\ \vdots \\ g_n \end{Bmatrix} \quad (3)$$

Eqs. (2) and (3) can be expressed as follows:

$$\{\tilde{\varepsilon}\} = [G]\{\tilde{f}\} = [F]\{g\} \quad (4)$$

The component of a transfer matrix,  $\{g\}$ , can be determined using the force histories  $\{\tilde{f}\}$  and measured strain responses  $\{\tilde{\varepsilon}\}$  in an impact test with an impulse hammer. Several times of tests are performed to avoid the measurement errors in the determination of  $\{g\}$ . Then the component of a transfer matrix can

be obtained by applying the least-squares method:

$$\min_{\{g\}} H = \sum_{k=1}^K \left\| \{\tilde{\varepsilon}\} - [F]\{g\} \right\|^2 \quad (5)$$

In this paper, we use bi-axial strain gauges attached on the surface of CFRP stiffened panel as strain sensors.

### Force History Identification

When the transfer matrix in Eq.(1) is determined, the impact force acting on CFRP stiffened panels under single or multiple loading is determined using measured strains at the multi-point strain gauges in the case that the force location is known [3]. The force history can be identified using a minimization problem as:

$$\begin{aligned} \text{Minimize}_{\{\tilde{f}\}} \quad & F = \sum_{i=1}^m \left\| \{\tilde{\varepsilon}_i\} - [G_i]\{\tilde{f}\} \right\|^2 \\ \text{subject to} \quad & \{\tilde{f}\} \geq 0 \end{aligned} \quad (6)$$

where  $\{\tilde{\varepsilon}_i\}$  is the strain responses measured by the  $i$ th sensor located at  $(x_{0i}, y_{0i})$ ,  $[G_i]$  is the transfer matrix relating  $\{\tilde{\varepsilon}_i\}$  to  $\{\tilde{f}\}$ , and  $m$  is the number of sensors. In the single loading case,  $\{\tilde{f}\}$  shows the force history of the single loading. In the multiple loading case, for example, in the two-point loading case,  $\{\tilde{f}\}$  shows the  $\{\tilde{f}_1^T, \tilde{f}_2^T\}^T$  where  $\tilde{f}_1$  and  $\tilde{f}_2$  are the force histories of two loading.

The constraint in Eq. (6) is to ensure the force to be compressive all the time. Then the force history identification is achieved by solving Eq. (6) by means of the quadratic programming method in this study.

### Force Location Identification

Another issue is the determination of the force location. In the force history identification at the assumed location, we can have a force history denoted by  $\{\tilde{f}_e\}$ . Then an error vector, which indicates the deviation between the estimated strains and measured strains, can be defined. The force location for the single loading case is determined by solving a minimization problem as follows:

$$\min_{x_e, y_e} E = \sum_{i=1}^m \frac{\left\| [G_i]\{\tilde{f}_e\} - \{\tilde{\varepsilon}_i\} \right\|^2}{\left\| \{\tilde{\varepsilon}_i\} \right\|^2}. \quad (7)$$

In the multiple loading case, the force locations of multiple loading are used as design variables. Eq. (7) is solved by the DFP nonlinear programming method [7]. In the minimization process, Eqs. (6) and (7) are solved iteratively to get the converged results where the force history  $\{\tilde{f}_e\}$  is updated using Eq.(6) for each force location.

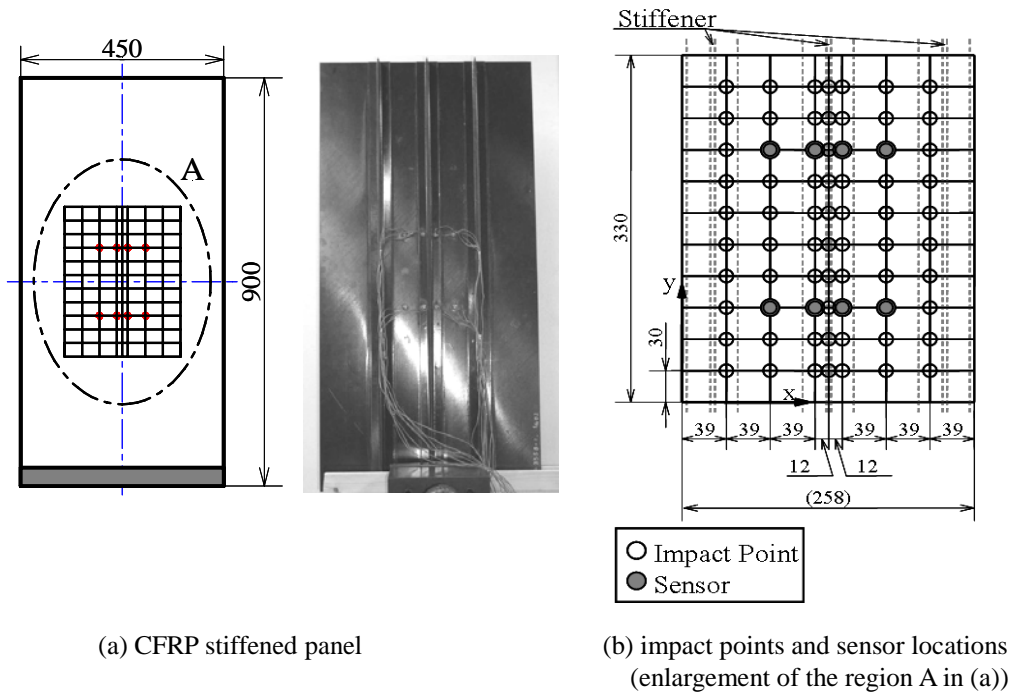
### IDENTIFICATION RESULTS

## Impact Force Identification of CFRP Stiffened Panel under Single Loading

To verify the identification method stated in the previous section, the impact test for Carbon/PEEK stiffened panel has been performed as shown in Figure 1. The impact point and the sensor location are also shown in Figure 1 where the impact point with the impulse hammer is located at the skin side and the strain

TABLE I. LAMINATE SEQUENCE OF CFRP STIFFENED PANEL

Laminate Sequence	
Stiffener	Skin
$[45/-45/-45/45/0_4/90/45_3]_s$	$[45/-45/-45/45/0/90]_s$



(a) CFRP stiffened panel

(b) impact points and sensor locations  
(enlargement of the region A in (a))

Figure 1. Carbon/PEEK stiffened panel.

responses are measured by using 8 biaxial strain gauges attached on the surface of the stiffener side. The transfer matrix is determined using the measured force histories and strain responses in an impact test with an impulse hammer. TABLE I shows laminate sequence of the stiffener and skin in the stiffened panel.

The force location is determined by Eq.(7). Figure 2 shows the identification results of the force location. Each circle involves the true (measured) and identified force locations. The average errors of the force location were 9.2 mm. The location error at the point A with the stiffener is 11.5mm and that at the point B without the stiffener is 3.2mm. The difference of location errors with and without the stiffener is not so large. Figure 3 shows the identified force histories in the case of points A and B in the panel. The identification error of force history at the point A is a little large since the location error is relatively

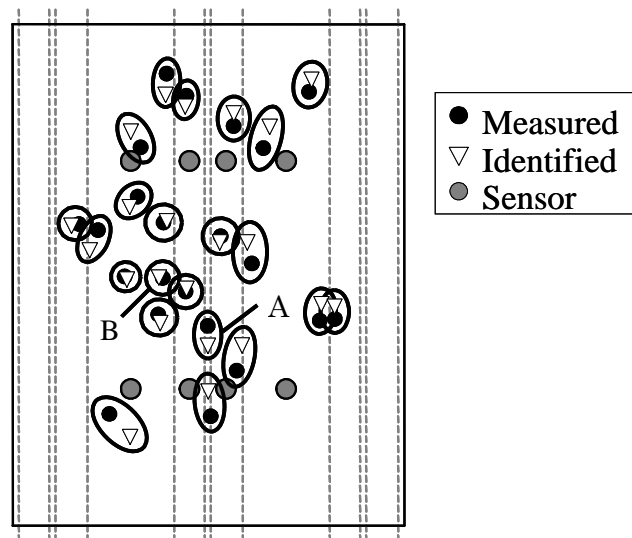
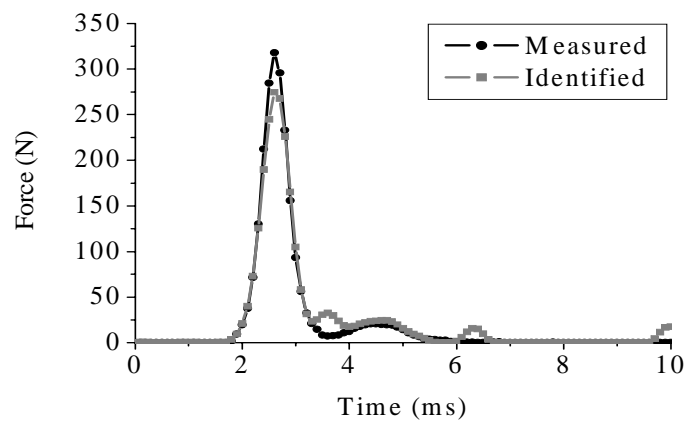
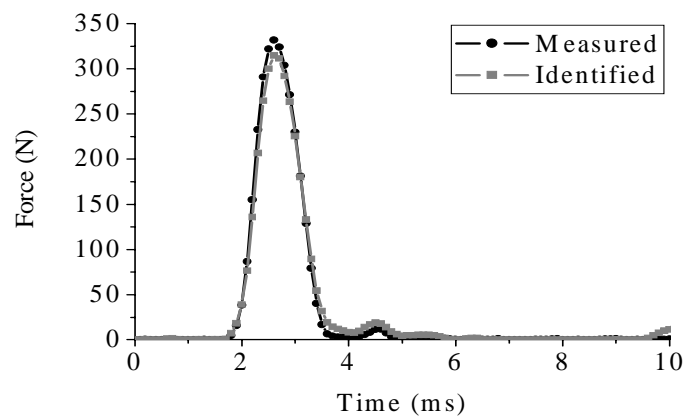


Figure 2. Identified force location for CFRP stiffened panel.



(a) point A



(b) point B

Figure 3. Identified force histories for CFRP stiffened panel.

large. On the contrary, the identification error of force history at the point B is small, and the force history as well as the force location is accurately identified.

In the present force identification, it takes a few seconds to identify the location and history for each case. Almost identification time is required in the force location identification.

### Impact Force Identification of CFRP Stiffened Panel under Multiple Loading

Next we consider the impact force identification for Carbon/Epoxy stiffened panel under multiple loading as shown in Figure 4. The stiffened panel is clamped at the upper and lower edges. The sensor location is shown in Figure 4 where the strain responses are measured by using 8 biaxial strain gauges attached on the surface of the stiffener side. The transfer matrix is determined using the measured force histories and strain responses in an impact test with an impulse hammer. TABLE II shows laminate sequence of the stiffener and skin in the stiffened panel.

In the present impact test, we consider the two-point loading with impulse hammer, and two kinds of impactors were used as tip materials of impulse hammer, i.e., hard tip (aluminum) and soft-tip (plastic). Hard-tip impulse hammer was used to determine the transfer matrix. In the two-point loading, two types of tip materials were used in order to examine the effect of tip stiffness on the force identification results as follows:

Case 1 : hard-tip + hard-tip

Case 2 : hard-tip + soft-tip

TABLE II. LAMINATE SEQUENCE

Skin	$[-45/0/45/90_2/-45/0/45/90]_s$
Flange	$[(-45/90/45/0/-45/90_2/45/90)s/(-45/90/45)_s]$
Web	$[(-45/90/45/0/-45/90_2/45/90)_s]_s$

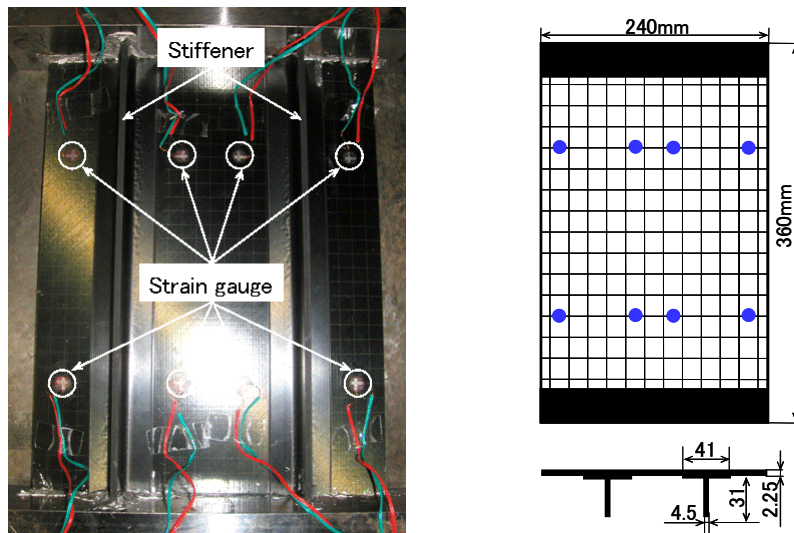


Figure 4. Carbon/Epoxy stiffened panel.



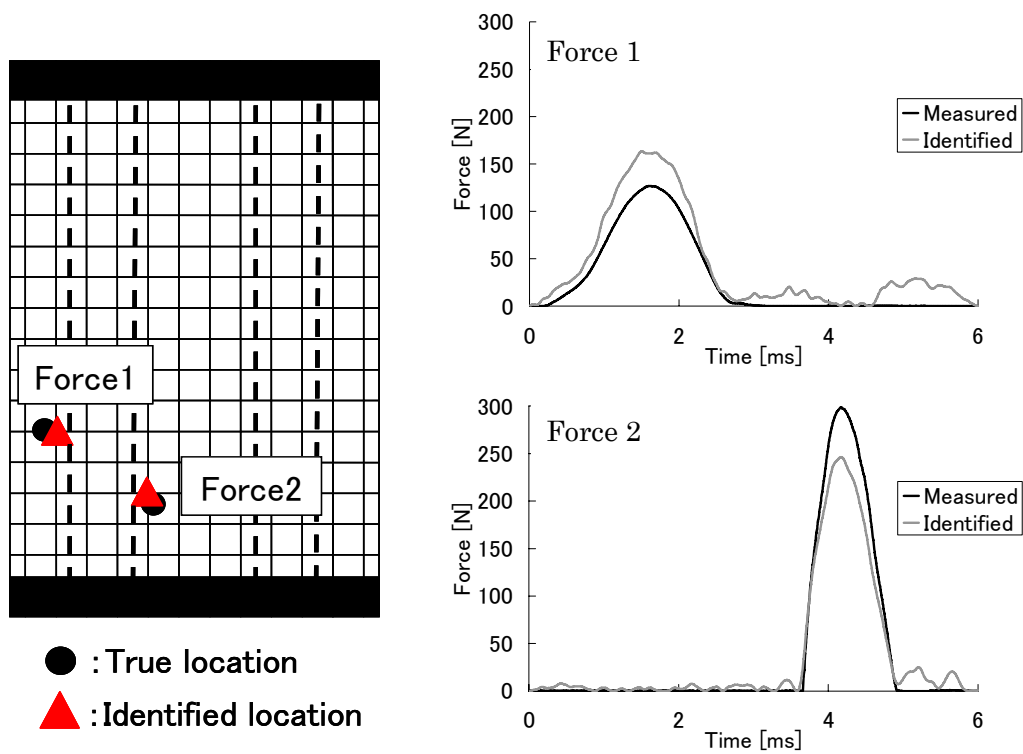


Figure 5. Identification results for case 1.

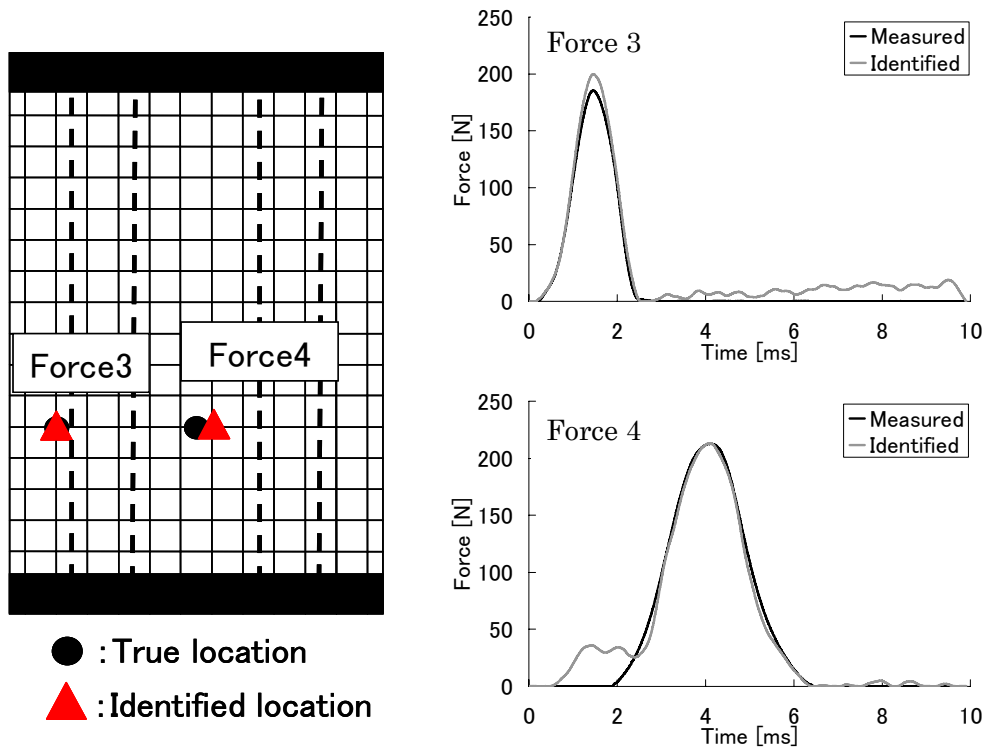


Figure 6. Identification results for case 2.

Figure 5 shows the identification results for the case 1 where the force location and the force histories of two loading, i.e., force 1 and force 2 are shown. The errors of the force location were 8.1mm for force 1 and 9.9mm for force 2. The errors of the maximum force were 29% for force 1 and 17% for force 2. The force location and the force histories are identified well although the results are not so good as compared with the single loading case. Figure 6 shows the identification results for the case 2 where the tip materials of impulse hammer with the different stiffness are used. The errors of the force location were 0.0mm for force 3 and 5.0mm for force 4. The errors of the maximum force were 8% for force 3 and 0% for force 4. The case 2 gives the better results both for the force location and the force histories.

## CONCLUSIONS

In this paper, the method to identify the impact force location and force history is developed by using an experimental transfer matrix relating the force history to the strain response. The identification tests for CFRP stiffened panels have been performed for both cases of single loading and multiple loading. The knowledge from these results are summarized as follows:

- (1) The accurate force location and force history can be identified using the present experimental identification method for both cases of single loading and multiple loading.
- (2) The present force identification method using the experimental transfer matrix can be applied to the complicated structures such as aircraft wings and fuselages since we do not need a mathematical model of structures.

## ACKNOWLEDGEMENTS

This work is partly supported by Grant-in-Aid from Asian Office of Aerospace R& D, No. FA4869-06-1-0076 and from the Ministry of Education, Culture, Sports, Science and Technology of Japan, No. 17360404.

## REFERENCES

1. Wu, E., J. C. Yeh and C. S. Yen. 1994. "Identification of Impact Forces at Multiple Locations on Laminated Plates," *AIAA J.*, 32(12): 2433-2439.
2. Seydel, R. and F. K. Chang. 2001. "Impact Identification of Stiffened Composite Panels," *Smart Mater. Struct.*, 10: 354-369 & 370-379.
3. Tajima, M., S. Matsumoto and H. Fukunaga. 2004. "Impact Force Identification of CFRP Laminated Plates Using PZT Piezoelectric Sensors," *Trans. Japan Soc. Mech. Eng., Part A*, 70: 1566-1573 & 1747-1754 (in Japanese).
4. Hu, N. and H. Fukunaga. 2005. "A New Approach for Health Monitoring of Composite Structures through Identification of Impact Force," *J. Advanced Science*, 17: 82-89.
5. Hu, N., H. Fukunaga, S. Matsumoto, B. Yan and X. H. Peng. 2007. "An Efficient Approach for Identifying Impact Force Using Embedded Piezoelectric Sensors," *Int. J. Impact Engineering*, 34: 1258-1271.
6. Fukunaga, H. and N. Hu. 2006. "Experimental Impact Force Identification of Composite Structures, in *Proc. Third European Workshop on Structural Health Monitoring 2006*, A. Guemes ed., DES Tech Pub., pp. 840-847.
7. Vanderplaats, G. N. and H. Sugimoto. 1986. "A General Purpose Optimization Program for Engineering Design," *Computers Structures*, 24: 13-21.

# Identification of Impact Forces on Composite Structures Using an Inverse Approach

Ning Hu<sup>†a,b</sup>, Satoshi Matsumoto<sup>‡b</sup>, Ryu Nishi<sup>††b</sup> and Hisao Fukunaga<sup>†††b</sup>

*<sup>a</sup>Department of Engineering Mechanics, Chongqing University,  
Chongqing 400044, P.R. China*

*<sup>b</sup>Department of Aerospace Engineering, Tohoku University,  
Aramaki-Aza-Aoba 6-6-01, Aoba-ku, Sendai 980-8579, Japan*

<sup>†</sup> Associate Professor, Corresponding author: [hu@ssl.mech.tohoku.ac.jp](mailto:hu@ssl.mech.tohoku.ac.jp)

Tel.: 81-22-795-4109, Fax: 81-22-795-4109

<sup>‡</sup> Mr.: [matsumoto@ssl.mech.tohoku.ac.jp](mailto:matsumoto@ssl.mech.tohoku.ac.jp)

<sup>††</sup> Mr.: [nishi@ssl.mech.tohoku.ac.jp](mailto:nishi@ssl.mech.tohoku.ac.jp)

<sup>†††</sup> Professor: [fukunaga@ssl.mech.tohoku.ac.jp](mailto:fukunaga@ssl.mech.tohoku.ac.jp)

Running title: Identification of impact forces on composite structures

## **Abstract**

In this paper, an identification method of impact force is proposed for composite structures. In this method, the relation between force histories and strain responses is first formulated. The transfer matrix, which relates the strain responses of sensors and impact force information, is constructed from the finite element method (FEM). Based on this relation, an optimization model to minimize the difference between the measured strain responses and numerically evaluated strain responses is built up to obtain the impact force history. The identification of force history is performed by a modified least-squares method that imposes the penalty on the first-order derivative of the force history. Moreover, from the relation of strain responses and force history, an error vector indicating the force location is defined and used for the force location identification. The above theory has also been extended into the cases when using acceleration information instead of strain information. The validity of the present method has been verified through two experimental examples. The obtained results demonstrate that the present approach works very well, even when the internal damages in composites happen due to impact events. Moreover, this method can be used for the real-time health monitoring of composite structures.

**Keywords:** Impact force, identification, optimization model, PZT, accelerometer

## 1. Introduction

It is well-known that carbon fiber reinforced plastic (CFRP) composites possess high specific strength (strength-to-density ratio) and high specific stiffness, and are widely applied to the fields of aerospace, sports, automobiles, constructions, civil engineering, etc. Specifically, the lightness in weight of CFRP, which contributes the improvement of the ability of structures for saving fuel consumption, and its very small linear coefficient of thermal expansion make it a kind of widely used materials in structures of aerospace engineering. On the other hand, it is well recognized that this kind of materials is very susceptible to the transverse loads or transverse low-velocity impacts. It has been shown by many researchers, such as Geubelle and Baylor (1998), Duan and Ye (2002), Guinard *et al.* (2002) and Li *et al.* (2002), that low-velocity transverse impact could cause various damages, e.g. as shown in Figure 1, matrix cracks, delaminations and fiber breakages. Such damages can cause significant reductions in the strength and stiffness of the materials. Especially, the residual compressive strength of laminated CFRP materials with delaminations after the low-velocity impacts (CAI) has been paid much attention in the design of aircraft structures (Wang *et al.* 1995; Hu *et al.* 1999). It has been reported that there are a lot of possibilities to make these damages occur, for instance, the tool drop in the process of production and maintenance of aircrafts, and various collisions between aircraft body and passenger steps, small stones, and flying birds. Such damages are very difficult to be detected by naked eyes in many circumstances. Because under certain loading conditions, these damages may grow rapidly and lead to catastrophic failure of the structures before any precautionary measure can be taken, diagnosis of them is necessary by employing various techniques of damage inspection based on some traditional techniques, such as ultrasonic waves, X-rays, etc. Usually, these kinds of traditional damage inspection techniques cannot be used for the on-line monitoring of structural integrity. Moreover, they are expensive and time-consuming. Accordingly, a new inspection approach, i.e. structural health

monitoring, has been recently focused on by many researchers. In this inspection technique, both sensing network and damage inspection algorithm are incorporated into structures and computers, so that structural integrity can be automatically monitored using sensor information. It is known that some important information of external impact forces, e.g. maximum impact force, is tightly related to the damage patterns and damage extents (e.g., Li *et al.* 2002). To establish such a damage-monitoring system for various impact damages, the external impact forces should be first effectively evaluated.

In some previous studies for solving the impact force identification problem, the method using a transfer function that relates the impact forces to the corresponding responses has been proposed. For the cases with given force locations in advance, for example, Inoue *et al.* (1988) have experimentally obtained the transfer function between impact forces and strain responses, and determined the impact forces through the deconvolution method. Using the same relation obtained numerically, Doyle (1984) proposed a similar technique for identifying an impact force history in a time domain from the strain response of an isotropic beam. This technique was further extended to the identification of impact force in a frequency domain using FFT (Doyle 1987). In addition, the validity of this method was verified through experiments using strain gauges. Wu *et al.* (1994) have constructed Green's functions with the eigenmode expansion method to identify impact force histories by minimizing the residual error between measured strain responses and numerically evaluated ones.

On the other hand, for the impact events without given force locations, some effective methods to identify both locations and histories of impact forces have also been proposed. Yen and Wu (1995) have identified force locations with multiple strain responses on isotropic plates. Impact force histories were identified using the approach by Wu *et al.* (1994). Choi and Chang (1996) have minimized the error between measured strain responses in PZT sensors and numerically evaluated ones to identify impact force locations and histories, simultaneously. Shin (2000) studied the impact

force identification technique using the information of modal displacements.

Moreover, some researchers employed the Neural Network to identify impact forces. For instance, Shaw *et al.* (1995) proposed the identification technique of force location and magnitude using the strain measurement of an isotropic plate and Neural Network. Akhavan *et al.* (2000) used the optic fiber and Neural Network to identify the impact forces. For all currently existing methods, it should be noted that so far, no results have been reported for their effectiveness when the practical impact damages happen in structures.

In this paper, a technique to identify the location and history of impact force acting on CFRP laminated plates is proposed. First, the relation between force histories and strain responses in CFRP laminated plates is formulated by using FEM. Next, a reliable identification method of force history and force location is built up. This approach can also be used when acceleration responses are available. Finally, the proposed technique has been realized using an identification system consisting of a measurement part and several signal conditioners. The obtained results show that it is possible to use the present method for the on-line or real-time health monitoring of composite structures, even when impact-induced internal damages in composites occur.

## 2. Theory

### 2.1. Strain Response Induced by Impact Force

In the low-velocity impact event, a CFRP plate excited by a force in the out-of-plane direction is considered. The governing equation of forced vibration of the plate is described as follows:

$$\mathbf{M}\ddot{\mathbf{u}}(t) + \mathbf{C}\dot{\mathbf{u}}(t) + \mathbf{K}\mathbf{u}(t) = \tilde{\mathbf{f}}(t) \quad (1)$$

where  $\mathbf{M}$ ,  $\mathbf{C}$  and  $\mathbf{K}$  are the mass matrix, the damping matrix and the stiffness matrix, respectively,  $\mathbf{u}(t)$  is the nodal displacement vector,  $(\dot{\phantom{x}})$  denotes a derivative with respect

to time  $t$  and  $\tilde{\mathbf{f}}(t)$  describes the impact force location and history.

First, in this research, the 4-noded non-conforming bending element based on Kirchhoff plate theory is employed in the FEM model of laminated plates. After performing the natural vibration analysis of Eq. (1), the following mode expansion of displacements can be employed

$$\mathbf{u} = \sum_{i=1}^n \boldsymbol{\phi}_i \xi_i = \boldsymbol{\Phi} \boldsymbol{\xi} \quad (2)$$

where  $\boldsymbol{\phi}_i$  is the  $i$ th-order vibration mode, and  $\xi_i$  is the  $i$ th-order modal displacement.

Then Eq. (1) can be transformed into the modal coordinates as follows

$$\ddot{\xi}_i(t) + 2\zeta_i \omega_i \dot{\xi}_i(t) + \omega_i^2 \xi_i(t) = \boldsymbol{\phi}_i^T \tilde{\mathbf{f}}(t) \quad (3)$$

where  $\omega_i$  is the  $i$ th-order natural circular frequency. And the damping term  $\zeta_i$  can be expressed as follows

$$\zeta_i = \frac{1}{2} \left( \frac{\alpha_c}{\omega_i} + \beta_c \omega_i \right) \quad (4)$$

when the damping matrix  $\mathbf{C}$  in Eq. (1) is cast into the following form

$$\mathbf{C} = \alpha_c \mathbf{M} + \beta_c \mathbf{K} \quad (5)$$

where  $\alpha_c$  and  $\beta_c$  are the damping coefficients.

Eq. (3) can be solved by means of Duhamel's integral easily, and then we can obtain the displacement  $\mathbf{u}$  by using Eq. (2). Finally, the relation between the impact force history and the strain response measured at the  $i$ th sensor can be expressed in the following algebraic equation:

$$\tilde{\boldsymbol{\varepsilon}}_i = \mathbf{G}_i \tilde{\mathbf{f}} \quad (6)$$

where the strain and force histories can be expressed at discrete time points as

$$\tilde{\boldsymbol{\varepsilon}}_i = [\varepsilon_i(0) \quad \varepsilon_i(\Delta t) \quad \cdots \quad \varepsilon_i(k\Delta t)]^T \quad \text{and} \quad \tilde{\mathbf{f}} = [f(0) \quad f(\Delta t) \quad \cdots \quad f(k\Delta t)]^T \quad (7)$$

where  $(k+1)$  is the number of sampling points in the time domain.



In Eq. (6),  $\mathbf{G}_i$  is a transfer matrix consisting of the Green's function at each time point, which is a lower triangular matrix (Wu *et al.* 1994, Fukunaga and Hu 2004). This matrix is determined by the force location and the observation point of strain only, and is not influenced by the force history.

## 2.2. Force history identification

The identification of impact force history is discussed in this section. First, an identification technique of force history is built up by solving an inverse problem. When the strain responses are acquired by using the multi-point measurements of sensors, the force history can be obtained by employing the least-squares method in the case of that the force location is known.

When using the FEM to construct the  $\mathbf{G}_i$  matrix, however, the direct solution of the identified force history from the traditional least-squares method contains some very large oscillations due to the influence of the FEM modeling errors, measurement noises, etc. Consequently, a technique imposing the penalty on the derivative of the force history is proposed to improve the numerical stability. By applying this technique, the force history can be identified using a minimization problem as:

$$\begin{aligned} \min_{\{\tilde{\mathbf{f}}\}} F &= \sum_{i=1}^m \left\| \boldsymbol{\varepsilon}_i^* - \mathbf{G}_i \tilde{\mathbf{f}} \right\|^2 + \alpha \left\| \Delta \tilde{\mathbf{f}} \right\|^2 \\ \text{subject to } \tilde{\mathbf{f}} &\geq \mathbf{0} \end{aligned} \quad (8)$$

where  $\boldsymbol{\varepsilon}_i^*$  is the experimental strain data,  $m$  is the number of sensors,  $\alpha$  is the regularization parameter for the derivative of the force history, and  $\{\Delta \tilde{\mathbf{f}}\} = \mathbf{L} \tilde{\mathbf{f}}$ , where  $\mathbf{L}$  is a finite difference operator for the first-order derivative of the force history.

It is very important to select a proper regularization parameter  $\alpha$ . When the regularization parameter is too small, the identified force history has some very large oscillations. On the contrary, when the regularization parameter is too large, the force history is identified excessively smoothly, and the identified maximum impact force is

usually lower than the true one. In this paper, the optimal regularization parameter is determined as a solution of the following maximization problem:

$$\begin{aligned} J &= \max_{\alpha} \lambda_{\min}(\mathbf{A}(\alpha)) \\ \text{subject to } &\lambda_{\max}(\mathbf{A}(\alpha)) \leq a\lambda_{\max}(\mathbf{A}(0)) \end{aligned} \quad (9)$$

where

$$\mathbf{A} = \sum_{i=1}^m \mathbf{G}_i^T \mathbf{G}_i + \alpha \mathbf{L}^T \mathbf{L} \quad (10)$$

In Eq. (9),  $\lambda_{\min}(\mathbf{A}(\alpha))$ ,  $\lambda_{\max}(\mathbf{A}(\alpha))$ , and  $\lambda_{\max}(\mathbf{A}(0))$  denote, respectively, the minimum and maximum eigenvalues of the matrix  $\mathbf{A}$  for an arbitrary  $\alpha$  and the maximum eigenvalue of  $\mathbf{A}$  for  $\alpha=0$ . In Eq. (9), the small value of  $a=1.01$  is employed here to avoid the excessive change of the maximum eigenvalue of  $\mathbf{A}(\alpha)$ . A solution of Eq. (9) yields the optimal  $\alpha$ . It can prevent the numerical instability due to the maximization of the minimum eigenvalue of  $\mathbf{A}(\alpha)$ , meanwhile it can avoid excessive smoothing and the extremely lower maximum impact force due to the strict constraint on the change of the maximum eigenvalue of  $\mathbf{A}(\alpha)$ .

Finally, the force history identification is achieved by solving Eq. (8) by means of the quadratic programming method in this study.

### 2.3. Force location identification

In this work, another issue is the determination of the force location. In the force history identification with the assumed location, we can obtain a force history denoted by  $\tilde{\mathbf{f}}$ . Then an error vector, which indicates the deviation between the calculated strains and measured strains, can be defined. The force location is determined by solving the following minimization problem:

$$\min_{x,y} E = \sqrt{\sum_{i=1}^m \|\boldsymbol{\varepsilon}_i^* - \mathbf{G}_i \tilde{\mathbf{f}}\|^2} \quad (11)$$

Eq. (11) is solved by a nonlinear programming method, e.g., DFP method (Vanderplaats and Sugimoto 1986). In the minimization process, the force history  $\tilde{f}$  is updated using Eq. (8) for each force location. By repeating the above process of solution of Eqs (8) and (11), we can simultaneously determine the force location and force history.

In the above sections, we have described the relations when using the strain information obtained from strain sensors. It is also very easy to build up the similar relations using the acceleration information at some points on plates obtained from the accelerometers, and the corresponding theory is abbreviated here for simplicity. In this research, both PZT strain sensors and accelerometers are employed as sensors in our experiments.

### 3. IDENTIFICATION RESULTS

#### 3.1 Verification for CFRP laminates using impulse hammer

To verify the formulations stated in the previous sections, the impact test for CFRP rectangular laminated plates has been performed. The experimental system for verifying the present method is shown in Figure 2. The identification system consists of a four-corner clamped CFRP plate specimen, a jig, a charge amplifier, a digital oscilloscope, an impulse hammer and a personal computer. Two kinds of CFRP plates are considered in the present research as shown in Table 1. Four specimens were prepared as shown in Table 1 with two kinds of sensors. First, a strain sensor network called SMART Layer (Acellent Technology, Inc.) (Wang and Chang 1999), in which 4 PZT sensors are placed, was utilized to measure strain responses. The schematic illustration of the shape of specimen and sensor positions is in Figure 3. This SMART layer was embedded within the laminate and near the bottom surface of the plate with the distance of 0.3 mm as shown in Figure 3. CFRP1 and CFRP3 shown in Table 1 employ this kind of sensors. Also, four accelerometers were used as sensors in this work for CFRP2 and CFRP4 shown in Table 1, which were attached on the top surface of plates. For both

kinds of sensors, the sensor locations are shown in Table 2 in the plate plane as shown in Figure 3. In this test, the impact is applied using an impulse hammer (ONO SOKKI, GK-3100). Multiple sensor responses due to the applied impact are amplified through a charge amplifier (ONO SOKKI, CH-1100), and A/D conversion is conducted through a digital oscilloscope (YOKOGAWA, DL708E). Finally, strain or acceleration responses are inputted into a personal computer. The force history is also directly measured from the output of impulse hammer for comparison to the identified force result. When the impact force is applied and the strain or acceleration responses are induced, a trigger signal is sent to the computer from the oscilloscope. After receiving the trigger signal, the computer imports into the strain or acceleration responses from the oscilloscope, identifies the impact force, and then monitors the possible strain or acceleration responses caused by other impact events again. In this test, the measurement time and the sampling time are  $1.0 \times 10^{-2}$  second and  $1.0 \times 10^{-4}$  second, respectively. In order to determine the sensitivity of the PZT sensors, the calibration was performed by comparing the output voltage of the PZT sensor to the output of the biaxial strain gauge located at the same position on the opposite surface of the plate.

First, by employing the numerical simulations for a cantilever plate (CFRP1), we examined the effect of the regularization parameter  $\alpha$  in Eq. (5) on the identification results of the force history. To simulate the experimental data, the numerically obtained strain data are mixed with some random noises of 2% of the highest amplitude of response of each sensor. When the force location is specified, the optimal regularization parameter  $\alpha$  is determined using Eq. (9). Figure 4 shows the identified force histories for the optimal value of  $\alpha$  and for the value of  $\alpha = 0$ , which are compared to the true force history. It is shown that the identified force history has some very large oscillations when the regularization parameter is equal to zero. For the optimal regularization parameter, the identified force history agrees very well with the true one.

When using the practical experimental data, Figures 5(a) and 5(b) show the

identification results of the force location for CFRP1 and CFRP3, respectively. The average errors of the identified force locations are 10.2 mm for CFRP1 and 8.5 mm for CFRP3, respectively. The location error is large near the clamped corners or near the free edge of the plate while the error is small in the area existing apart from the boundaries of the plate. The main reason of the location error may be due to the error of FEM modeling. Figures 6(a) and 6(b) show the identified force histories at the point A for CFRP1 and the point B for CFRP3 in Figures 5(a) and 5(b), respectively. In these cases, the force locations are identified near the true ones. Therefore, the identified force histories agree very well with the experimental ones. When the identified force location is not so accurate, the accuracy of identified impact force history will usually decrease. However, in some cases, although the identification accuracy of force location is not so high, we can also get very accurate results for impact force history, such as the points C and D in Figure 5(b). Therefore, it can be concluded that the present identification system is very successful for identification of force history and location except at some specified structure boundaries.

Figures 7(a) and 7(b) show identification results of the force location for CFRP2 and CFRP4, respectively. The average errors of the force location are 3.8 mm for CFRP2 and 4.2 mm for CFRP4, respectively. Compared to Figures 5(a) and 5(b), it can be found that the identification accuracy for force location increases remarkably when using accelerometers as sensors. The main reason is that the numerical accuracy of strain data is usually lower than that of acceleration data. Generally, the accuracy of the first-order derivatives of translation displacements for obtaining the strain responses in the FEM model is low. Figures 8(a) and 8(b) show the identified force histories at the point A for CFRP2 and the point B for CFRP4 in Figures 7(a) and 7(b), respectively. In these cases, the impact forces can be identified accurately. Although there is an obvious advantage in the accuracy of accelerometers, the strain sensors are practically employed in more situations due to its small sizes and installation convenience.

For the present method, most of the identification time is required in the search process of force location identification. The force history identification is very fast at a specified force location. To speed up the identification process, in our identification system, the strain responses from four sensors are compared first. When the observable strain signal of a sensor among four sensors arrives first, the force location search is then limited to an area surrounding that sensor (around 1/4 size of the plate). Other portions of the plate will not be searched in our algorithm. In this case, the present force identification system is very fast, which takes only a few seconds to identify the location and the history for each impact event.

### *3.2 Verification for quasi-isotropic CFRP laminates using drop-weight tests*

Another example is a drop-weight test using Dynatup 9250HD test machine made by Instron Inc. The supporting jig and specimen were prepared according to SACMA standards of CAI test as shown in Figure 9. The rectangular quasi-isotropic CFRP specimen was put on a supporting frame with 4-point fixed on the surface of the specimen. An impactor with the mass of 4.6 kg drops at the center of the specimen. An accelerometer was installed on the impactor to measure the impact force. The dimensions of the quasi-isotropic CFRP of 32 plies  $[(45^\circ/0^\circ/-45^\circ/90^\circ)_4]_S$  are shown in Figure 10 with the material properties defined in Table 3. 4 impact energy levels were investigated as shown in Table 4. For each energy level, two tests for two specimens were performed. The presence of damages in specimens after impact was checked by ultrasonic inspections. From Table 4, we can find that for the case of 3.0 J, there is completely no damage for two tested specimens. However, for 4.8 J, there are damages in one specimen, meanwhile there is completely no damage in another specimen. When the impact energy is higher than 4.8 J, the impact-induced damages always happen. The force histories in two tests are very similar and repeatable except for the case of 4.8 J. The ultrasonic inspection results of damages of 6.0 J from the top, bottom and thickness

direction are shown in Figure 11. In this example, to construct the  $G_i$  matrix, the FEM model with 384 elements is shown in Figure 12, in which the four points on the plate surface and the inner edge of the supporting frame are modeled by fixed boundary conditions. Four bi-axial strain gages were attached on the upper surface of plate, with the locations of (31 mm, 46 mm) for Sensor 1, (71 mm, 46 mm) for Sensor 2, (31 mm, 106 mm) for Sensor 3 and (71 mm, 106 mm) for Sensor 4. In the  $G_i$  matrix constructed from the FEM model, no damages are considered. This matrix of the intact plate may cause errors for the cases of high impact energies, such as 6.0 J and 7.2 J, which induce obvious damages. In this research, only impact force history is identified since the impact location is fixed at the center of plate when performing the experiments.

First, for the cases without happening of damages, the results are shown in Figure 13. From it, we can find that for cases 1 and 2 (3.0 J) and case 3 (4.8 J) in Table 4, the present approach can identify the impact force very accurately. It means that for the cases without damages, the constructed  $G_i$  matrix is quite accurate. Second, for the cases with damages, the results are plotted in Figure 14. In this case, the impact force history becomes more complex. Figure 14(a) shows that for case 4 (4.8 J) with damages, the present approach can identify the impact force very well. However, at the stage after the peak load, the present approach cannot precisely trace the oscillating curve of experimental one. It seems that after the peak load, the present technique yields the smooth average impact force. In Figure 14(b), the results for 7.2 J are shown. From it, we can find that the present approach works well. However, compared to Figure 14(a), the identified result becomes slightly worse due to higher damage extent in this case. The duration of identified impact force is slightly shorter than that of experimental one since the FEM model without consideration of damages may evaluates the higher structural stiffness. This FEM model yields inaccurate  $G_i$  matrix at the stage after the occurring of internal impact damages. Although there are some errors in the numerical model for the damaged cases, Figure 14 illustrates that the present approach is still

effective for obtaining acceptable impact force history.

#### **4. CONCLUSIONS**

In this research, an identification method of impact force acting on composite structures is proposed. First, the transfer matrix, which connects the measured responses of sensors and impact force information, is constructed from the FEM model. Second, the corresponding optimization model to minimize the difference between the measured responses and numerically evaluated responses is built up to obtain the stable impact force history. Moreover, an error vector indicating the force location is defined for searching for the force location. Two experimental examples have been employed to illustrate the validity of the present method. From the results, it can be found that the proposed method can identify the impact force history and location accurately within a few seconds. Therefore, the proposed inverse method can be used for the real-time health monitoring of composite structures. When using accelerometers as sensors, the identification accuracy is higher than that of PZT strain sensors. The errors of identified force location are higher near structure boundaries due to the numerical modeling errors and experimental noises. When the internal damages induced by impact events happen, the accuracy of identified force history is still within the acceptable range. The main problem in the present approach is that the transfer matrix is constructed by the numerical model, which certainly leads to the lower modeling and identification accuracies (e.g., the force location) for complex and large-scale structures. In the ongoing research, this problem will be addressed through constructing a highly reliable transfer matrix experimentally.

#### **Acknowledgements**

This work is partly supported by the Award from AFOSR numbered by AOARD-06-4066 and Natural Science Foundation Project of CQ CSTC.



## References

1. Akhavan, F. and Watkins, S.E. *et al.* (2000), "Prediction of impact contact forces of composite plates using fiber optic sensors and neural networks", *Mechanics of Composite Materials and Structures*, **7**, 195-205.
2. Choi, K. and Chang, F.K. (1996), "Identification of impact force and location using distributed sensors", *AIAA Journal*, **34**, 136-142.
3. Doyle, J.F. (1984), "An experimental method for determining the dynamic contact law", *Experimental Mechanics*, **24**, 10-16.
4. Doyle, J.F. (1987), "Experimentally determining the contact force during the transverse impact of an orthotropic plate", *Journal of Sound and Vibration*, **118**, 441-448.
5. Duan, S.H. and Ye, T.Q. (2002), "Three-dimensional frictional dynamic contact analysis for predicting low-velocity impact damage in composite laminates", *Advances in Engineering Software*, **33**, 9-15.
6. Fukunaga, H. and Hu, N. (2004), "Health monitoring of composite structures based on impact force identification", *Proceeding of the Second European Workshop, Structural Health Monitoring*, Edited by C. Boller and W.J. Straszewski, 415-422.
7. Geubelle, P.H. and Baylor, J.S. (1998), "Impact-induced delamination of composites: a 2D simulation", *Composites: Part B*, **29B**, 589-602.
8. Guinard, S. and Allix, O. *et al.* (2002), "A 3D damage analysis of low-velocity impacts on laminated composites", *Composites Science and Technology*, **62**, 585-589.
9. Hu, N. and Fukunaga, H. *et al.* (1999), "Compressive buckling of laminates with an embedded delamination", *Composites Science and Technology*, **59**, 1247-1260.
10. Inoue, H. and Watanabe, R. *et al.* (1988), "Measurement of impact force by the deconvolution method (part-a)", *Journal of Japanese Society for Non-Destructive Inspection*, **34**, pp. 337-342.

11. Inoue, H. and Watanabe, R. *et al.* (1988), “Measurement of impact force applied to a plate by the deconvolution method (part-b)”, *Journal of Japanese Society for Non-Destructive Inspection*, **37**, 874-878.
12. Li, C.F. and Hu, N. *et al.* (2002), “Low-velocity impact-induced damage of continuous fiber-reinforced composite laminates. Part I. An FEM numerical model”, *Composites: Part A*, **33**, 1055-1061.
13. Li, C.F. and Hu, N. *et al.* (2002), “Low-velocity impact-induced damage of continuous fiber-reinforced composite laminates. Part II. Verification and numerical investigation”, *Composites: Part A*, **33**, 1063-1072.
14. Shaw, J.K. and Sirkis, J.S. *et al.* (1995), “Model of transverse plate impact dynamics for design of impact detection methodologies”, *AIAA Journal*, **33**, 1327-1335.
15. Shin, E.S. (2000), “Real-time recovery of impact force based on finite element analysis”, *Composite Structure*, **76**, 621-627.
16. Vanderplaats, G.N. and Sugimoto, H. (1986), “A general purpose optimization program for engineering design”, *Computers Structures*, **24**, 13-21.
17. Wang, C.S. and Chang, F.K. (1999), “Built-in diagnostics for impact damage identification of composite structures”, *Structural Health Monitoring 2000, Stanford, 1999*, Edited by F.K. Chang (Stanford University, 1999), 612-621.
18. Wang, J.T.S. and Cheng, S.H. *et al.* (1995), “Local buckling of delaminated beams and plates using continuous analysis”, *Journal of Composite Materials*, **29**, 1374-1402.
19. Wu, E. and Yeh, J.C. *et al.* (1994), “Identification of impact forces at multiple locations on laminated plates”, *AIAA Journal*, **32**, 2433-2439.
20. Yen, C.S. and Wu, E. (1995), “On inverse problem of rectangular plates subjected to elastic impact, Part I: method development and numerical verification”, *Journal of Applied Mechanics*, **62**, 692-698.
21. Yen, C.S. and Wu, E. (1995), “On inverse problem of rectangular plates subjected to

elastic impact, Part II: experimental verification and further application”, *Journal of Applied Mechanics*, **62**, 699-705.

## Figure and Table Captions

Figure 1. Various damages due to transverse impacts

Figure 2. Experimental system

Figure 3. CFRP specimen and smart layer

Figure 4. Relation between regularization parameter and force history

Figure 5. Identification results of force location using piezoelectrics

Figure 5(a) CFRP1, Figure 5(b) CFRP3

Figure 6. Results of impact forces using piezoelectrics

Figure 6(a) CFRP1 (point A in Figure 5(a)), Figure 6(b) CFRP3 (point B in Figure 5(b))

Figure 7. Identification results of force location using accelerometer

Figure 7(a) CFRP2, Figure 7(b) CFRP4

Figure 8. Results of impact forces using accelerometer

Figure 8(a) CFRP2 (point A in Figure 7(a)), Figure 8(b) CFRP4 (point B in Figure 7(b))

Figure 9. Drop-weight test setup

Figure 10. Quasi-isotropic CFRP specimen

Figure 11. Results of ultrasonic inspection for 6.0 J

Figure 11(a) Impacted side, Figure 11(b) Opposite side of impacted side

Figure 12. FEM mesh for identification of impact force

Figure 13. Identified impact forces for cases without damages

Figure 13(a) Results of impact energy of 3.0 J (without damages), Figure 13(b) Results of impact energy of 4.8 J (without damages)

Figure 14. Identified impact forces for cases with damages

Figure 14(a) Results of impact energy of 4.8 J (with damages), Figure 14(b) Results of impact energy of 7.2 J (with damages)

Table 1. Properties of the specimens

Table 2. Sensor positions

Table 3. Material properties of CFRP specimen

Table 4. Impact test results

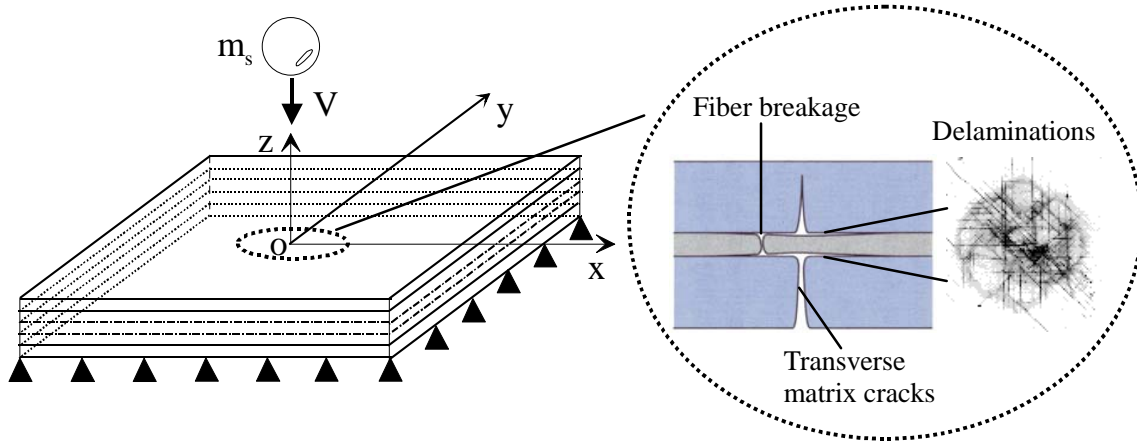


Figure 1. Various damages due to transverse impacts

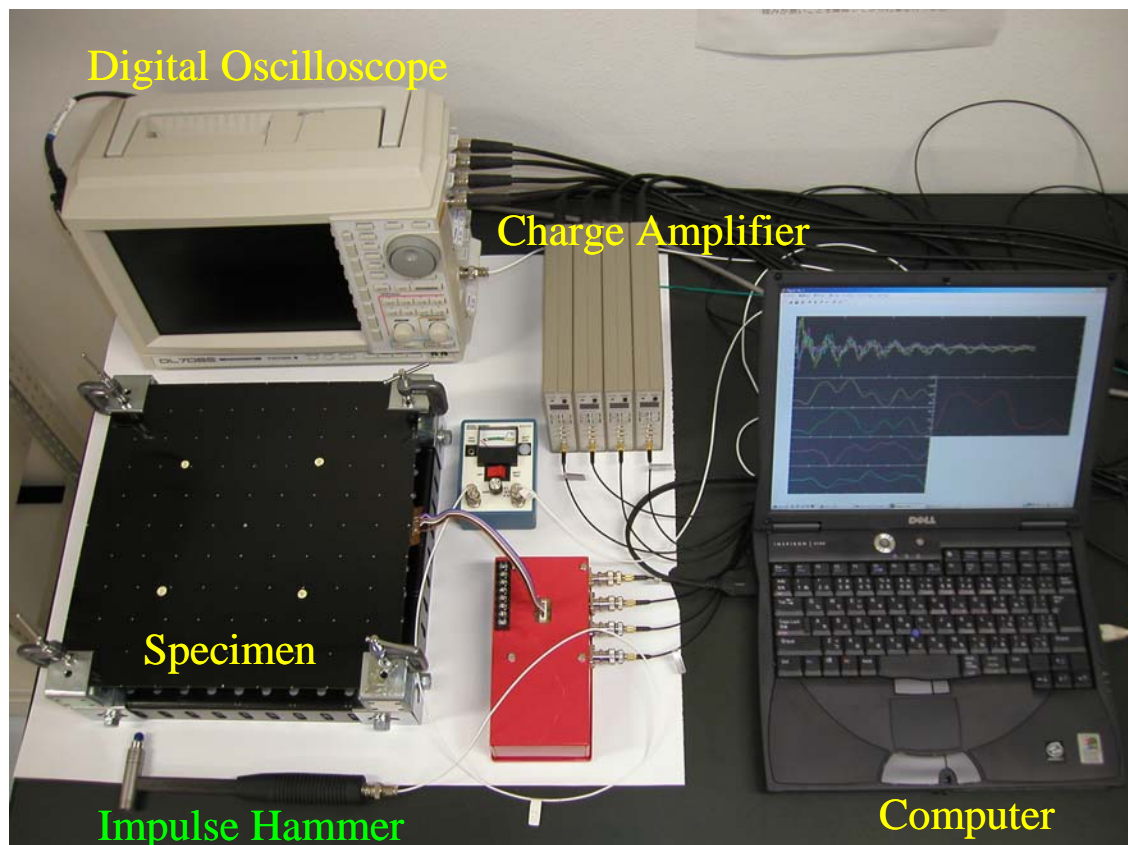


Figure 2. Experimental system

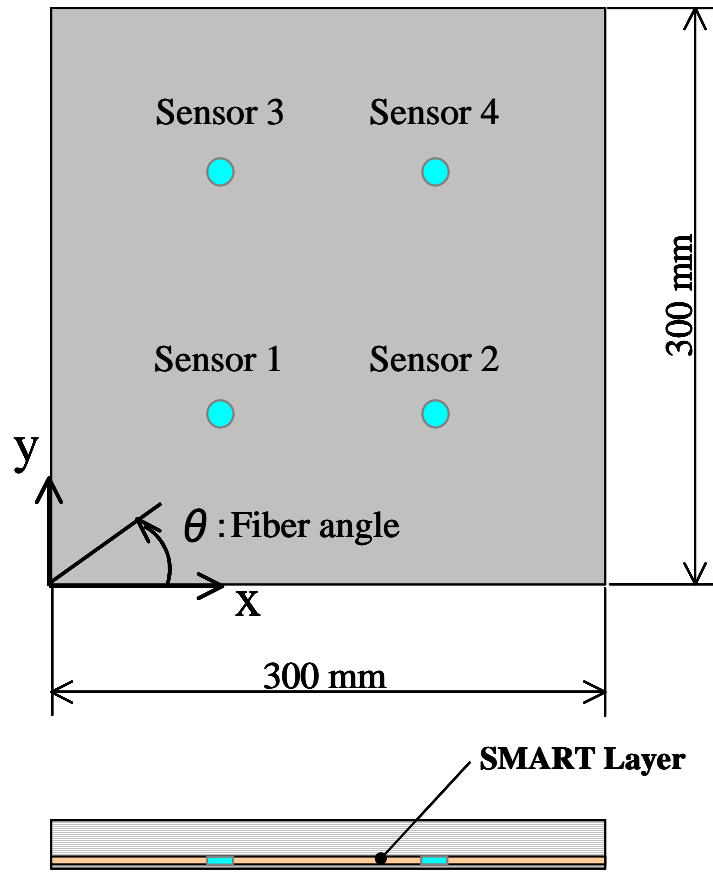


Figure 3. CFRP specimen and smart layer

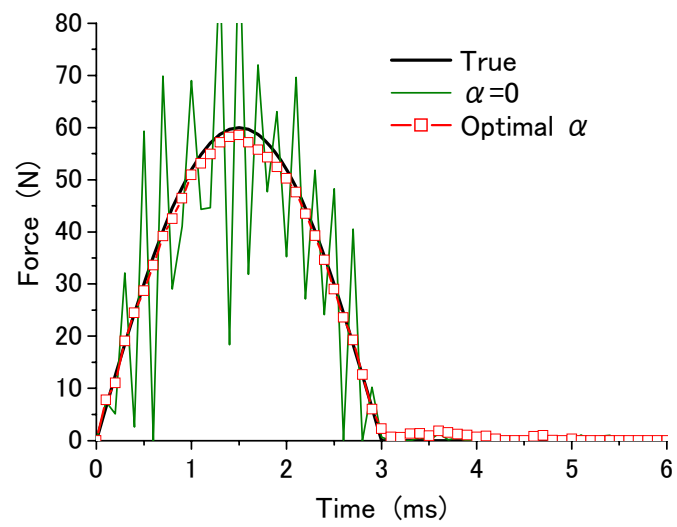


Figure 4. Relation between regularization parameter and force history

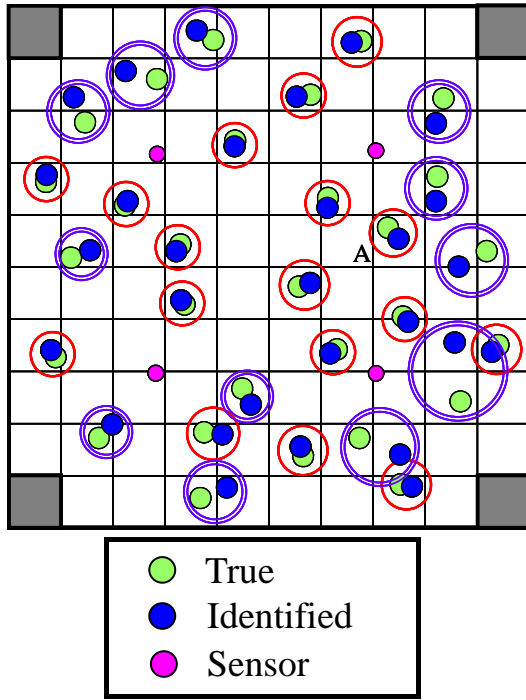


Figure 5(a) CFRP1

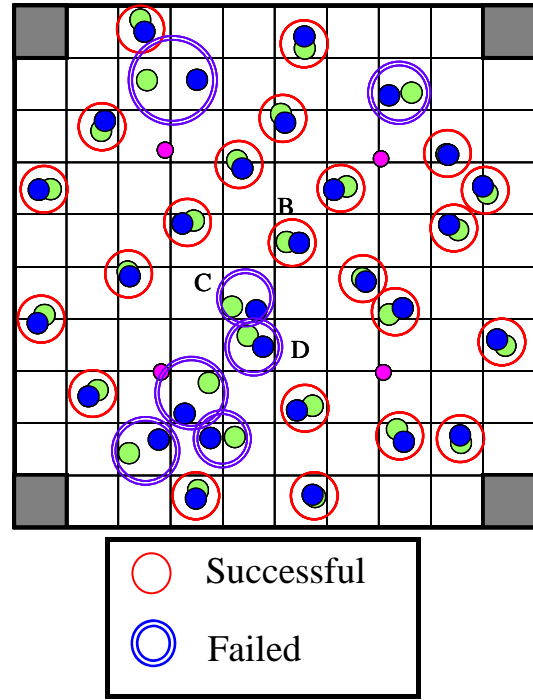


Figure 5(b) CFRP3

Figure 5. Identification results of force location using piezoelectrics

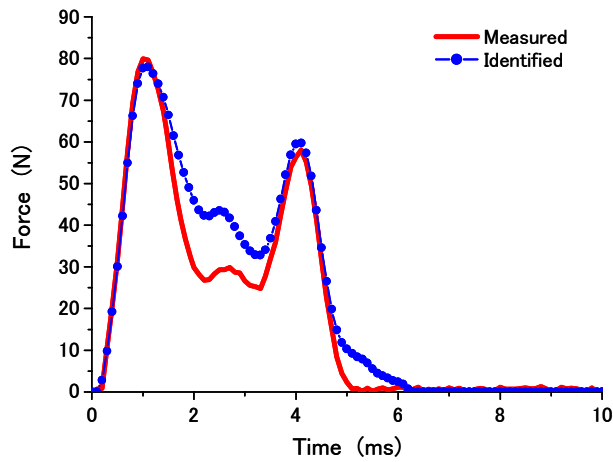


Figure 6(a) CFRP1 (point A in Figure 5(a))

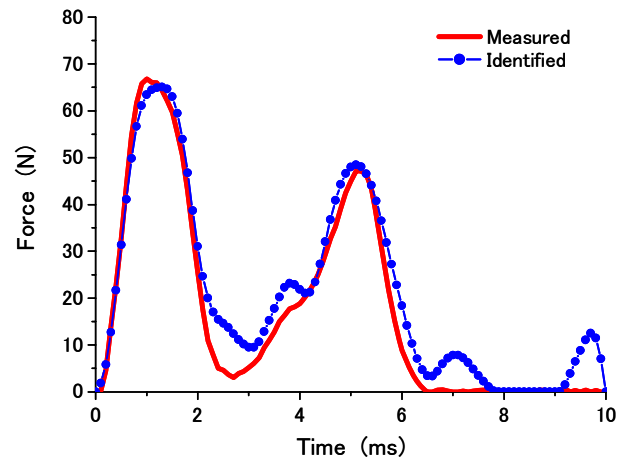


Figure 6(b) CFRP3 (point B in Figure 5(b))

Figure 6. Results of impact forces using piezoelectrics

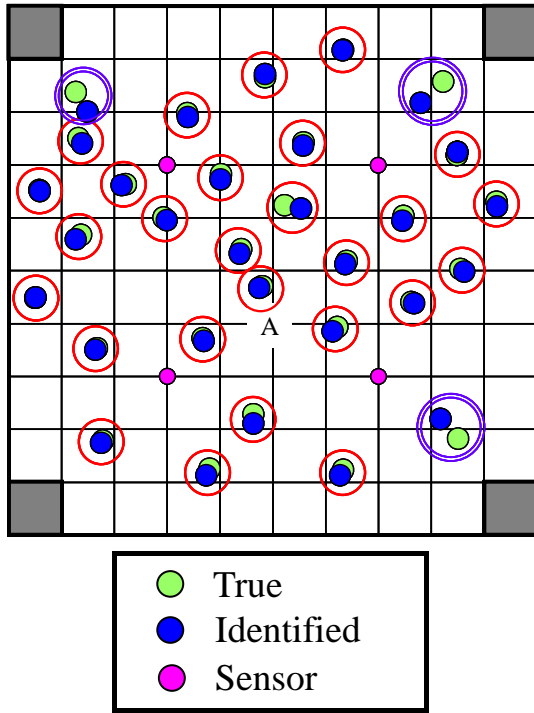


Figure 7(a) CFRP2

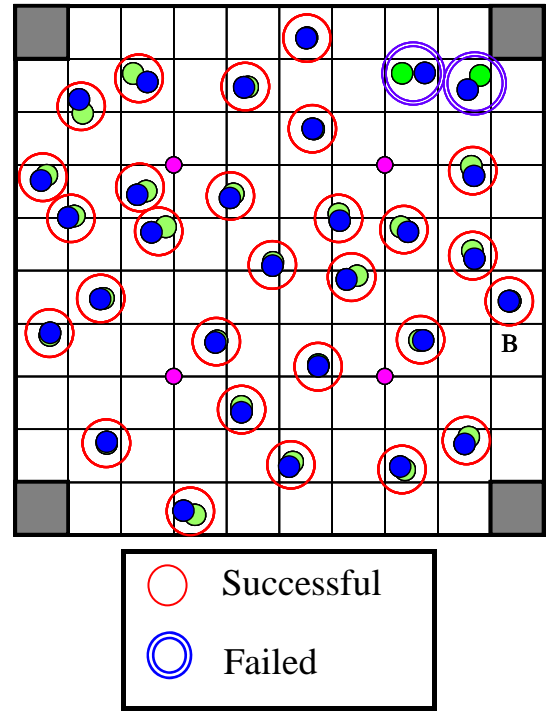


Figure 7(b) CFRP4

Figure 7. Identification results of force location using accelerometers

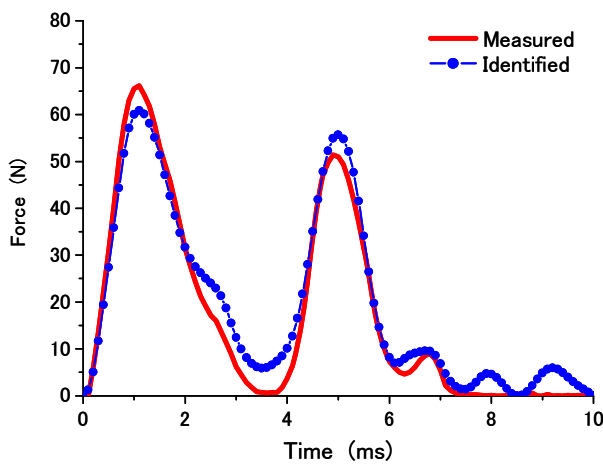


Figure 8(a) CFRP2 (point A in Figure 7(a))

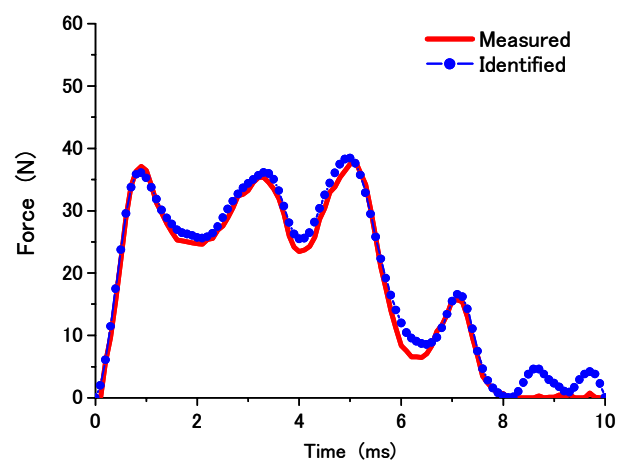


Figure 8(b) CFRP4 (point B in Figure 7(b))

Figure 8. Results of impact forces using accelerometers



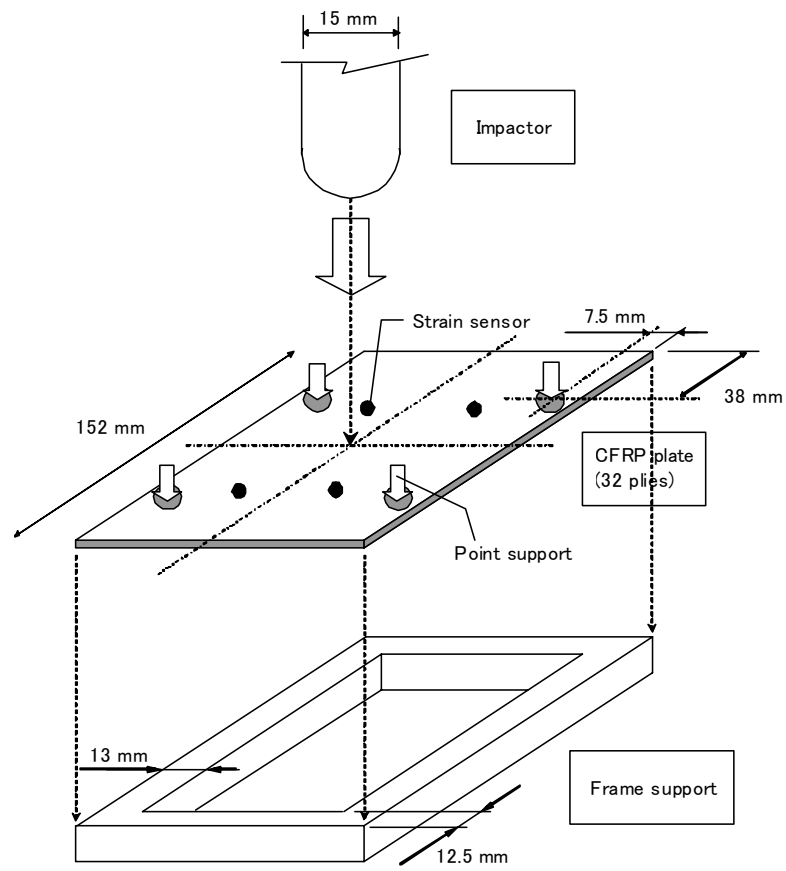


Figure 9. Drop-weight test setup

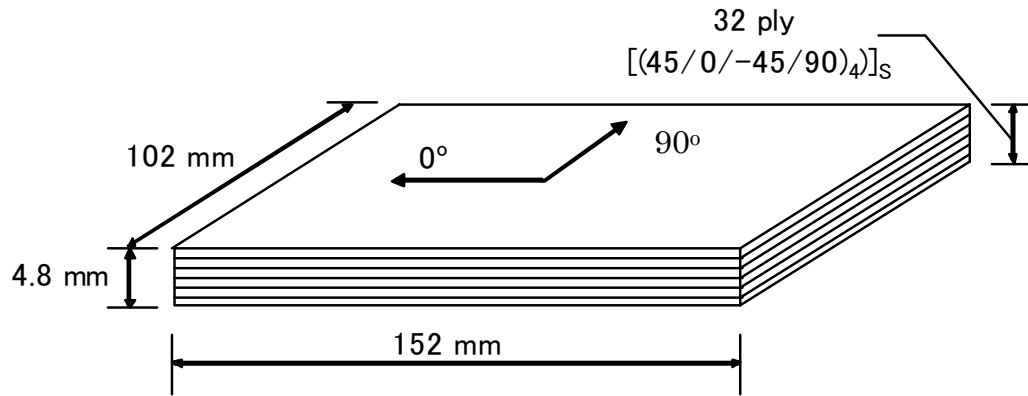


Figure 10. Quasi-isotropic CFRP specimen

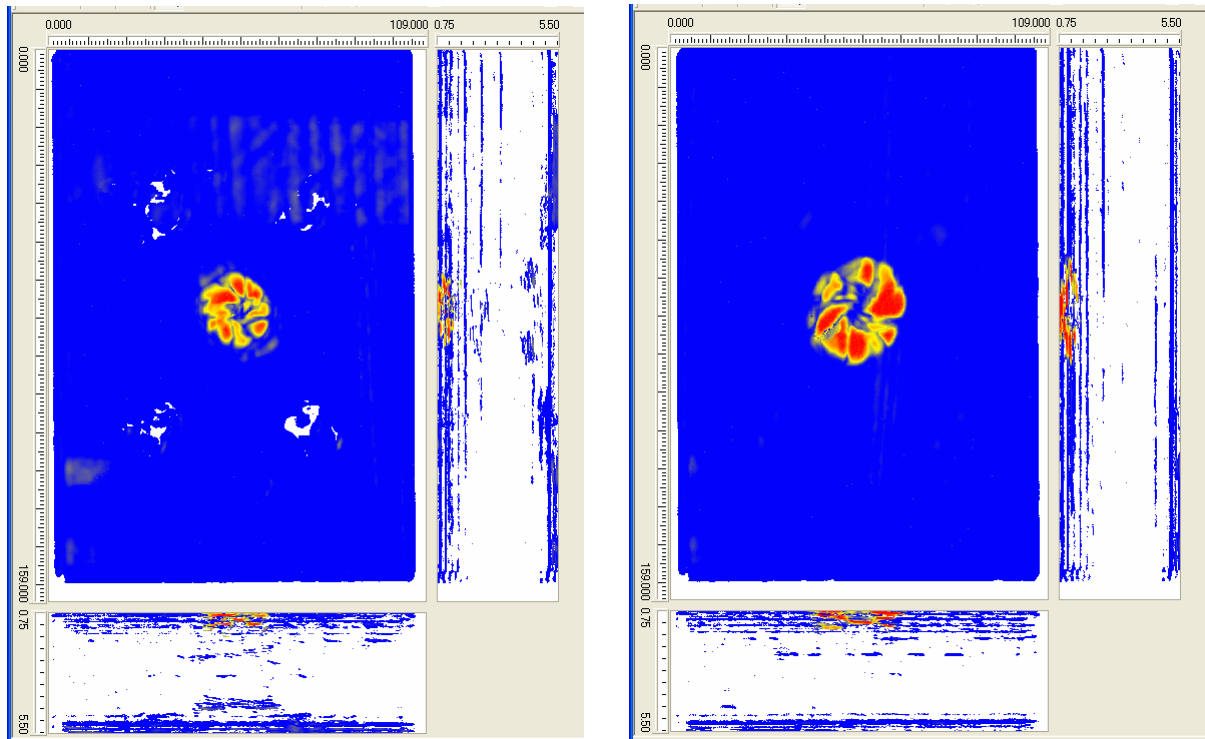


Figure 11(a) Impacted side

Figure 11(b) Opposite side of impacted side

Figure 11. Results of ultrasonic inspection for 6.0 J

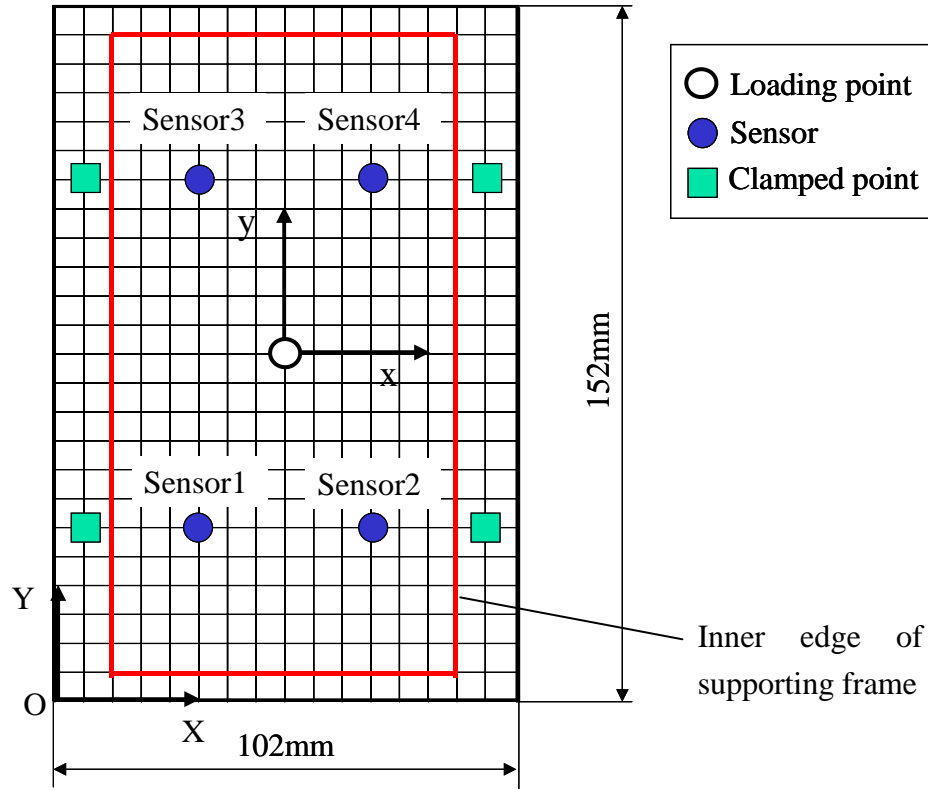


Figure 12. FEM mesh for identification of impact force

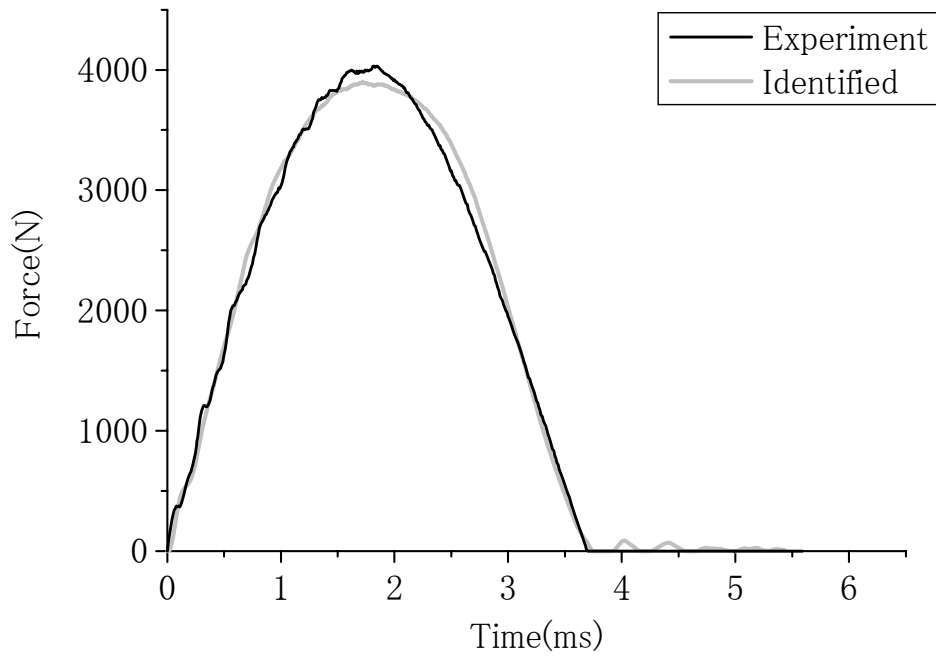


Figure 13(a) Results of impact energy of 3.0 J (without damages)

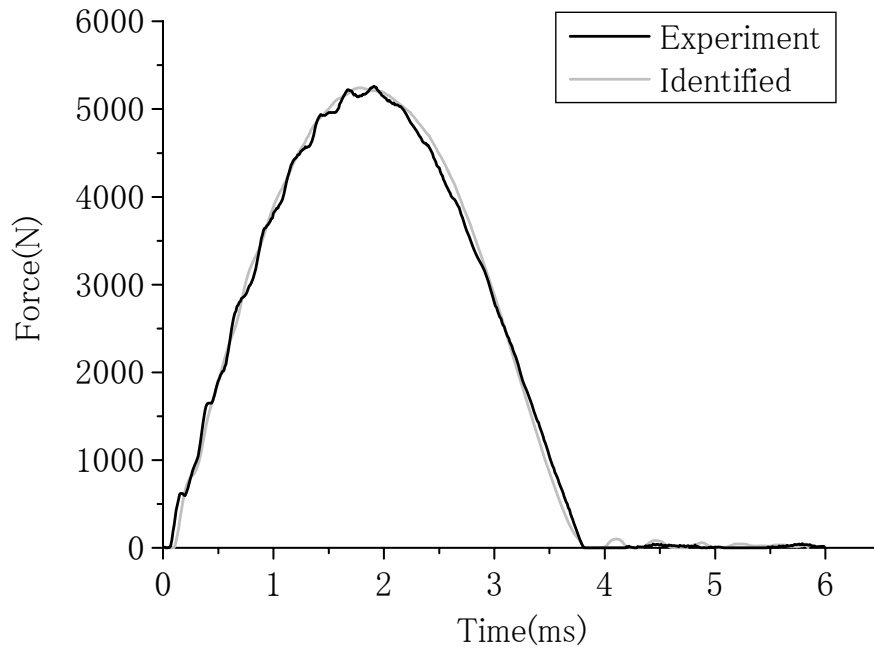


Figure 13(b) Results of impact energy of 4.8 J (without damages)

Figure 13. Identified impact forces for cases without damages

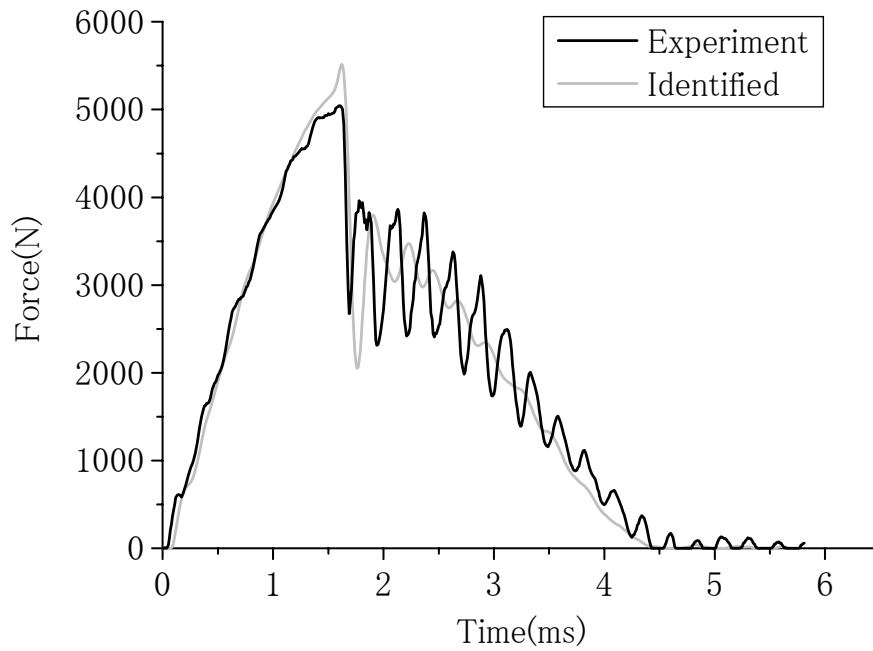


Figure 14(a) Results of impact energy of 4.8 J (with damages)

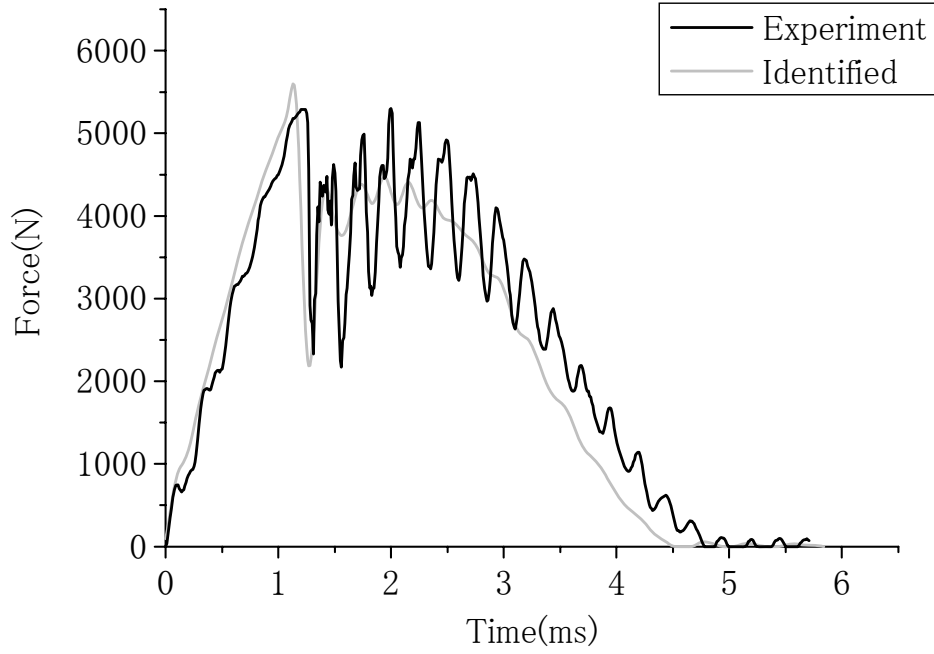


Figure 14(b) Results of impact energy of 7.2 J (with damages)

Figure 14. Identified impact forces for cases with damages

Table 1. Material properties of specimens

	CFRP1	CFRP2	CFRP3	CFRP4
Sensor	PZT	Accelerometer	PZT	Accelerometer
Laminate Sequence	$[45_2 / -45_4 / 45_2]_s$		$[0_2 / 45_2 / -45_2 / 90_2]_s$	
Geometry [mm]	Length = 300 Width = 300 Thickness = 2.27	Length = 300 Width = 300 Thickness = 2.3	Length = 300 Width = 300 Thickness = 2.3	Length = 300 Width = 300 Thickness = 2.28
$E_1$ [Gpa]	114.2	104.2	117.6	113.2
$E_2$ [Gpa]	10.8	10.8	9.2	9.2
$G_{12}$ [Gpa]	5.49	5.49	4.5	4.5
$\nu_{12}$	0.3	0.3	0.3	0.3
$\rho$ [kg/m <sup>3</sup> ]	1550	1550	1550	1550

Table 2. Sensor positions

Sensor	PZT	Accelerometer
Sensor1	(85 mm, 90 mm)	(90 mm, 90 mm)
Sensor2	(213 mm, 90 mm)	(210 mm, 90 mm)
Sensor3	(86 mm, 216 mm)	(90 mm, 210 mm)
Sensor4	(213 mm, 218 mm)	(210 mm, 210 mm)

Table 3. Material properties of CFRP specimen

Elastic constants of lamina
$E_1=135.0\text{GPa}$ , $E_2=E_3=10.0\text{GPa}$ , $G_{12}=G_{13}=5.50\text{GPa}$ , $G_{23}= 4.50\text{GPa}$ $\nu_{12}=0.0183$ , $\nu_{13}=0.45$ , $\nu_{23}=0.25$ , $\rho=1489 \text{ kg/m}^3$

Table 4. Impact test results

Case No.	Impact energy (J)	Damage
1	3.0	none
2	3.0	none
3	4.8	none
4	4.8	damaged
5	6.0	damaged
6	6.0	damaged
7	7.2	damaged
8	7.2	damaged

# **Damage Identification of Metallic Structures Using $A_0$ Mode of Lamb Waves**

Ning Hu<sup>1</sup>, Takahito Shimomukai<sup>1</sup>, Hisao Fukunaga<sup>1</sup>  
and Zhongqing Su<sup>2</sup>

<sup>1</sup>*Department of Aerospace Engineering, Tohoku University, Aramaki-Aza-Aoba 6-6-01,  
Aoba-ku, Sendai 980-8579, Japan*

<sup>2</sup>*Department of Mechanical Engineering  
The Hong Kong Polytechnic University, Hong Kong SAR, China*

The corresponding author's information:

Title: Associate Professor (Ning Hu)

Affiliation: Department of Aerospace Engineering, Tohoku University

Address: Aramaki-Aza-Aoba 6-6-01, Aoba-ku, Sendai 980-8579, Japan

E-mail: [hu@ssl.mech.tohoku.ac.jp](mailto:hu@ssl.mech.tohoku.ac.jp)

Web Page: <http://www.ssl.mech.tohoku.ac.jp/>

Running title: Damage identification using  $A_0$  mode in Lamb wave

## ABSTRACT

In the work, a Lamb wave-based technique was developed for detecting damages in metallic structures, such as cracks and holes in metallic beams and plates. For metallic structures with transverse cracks and holes,  $A_0$  mode of Lamb waves was employed due to its shorter wave length compared with  $S_0$  mode, which leads to high sensitivity to small damages. Two kinds of excitation techniques for generating comparatively pure  $A_0$  mode using piezoelectric lead zirconate titanate (PZT) actuators were realized experimentally. In one technique, two PZT actuators with applied out-of-phase voltages were attached on both sides of the structures. While in the other one, a kind of grease lubricant was used between the bottom surface of one PZT actuator and the surface of the specimens. Both techniques were able to enhance the component of  $A_0$  mode and reduce the component of  $S_0$  mode effectively. Secondly, in terms of the arrival time of the  $A_0$  wave mode reflected from damages obtained using the wavelet analysis, the positions of damages were identified accurately. The above two techniques were then validated by identifying the transverse cracks and holes in aluminum beams and plates, respectively. Numerical simulations using the finite element method (FEM) for the wave propagation in these structures with damages were carried out. The obtained experimental and numerical results demonstrate that it is possible to identify damage position very accurately by using only sensor data of defective structures without referring benchmark signals (sensor data of intact structures).

Keywords: Lamb wave •  $A_0$  mode • metallic structures • damage identification • FEM



## 1 INTRODUCTION

In order to improve the safety, reliability and operational life of various structures, the development of efficient techniques for non-destructive damage detection or structural health-monitoring is essential. Lamb wave can propagate a long distance in plate-like and shell-like structures made of materials even with high attenuation ratio (e.g. CF/EP composites), by virtue of this advantage, many researchers have recently examined Lamb waves as an means for damage identification [1]. Up to date, many developed Lamb wave-based techniques detect damage using a two-stage prediction model to find the difference in the signals between defective structure and benchmark, i.e. intact structure, for defining the *residual error* no matter what kind of information inherited in signals is used, such as the information in the time domain [2, 3] or in the frequency domain [4, 5]. Therefore, a benchmark or baseline signal is essential for comparison, which is very suitable for monitoring the propagation of damages with high reliability. On the other hand, tremendous efforts [6-8] have been directed to solve the damage identification problem as an inverse pattern recognition problem through comparison between theoretical results and experimentally captured signals, including artificial neural network etc. Most of these techniques do not need the baseline data of intact structures, although they may be referred to, e.g. in [8]. This kind of techniques, which provide the detailed information for damage, needs a careful verification of the effectiveness of the theoretical or numerical models by comparing with the experimental data so as to increase the reliability and accuracy.

No matter if the benchmark is referred to or not, an important issue in all the Lamb wave-based approaches is the proper selection of Lamb mode. Generally, Lamb wave has two fundamental modes, i.e., symmetric mode (*S* mode), and anti-symmetric mode (*A* mode). The basic symmetric mode,  $S_0$ , and the anti-symmetric mode  $A_0$ , are widely used in practice. Usually,  $S_0$  mode is preferred in the majority of studies [9, 10] since it

can travel a long distance. Also, it is comparatively easier to pick up  $S_0$  mode from complex Lamb wave signals containing multi-modes, since the reflected  $S_0$  mode waves from damages always arrive at sensors earliest due to its much higher propagation speed compared with that of  $A_0$  mode. However, within the comparatively lower frequency domain, such as several hundreds of kHz, the wavelength of  $A_0$  mode is much smaller than that of  $S_0$  mode so that it is more sensitive to some tiny damages, in recognition of the fact that the wavelength of the selected mode must be lower than or equal to the size of the damage. In recent, utilization of  $A_0$  mode is increasing and its outstanding ability to detect delamination and transverse cracks has been well recognized. There exist various kinds of methods to generate a pure mode of Lamb wave mode, such as using ultrasonic probes coupled with angle-adjustable perspex wedges or electro-magnetic acoustic transducers. However, it is not an easy task to generate pure  $A_0$  mode using simple PZT elements, although PZT possess many merits, such as wide frequency responses, excellent mechanical strength, low power consumption and acoustic impedance, as well as low cost. For this purpose, some studies have been performed. For instance, a multi-element transducer set-up was proposed for composite laminated beams [13]. By carefully choosing the distance between two PZT elements, the normal displacement of  $A_0$  mode can be maximized and that of  $S_0$  mode can be minimized. Another approach [14] is to attach a pair of PZT actuators symmetrically on the upper and lower surfaces of a composite laminate. Then,  $A_0$  mode can be excited using the applied out-of-phase voltages on two actuators. Of course, as commented on in [13, 14], these mode selection techniques cannot remove  $S_0$  mode completely.

In spite of some available achievements, further efforts are still requested to apply the Lamb wave-based techniques to some more practical cases with higher reliability and accuracy. With the previous background in mind, two important issues have been focused on in the current work. The first one is about the baseline data of intact structures. The damage identification without referring the baseline data is always

preferred, which was explored in the study. To realize this purpose, simple and clear Lamb wave signals containing only a single wave mode are preferred, which lead to another important issue in this work: generation of pure  $A_0$  mode, which was implemented by using PZT actuators. For the damage identification in metallic structures, two kinds of  $A_0$  mode generation techniques were experimentally developed. In the first one, two PZT actuators with applied opposite voltages on both sides of structures were attached on the host structure. In the second one, a kind of grease lubricant between the bottom surface of one actuator and the surface of specimens was used. Both techniques can generate comparatively pure  $A_0$  mode Lamb waves, which are able to travel through a wide range up to several hundreds of *mm* or longer as observed in the experiments but with reasonably low dispersion. With these techniques and comparatively low excitation frequency with low noises, very clear wave signal containing  $A_0$  mode only were captured, clearly highlighting those reflected wave components from damages. The group speeds of  $A_0$  mode in an aluminum plate were experimentally measured by virtue of wavelet transformation technique. These experimental values were further compared with those values predicted theoretically using Rayleigh-Lamb equation. Then, in terms of the wave propagation speeds and the arrival time of reflected waves from damages identified by the wavelet transformation technique, the positions of damages were identified accurately. An obvious merit of the present technique is that there is no need of the benchmark data of intact structures. For beam-like aluminum structures with transverse cracks, the first kind of  $A_0$  mode generation technique with two actuators and one sensor was employed. For aluminum plate structures, the second kind of  $A_0$  mode generation technique was employed. In this case, a kind of transducer set containing three sensors and one actuator was developed. A small hole and a very short crack in the plate were considered. The numerical simulations using FEM were also carried out for two cases, and it can be found that the numerical results agree with the experimental ones very well.

## 2 DETERMINATION OF GROUP VELOCITY of A<sub>0</sub> LAMB MODE IN ALUMINUM STRUCTURES

The formulations of Rayleigh-Lamb equation for computing the phase and group velocity can be described as follows [15]:

For symmetrical modes (S mode):

$$\frac{\tan \sqrt{1 - \zeta^2} \bar{d}}{\tan \sqrt{\xi^2 - \zeta^2} \bar{d}} = - \frac{4\zeta^2 \sqrt{1 - \zeta^2} \sqrt{\xi^2 - \zeta^2}}{(2\zeta^2 - 1)^2} \quad (1a)$$

and for anti-symmetrical modes (A mode)

$$\frac{\tan \sqrt{1 - \zeta^2} \bar{d}}{\tan \sqrt{\xi^2 - \zeta^2} \bar{d}} = - \frac{(2\zeta^2 - 1)^2}{4\zeta^2 \sqrt{1 - \zeta^2} \sqrt{\xi^2 - \zeta^2}} \quad (1b)$$

where

$$\bar{d} = kd = 2\pi f \bar{t} \sqrt{\frac{\rho}{\mu}} \quad (2)$$

where  $\bar{t}$  is half the plate thickness,  $\rho$  is the mass density,  $\mu$  is the elastic Lamé constant, i.e. the shear modulus,  $\mu = \frac{E}{2(1 + \nu)}$ .

Also,

$$\zeta^2 = \frac{c_t^2}{c^2}, \quad \xi^2 = \frac{c_t^2}{c_l^2} \quad (3)$$

where

$c_l$ : the longitudinal wave velocity, 6138 m/s for aluminum

$c_t$ : the transverse shear wave velocity, 3102 m/s for aluminum

$\lambda$ : the wavelength

$c$ : the phase velocity of wave propagation and  $c = \omega / k$

where  $\omega$  is the circular frequency, and wave number  $k$  can be expressed as follows

$$k = \frac{2\pi}{\lambda} \quad (4)$$

Finally, it has

$$c = \lambda\omega / 2\pi = \lambda f, \quad \lambda = c / f \quad (5)$$

where  $f$  is the frequency.

To avoid the equation of complex numbers, in the practical computation, the following equations were employed by transferring the terms on both sides from equations (1a) and (1b)

$$\frac{\tan \sqrt{1-\zeta^2} \bar{d}}{4\zeta^2 \sqrt{1-\zeta^2}} = -\frac{\sqrt{\xi^2 - \zeta^2} \tan \sqrt{\xi^2 - \zeta^2} \bar{d}}{(2\zeta^2 - 1)^2} \quad (6a)$$

$$\frac{\sqrt{1-\zeta^2} \tan \sqrt{1-\zeta^2} \bar{d}}{(2\zeta^2 - 1)^2} = -\frac{\tan \sqrt{\xi^2 - \zeta^2} \bar{d}}{4\zeta^2 \sqrt{\xi^2 - \zeta^2}} \quad (6b)$$

The bi-division method was employed to solve the above two nonlinear equations numerically.

To calculate the group velocity, the relation proposed by Rose [16], shown as below, was adopted,

$$c_g = c^2 [c - f \frac{dc}{df}]^{-1} \quad (7)$$

Here, for an arbitrary frequency  $f=f_0$ , the forward difference method was used to compute:  $\frac{dc}{df} = \frac{c_1 - c_0}{f_1 - f_0}$ , where  $f_1=f_0+\Delta f$ . It was found that  $\frac{dc}{df}$  was very stable to the

different choice of  $\Delta f$ , for instance, in the computation,  $\Delta f$  was chosen from 0.1~1.0.

By using a square aluminum plate of 5 mm in thickness as shown in Figure 1, with two actuators with applied out-of-phase voltages which were attached on the top and bottom surfaces of plate, respectively (Figure 2), the group speed of  $A_0$  mode was measured for excitation frequency ranging from 10 kHz to 300 kHz. The circular actuator and sensor were of 10 mm in diameter and 0.5 mm in thickness. For the case

when 80 kHz excitation was adopted, the captured signals of sensors 1~3 are shown in Figure 3. From it, it can be found that very pure  $A_0$  mode was generated. Also, the reflected waves from the boundaries of plate can be identified clearly. By employing the wavelet transformation technique [17], the arrival time of incident  $A_0$  mode can be determined exactly. In the approach, the peak of the spectral intensities corresponding to the excitation frequency component as a function of time obtained by the wavelet transformation was used. Finally, the delay of arrival time of incident wave and distances between three sensors were used to calculate the group velocity of  $A_0$  mode. The average group velocity of  $A_0$  mode determined by experiments and theoretical group velocity evaluated from the above Rayleigh-Lamb equation with the material properties in Table 1 are plotted in Figure 4(a). From this figure, it can be observed that both results agree very well, the maximum error between the experimental results and theoretical ones is 5.4%. Also, the comparison of theoretically predicted wavelengths of  $A_0$  mode and  $S_0$  mode is shown in Figure 4(b). As seen the wavelength of  $A_0$  mode is much smaller than that of  $S_0$  mode. For example, at 50 kHz and 200 kHz (to be used in the following experiments), the wavelength of  $A_0$  mode is smaller than that of  $S_0$  mode by around 4 times and 2 times, respectively.

### 3 ALUMINUM BEAMS WITH TRANSVERSE CRACKS

First, an aluminum beam with surface transverse cracks, which were modeled by notches with a very narrow width (around 0.2 mm) in experiments, are shown in Figure 5. The material properties of the cantilevered aluminum beam are given in Table 1. Two kinds of beam thicknesses were considered, i.e., 3 mm and 5 mm, respectively. For transverse cracks, two kinds of damage patterns were considered. One was a single crack on one side of the beam, and the other was double cracks on both sides of the beam. Also, as shown in Figure 5, the same actuator configuration as that in Figure 2 was employed to experimentally generate comparatively pure  $A_0$  mode. The dimensions

of square PZT actuator and sensor were  $10\text{ mm}\times 10\text{ mm}\times 0.5\text{ mm}$ . A very strong adhesive was used between the specimen surface and PZT surface. The excitation signal was of 50 kHz frequency and 5 cycles for experiments on beams. For this excitation frequency, by referring to Figure 4(a),  $A_0$  mode should be of high dispersion, which is the main reason that  $A_0$  mode is not used in typical long distance damage detection scenarios. However, for the long beam in Figure 5, the wave dispersion is not so obvious, at least for the reflected signal from cracks which travels around 600 mm. From our experimental experiences, usually,  *$A_0$  mode can be generated more easily when the actuator is thin and excitation frequency is comparatively low.*

For the aluminum beam in Figure 5, numerical simulations by using a hybrid 3D finite element proposed by the authors [18] combined with the explicit time integration algorithm were performed. The efforts for increasing the computational speed in our FEM code have been done. In computations, within one wavelength, at least ten elements are used. The material properties of PZT are listed in Table 2. Note that for the computation of this one-dimensional problem,  $d_{32}$  was neglected. For intact beam of 5 mm in thickness, the comparison between the numerical results and experimental ones is shown in Figure 6(a), where the damping coefficient used in the numerical model was obtained by comparing the amplitudes of reflected waves from two ends of the beam in numerical and experimental results. For beams of 5 mm in thickness with 1.25 mm single crack on one side and 1.25 mm double cracks on both sides, the comparison of numerical and experimental results are shown in Figures 6(b) and 6(c), respectively. From them, both results are coincident to each other very well. The effectiveness of numerical model was verified, which can facilitate the identification of damage size in future applications. In Figures 6(b) and 6(c), the first blob is the incident wave. Between the incident wave and the reflected waves from boundaries, we can clearly identify a distinct blob, i.e., the reflected waves from cracks. To investigate the influence of crack depth  $d$  on the amplitude of reflected waves of crack, for beams of 3 mm and 5 mm in

thickness with single crack, the experimental results are shown in Figures 7 and 8, respectively. From these figures, it can be found that when the crack depth is  $0.25\text{ mm}$ , there is no obvious reflection from damages for both cases. When the crack depth is larger than  $0.5\text{ mm}$  for  $3\text{ mm}$  beam and  $0.75\text{ mm}$  for  $5\text{ mm}$  beam, respectively, very clear reflections from cracks can be identified. Also, with the increase of crack depth, the amplitude of reflected waves from damages was observed to increase too. The same results can also be found for double sided cracks.

Finally, by employing the arrival time of reflected wave from cracks determined by the wavelet transformation technique plus the information of the group velocity of  $A_0$  mode at  $50\text{ kHz}$  shown in Figure 4(a), the positions of cracks were identified for both numerical and experimental models, detailed in Table 3. From it, it is noted that the position of cracks can be identified very accurately. Compared with the case of beam of  $3\text{ mm}$  in thickness, the errors of positions of cracks in the beam of  $5\text{ mm}$  in thickness are slightly lower.

#### **4 ALUMINUM PLATES WITH CIRCULAR HOLE AND TRANSVERSE CRACK**

To generate  $A_0$  mode of Lamb waves more conveniently, besides the above technique with double-sided attached actuators, a simpler technique has also been developed. In this technique, we applied a kind of grease lubricant under the bottom surface of actuator. The mechanism of this technique is to generate the vertical pressure from the actuator on the plate to excite  $A$  mode, and the strong shear force between the actuator and the plate is remarkably weakened since this shear force can excite  $A$  and  $S$  modes simultaneously when the actuator is not located on the mid-plane of plate. Also, due to the existence of the grease as wave propagation media, the signal from actuator does not attenuate significantly. To move the sensor freely, a kind of two-sided tape made of polypropylene film with weak acrylic adhesive was used between the bottom



surface of sensor and the top surface of plate. By employing the above technique, very pure  $A_0$  mode of Lamb waves can be generated. The comparison of wave forms, when using three bonding methods between the bottom surface of actuator and sensor, and the top surface of plate, is shown in Figure 9. The distance between the actuator and the sensor was 200 *mm* and the excitation signal was of 200 kHz frequency and 5 cycles. By referring to Figure 4(a), for this excitation frequency,  $A_0$  mode is almost non-dispersive. The ratios of amplitudes of  $S_0$  and  $A_0$  modes in three methods are shown in Table 4. From Figure 9 and Table 4, we can find the grease lubricant used for actuator and the two-sided type used for sensor can remove  $S_0$  mode effectively although the excited  $A_0$  mode seems to have more cycles due to the usage of grease, which however was observed to apply neglectable influence on identification accuracy. Of course, this technique leads to the slightly shorter wave propagation distance compared with the first technique in beams. However, it is still enough to cover the large area ranging up to several hundreds *mm* depending on the excitation frequency. A very simple technique to enhance the signal in this case was to apply a constant vertical pin-load on a small area of the center of sensors. It has been found that the signal amplitude of sensor was enlarged by several times compared with that without applying such a vertical pin-load.

As stated in the above example, in this study, an important feature is to catch the reflected waves from damages directly without referring the data of pre-damaged state. Therefore, the intensity of the reflected waves from damages is a key factor for accurately identifying the positions of damages. For 2-dimensional plate problems, to investigate the intensity of the reflected waves from damages, first, the numerical computations were performed. As shown in Figure 10, for an aluminum plate with a hole of 20.0 *mm* in diameter, when the sensors were arranged around the hole, we computed the intensity of reflected waves from damages. The circular PZT actuator and sensor fixed on the surface of the plate with the properties in Table 2 were of 10 *mm* in diameter and 0.5 *mm* in thickness. The excitation signal was of 200 kHz frequency and

5 cycles. The configurations of wave propagation at the different time steps are shown in Figure 11, from which, we can identify the reflected wave from the hole very clearly. In this computation, both  $S_0$  and  $A_0$  modes were observed to exist. The amplitudes of the reflected wave from the hole for the sensors located on the different angles were obtained from the difference of wave signals ( $S_0$  mode) of the same plate without a hole and the plate with a hole. The maximum amplitude of the reflected wave from the hole at one sensor was used to normalize the others. The normalized intensity of reflected waves from the hole is shown in Figure 12. This result illustrates that when the angle between the line connecting the actuator and the damage and the line connecting the damage and the sensor is very small, the intensity of reflected wave from the hole is very high. However, with the increase of this angle, the intensity drops very rapidly. Since the position of damage was unknown beforehand, a kind of transducer set was designed, which contains a centered actuator and three sensors located at the outer circumference as shown in Figure 13(a). The distance between the actuator and the sensor was small, i.e. 50 mm. The angle between the line connecting the actuator to one sensor and the line connecting the actuator to another sensor was 120°. Therefore, no matter where the damage was located, comparatively strong reflected waves from damages were captured at one sensor at least. An important merit of this transducer set is that it can be moved freely in a large area for damage detection purpose. For the case shown in Figure 13(a), the distance from the actuator to damage is assumed as  $s$ , and the distances from sensors A, B and C to damage are assumed as  $a$ ,  $b$  and  $c$ , respectively. At first, we define the following variables,

$$a' = a + s \quad (8a)$$

$$b' = b + s \quad (8b)$$

$$c' = c + s \quad (8c)$$

From the measured experimental data using three sensors, the arrival times of the reflected waves from damages were obtained from the wavelet transformation, and then

the distances  $a'$ ,  $b'$  and  $c'$  were calculated by virtue of wave propagation velocity. Finally, the unknown parameters  $a$ ,  $b$ ,  $c$  and  $s$  could be obtained easily. For example,  $s$  can be expressed as follows

$$s = \frac{a'^2 + b'^2 + c'^2 - 3r^2}{2(a' + b' + c')} \quad (9)$$

where  $r$  is the distance from the actuator to the sensor in Figure 13(a) with the known value.

Finally, after determining the parameters of  $a$ ,  $b$ ,  $c$  and  $s$ , three circles with the centers of three sensors respectively can be drawn and the intersection of them is namely the position of damage. As one example of validation, a transducer set was made, shown in Figure 13(b), which contains the centered actuator and three surrounding sensors. Four screws passing through a top circular plate possessed a very small flat bottom tip, where the PZTs were attached. The screws can adjust the positions of PZTs along the vertical directions of specimen for possible curved structures. This set can be moved on the surface of specimen freely, and the vertical load on sensors can be increased conveniently by putting some weights on the top circular plate. From our experiences, it is better to avoid the strong vertical load applied on the actuator for obtaining the clear wave form. However, a suitable vertical load on sensors is preferred, which can increase the signal amplitudes. This can be easily realized by adjusting the positions of four screws along the vertical direction. It should be noted that without this equipment, by only directly placing the actuator and sensors on the surface of plate, sufficiently good signals could still be captured.

#### 4.1 An aluminum plate with a hole

An aluminum plate of 5 mm in thickness with a hole of diameter of 20.0 mm is shown in Figure 14, on which the transducer set was placed. The dimensions of PZT actuator and sensor and the excitation signal were the same with those in the above

numerical example. The excitation frequency was chosen at such a frequency at which the incident wave and the reflected wave from damage can be easily separated. In this example, since the distance between the transducer set and the damage was comparatively small, the higher excitation frequency was chosen. A typical wave signal of sensor B is plotted in Figure 15, where the reflected wave from the hole can be clearly identified. Also, only  $A_0$  mode was noticed to be excited. The position of the hole is visually shown in Figure 16 by the three circles centered by three sensors. The detailed identified position of the hole is given in Table 5. Also, the numerical computation of FEM was performed, where some springs with high vertical stiffness and very weak in-plane stiffness were used between the actuator and the top surface of plate to simulate the effect of grease lubricant. In the numerically obtained wave forms,  $S_0$  was noticed to be removed effectively. The numerically identified position of the hole is detailed in Table 6. From these results, we can find that both experimental and numerical approaches can provide very accurate results.

## 4.2 An aluminum plate with a transverse crack

An aluminum plate of 5 mm in thickness with a transverse crack is shown in Figure 17. The crack was modeled by a notch of length of 10 mm and width of 1 mm in experiments. The same transducer set and excitation signal as in Section 4.1 were used. When the angle  $\theta$  between the line connecting the actuator to the notch and the length direction of the crack was equal to  $90^\circ$  as shown in Figure 17, a typical signal of sensor C is shown in Figure 18. From it, the reflected wave from the crack can be observed clearly. The identified position of the crack is given in Table 7. When the transducer set moved to decrease the angle  $\theta$ , for example, for the case of  $\theta=45^\circ$  as shown in Figure 19, the reflected wave from the crack can be identified very clearly from the corresponding signal of sensor A in Figure 20. The crack position is also visually demonstrated in Figure 21 for this case. The identified position of the crack is given in Table 8, where the accuracy is very high. From experimental experiences, the limit of the angle  $\theta$  for

clearly identifying the position of crack is  $22.5^\circ$ . The results for  $\theta = 22.5^\circ$  is shown in Table 9, where we can still identify the position of crack within the acceptable accuracy. When  $\theta$  is smaller than  $22.5^\circ$ , satisfactory identification accuracy may not be guaranteed due to very weak reflected wave from the crack.

In the above technique, since no benchmark data of pre-damaged structures were used, a question arises naturally. How to interpret which blob in sensor signals is the reflected wave from damage? To answer this question, the following several aspects should be considered. When multi-modes in Lamb waves are excited simultaneously, it is not easy to pick up the correct components of  $A_0$  mode reflected from the damages from a very complex signal configuration. In our cases, as shown in figures, comparatively simple signals were obtained since only  $A_0$  mode possesses the visible amplitude. Therefore, it is not so difficult to select the blob in signals representing the reflected wave from damages. First, for the first blob, i.e., the incident wave, which arrives at sensors from an actuator directly, it is not difficult to judge it with known wave propagation speed of  $A_0$  mode and the distance from the actuator to sensors. Also, the amplitude of this blob is quite bigger than others, e.g. the wave signals reflected from boundaries or damages, which travel through much longer distances. The comparatively difficult thing is to separate the signal of damages from signals of boundaries. This case can be divided into three kinds of sub-cases. For the first one, the reflected signal from damages, which is not overlapped with the signals from boundaries, can be identified distinctly. In this case, since the positions of transducer set and specimen dimensions and the wave propagation velocity are known beforehand. It is easy to interpret which blob is the reflected wave from damages and which blobs are the reflected waves from boundaries. For the second one, the signal from damages is partially overlapped with the signals from boundaries. This situation may happen when the damages are located close to boundaries. In this case, we can still interpret the reflected wave from damages by employing the information of the positions of

transducer set and specimen dimensions, and wave propagation velocity. The numerical simulations were conducted when a hole was located very close to boundaries, such as 40 *mm* in distance. In this case, we could still identify the hole with the excitation signal of 200 kHz frequency and 5 cycles although the reflected wave from the hole was partially overlapped with the signals from boundaries. An effective means in this case is to increase the excitation frequency and meanwhile reduce the cycle number of excitation signal. It can shorten the duration time of one blob and increase the resolving capability for isolating the different blobs more easily. For the third case, when the reflected wave from damages are completely overlapped with the signals from boundaries. This situation may happen when the damages are located very close to or right on the specimen boundaries. In this case, the present approach may lose its effectiveness.

Generally, a very intuitive means to judge the reflected wave from damages in sensor signals is that usually the amplitude of signal from tiny damages, which cannot reflect the enormous wave energy back to sensors, is much smaller than those of incident wave and reflected waves from boundaries.

## **5 CONCLUSIONS**

In this study, we have experimentally realized two kinds of techniques to excite the  $A_0$  mode of Lamb waves using PZT actuators.  $A_0$  mode was employed for identifying the damages in metallic structures due to its shorter wave length leading to the higher sensitivity to small damages. The first technique used two actuators attached on the top and bottom surfaces with the applied out-of-phase voltages; and the second technique employed a one-sided actuator and a kind of grease lubricant between the bottom surface of actuator and the top surface of structures. Both techniques have been demonstrated to generate comparatively pure  $A_0$  mode with undetectable  $S_0$  mode in wave signals. Therefore, very clear wave form can be obtained for more conveniently picking up the reflected  $A_0$  wave from damages. A removable transducer set was

designed when the second excitation technique employed for the actuator by combining with a kind of two-sided tape used between the bottom surface of sensors and top surface of specimen. This transducer set consisted of a centered actuator and three surrounding sensors, which can receive the possibly reflected wave from damages with high intensity. The arrival time of reflected wave from damages determined by a wavelet transformation technique was used to locate the damage combined with the wave propagation velocity of  $A_0$  mode. Both aluminum beams with transverse cracks and aluminum plates with a hole or a transverse crack were used to verify the present technique. It has been found that without the benchmark data of pre-damaged structures, the positions of damages can still be identified by focusing on the reflected  $A_0$  wave from damages. In parallel, the numerical simulations of FEM were carried out with high accuracy by comparing with the experimental data..

#### Acknowledgements

This work is partly supported by the Award from AFOSR numbered by AOARD-06-4066 and Natural Science Foundation Project of CQ CSTC.

#### References

1. Su, Z.Q., Ye, L. and Lu, Y. (2006). Guided Lamb waves for identification of damage in composite structures: A review. *Journal of Sound & Vibration*, 295(3-5), 753-780.
2. Valdes, S.H.D., Soutis, C. (2001). A structural health monitoring system for laminated composites. *Proceedings of DETC*, Pittsburgh, PA, USA.
3. Sohn, H., Farrar, C.R. (2001). Damage diagnosis using time series analysis of vibration signals. *Smart Materials and Structures*, 10, 1-6.
4. Ihn, J.B. and Chang, Fu-Kuo. (2001). Built-in diagnostics for monitoring crack growth in aircraft structures. In: Chang, Fu-Kuo (ed.), *Proceedings of the international workshop on structural health monitoring*. Stanford University, USA.

5. S. Hurlesbaus, S., Niethammer, M., Jacobs, L.J., and Valle, C. (2001). Automated methodology to locate notches with Lamb waves. *Acoustics Research Letters Online*, 2, 97-102.
6. Bork, U., Challis, R.E. (1994). Artificial neural networks applied to Lamb wave testing of T-form adhered joints. In: Saffari, N. (ed.), *Proceedings of the Conference on the Inspection of Structural Composites*, Bentham Press.
7. Su, Z., Ye, L. (2004). Lamb wave propagation-based damage identification for quasi-isotropic CF/EP composite laminates using artificial neural algorithm, Part-I: methodology and database development. *Journal of Intelligent Material Systems and Structures*, 16, 97-111.
8. Zang, C. Friswell, M.I. and Imregun, M. (2004). Structural damage detection using independent component analysis. *Structural Health Monitoring: An International Journal*. 3(1), 69-83.
9. Lemistre, M. and Balageas, D.L. (2001). Structural health monitoring system based on diffracted Lamb wave analysis by multiresolution processing. *Smart Materials and Structures*, 10, 504-511.
10. Roh, Y.S. and Chang, Fu-Kuo (1995). Effect of impact damage on Lamb wave propagation in laminated composites. *Proceedings of ASME on Dynamic Responses and Behavior of Composites*, USA.
11. Monkhouse, R.S.C., Wilcox, P.W., Lowe, M.J.S., Dalton, R.P. and Cawley, P. (2000). The rapid monitoring of structures using interdigital Lamb wave transducer. *Smart Materials and Structures*, 9, 304-309.
12. Kessler, S.S., Spearing, S.M. and Soutis, C. (2002). Damage detection in composite materials using Lamb wave methods. *Smart Materials and Structures*, 11, 269-278.
13. Grondel, S., Paget, C., Delebarre, C., Assaad, J. and Levin, K. (2002). Design of optimal configuration for generating  $A_0$  Lamb mode in a composite plate using piezoelectric transducers. *Journal of the Acoustical Society of America*, 112, 84-90.



14. Su, Z. and Ye, L. (2004). Selective generation of Lamb wave modes and their propagation characteristics in defective composite laminates. *Journal of Materials: Design and Applications*, 218, 95-110.
15. Viktorov, I.A. (1976). *Rayleigh and Lamb Waves*, New York: Plenum press.
16. Rose, W.R. (1999). *Ultrasonic Waves in Solid Media*, Cambridge: Cambridge University Press.
17. Jeong, H. and Jang, Y.S. (2000). Wavelet analysis of plate wave propagation in composite laminates. *Composite Structures*, 49, 443-450.
18. Cao, Y.P., Hu, N., Lu, J., Fukunaga, H. and Yao, Z.H. (2002). A 3D brick element based on Hu-Washizu variational principle for mesh distortion. *Int. J. Numer. Meth. Engrg.*, 53, 2529-2548.

### Figure and Table Captions

Figure 1. A square plate with actuators and three sensors (length unit: *mm*)

Figure 2. Applied out-of-phase voltages on actuators on top and bottom surfaces

Figure 3. Signals of three sensors on the plate (80 kHz)

Figure 3(a). Signal of sensor 1

Figure 3(b). Signal of sensor 2

Figure 3(c). Signal of sensor 3

Figure 4. Comparison of wave velocity and wave length

Figure 4(a). Comparison of theoretical and experimental group velocities of  $A_0$  mode

Figure 4(b). Comparison of wavelength of  $A_0$  mode and  $S_0$  mode

Figure 5. Schematic view of aluminum beams with cracks (length unit: *mm*)

Figure 6. Comparison of numerical and experimental results for beam of 5 *mm* thickness

Figure 6(a). Numerical and experimental results of intact beam

Figure 6(b). Numerical and experimental results of beam with 1.25 *mm* single crack on one side

Figure 6(c). Numerical and experimental results of beam with 1.25 *mm* double cracks on two sides

Figure 7. Influence of crack depth on reflected waves from cracks for 3 *mm* beam

Figure 8. Influence of crack depth on reflected waves from cracks for 5 *mm* beam

Figure 9. Comparison of wave forms for three kinds of bonding methods

Figure 9(a) Strong adhesive used for actuator and sensor

Figure 9(b) Grease lubricant used for actuator and strong adhesive used for sensor

Figure 9(c) Grease lubricant used for actuator and two-sided tape used for sensor

Figure 10. Schematic view of aluminum plate for FEM computation

Figure 11. Configurations of wave propagation at various time steps

Figure 11(a). Istep=1500

Figure 11(b). Istep=9000

Figure 11(c). Istep=12000

Figure 11(d). Istep=15000

Figure 12. Normalized intensity of reflected wave from the hole versus angle of sensor

Figure 13. A designed transducer set containing one actuator and three sensors

Figure 13(a). Configuration of transducer set and damage

Figure 13(b). A hand-made transducer set

Figure 14. Schematic view of a plate with a hole and a transducer set

Figure 15. Signal of sensor B for a plate with a hole

Figure 16. Identified position of hole using three circles

Figure 17. Schematic view of an aluminum plate with a transverse crack ( $\theta=90^\circ$ )

Figure 18. Signal of sensor C for a plate with a crack

Figure 19. Schematic view of an aluminum plate with a transverse crack ( $\theta=45^\circ$ )

Figure 20. Signal of sensor A for a plate with a crack

Figure 21. Identified position of crack using three circles when  $\theta=45^\circ$

Table 1. Material properties of aluminum

Table 2. Material properties of PZT

Table 3. Results of identified crack position for 3 mm and 5 mm beams

Table 4. Ratio of amplitudes of  $S_0$  and  $A_0$  modes for various bonding conditions

Table 5. Experimental results of identified position of hole

Table 6. Numerical results of identified position of hole

Table 7. Experimental results of identified position of crack ( $\theta=90^\circ$ )

Table 8. Experimental results of identified position of crack ( $\theta=45^\circ$ )

Table 9. Experimental results of identified position of crack ( $\theta=22.5^\circ$ )

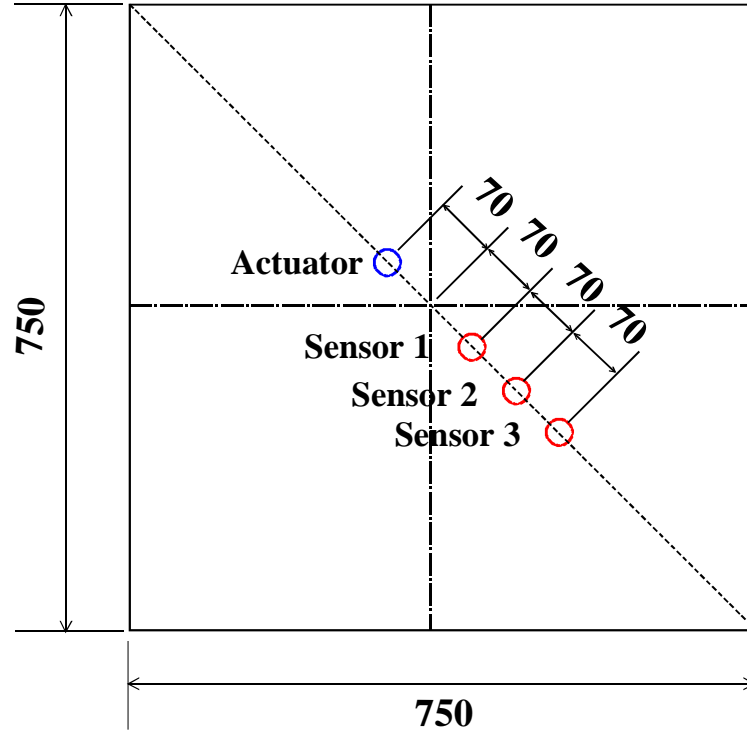


Figure 1. A square plate with actuators and three sensors (length unit: *mm*)

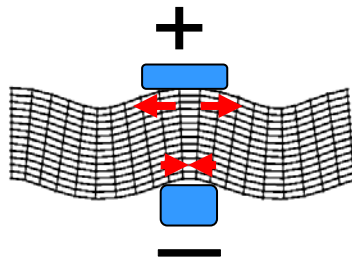
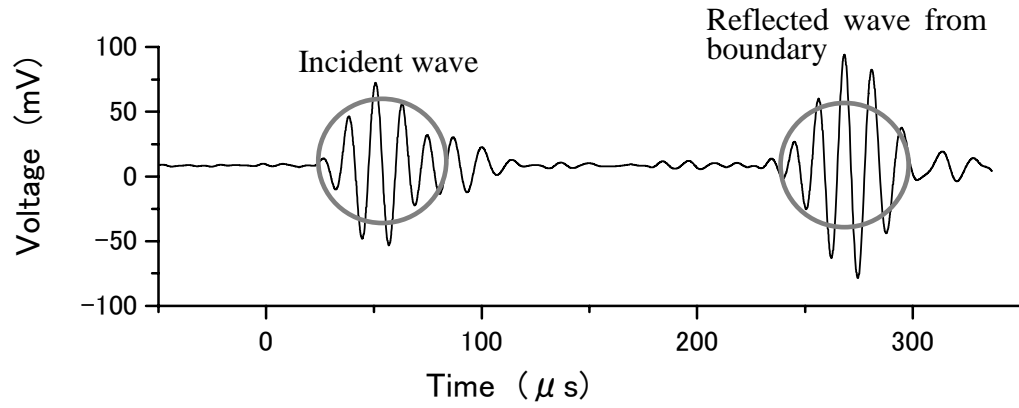
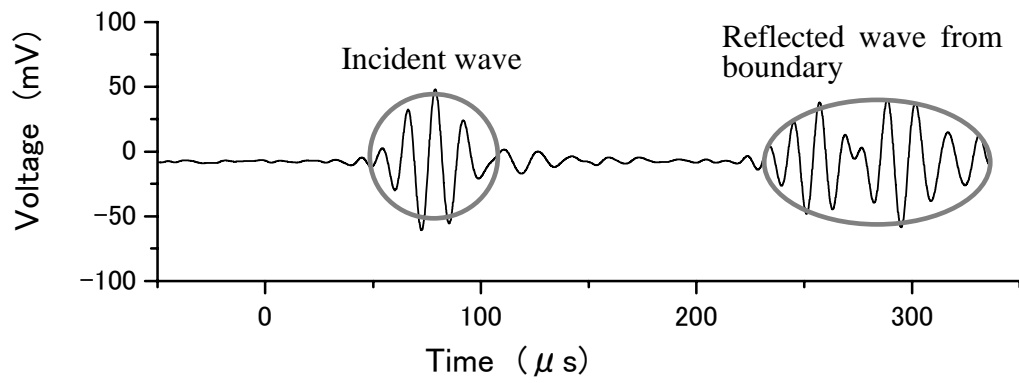


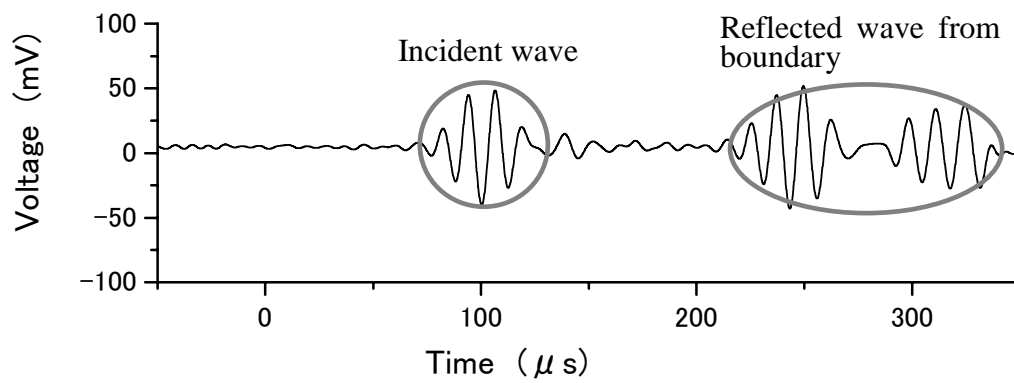
Figure 2. Applied out-of-phase voltages on actuators on top and bottom surfaces



a) Signal of sensor 1

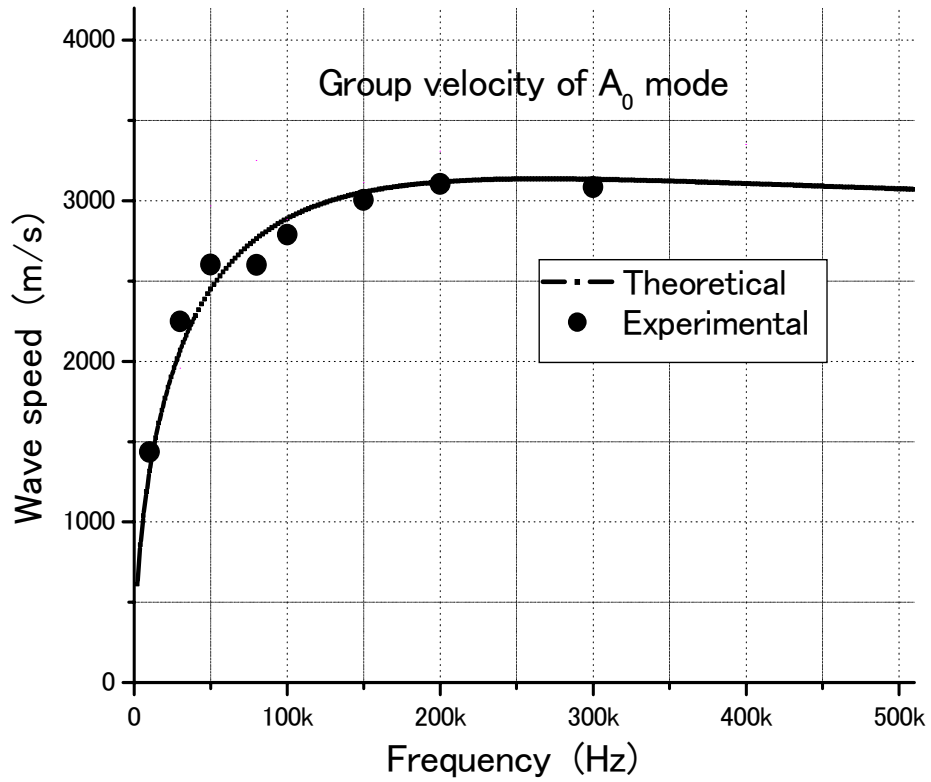


b) Signal of sensor 2

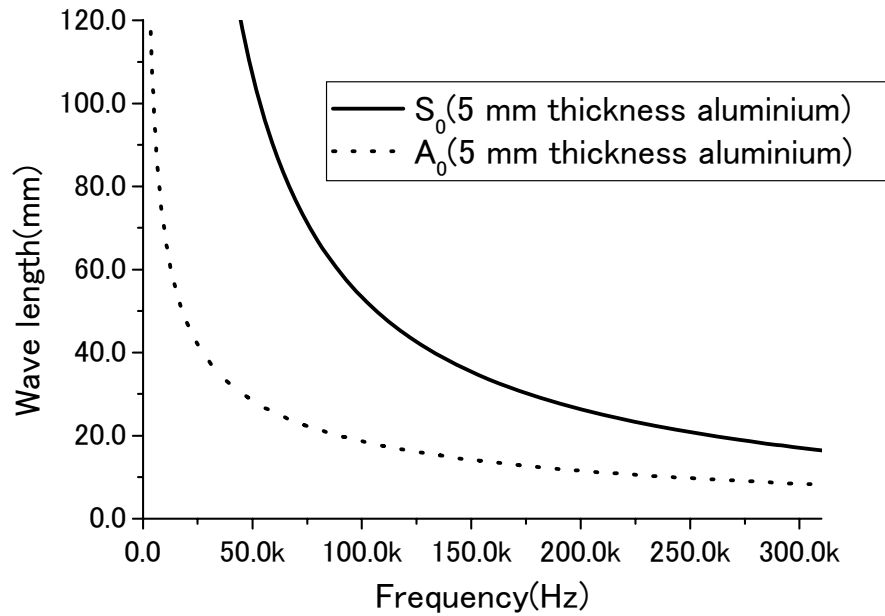


c) Signal of sensor 3

Figure 3. Signals of three sensors on the plate (80 kHz)

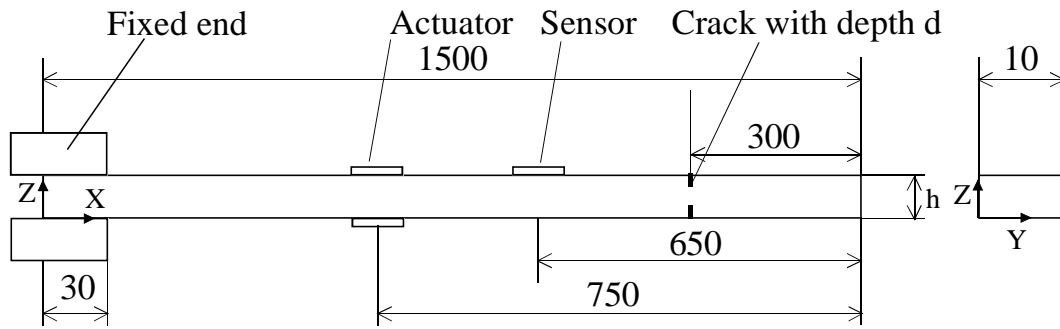
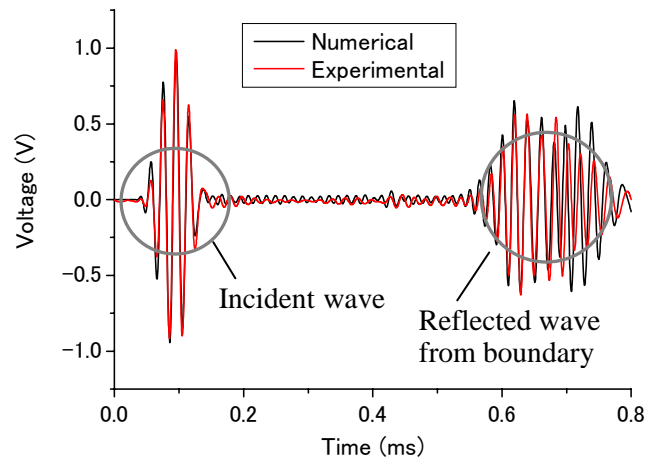


a) Comparison of theoretical and experimental group velocities of  $A_0$  mode

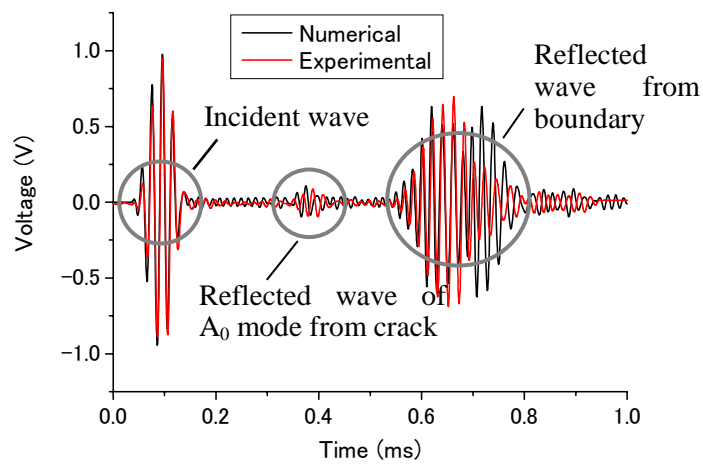


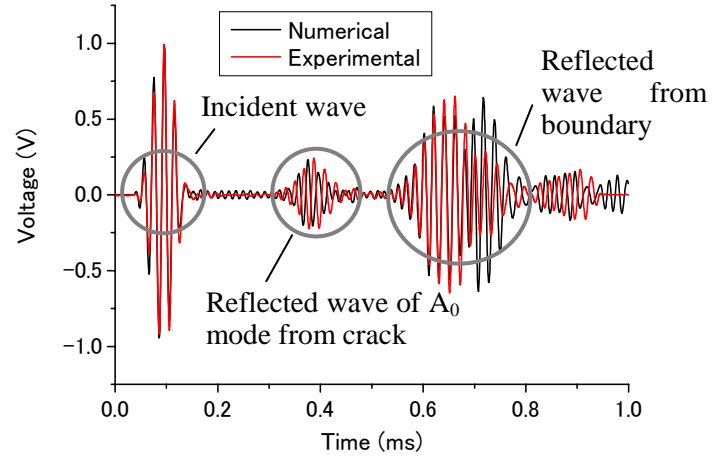
b) Comparison of wavelength of  $A_0$  mode and  $S_0$  mode

Figure 4. Comparison of wave velocity and wave length

Figure 5. Schematic view of aluminum beams with cracks (length unit: *mm*)

a) Numerical and experimental results of intact beam

b) Numerical and experimental results of beam with 1.25 *mm* single crack on one side



c) Numerical and experimental results of beam with 1.25 mm double cracks on two sides  
Figure 6. Comparison of numerical and experimental results for beam of 5 mm thickness

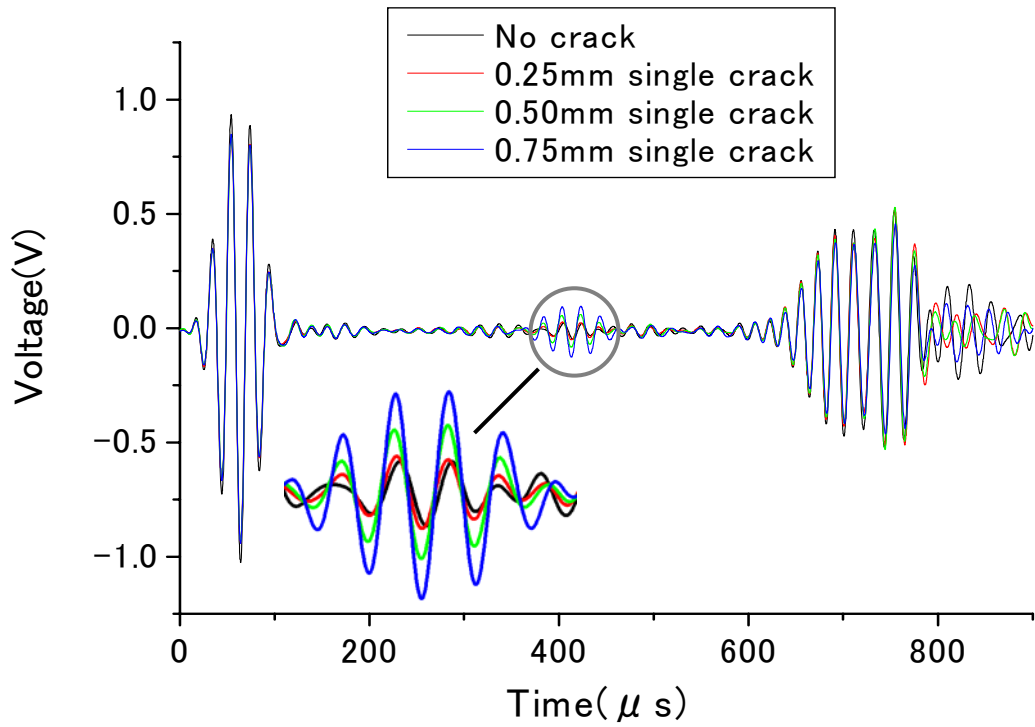


Figure 7. Influence of crack depth on reflected waves from cracks for 3 mm beam



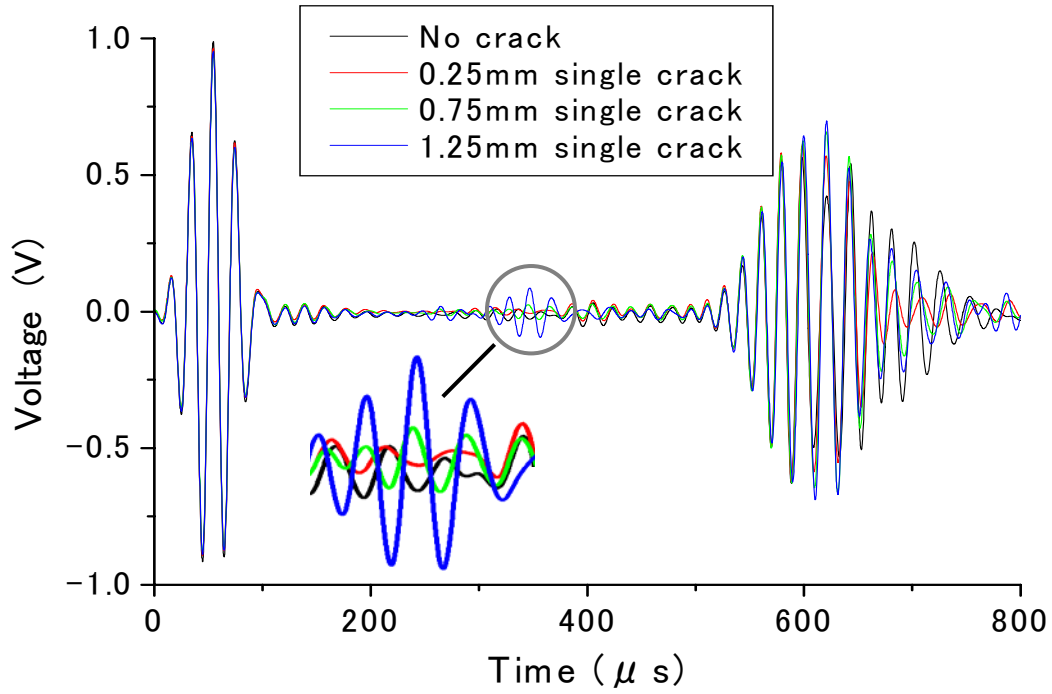
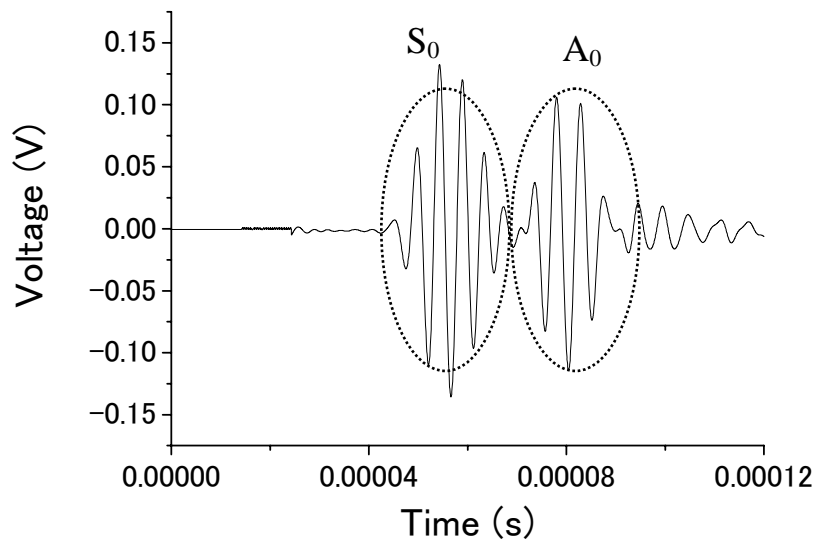
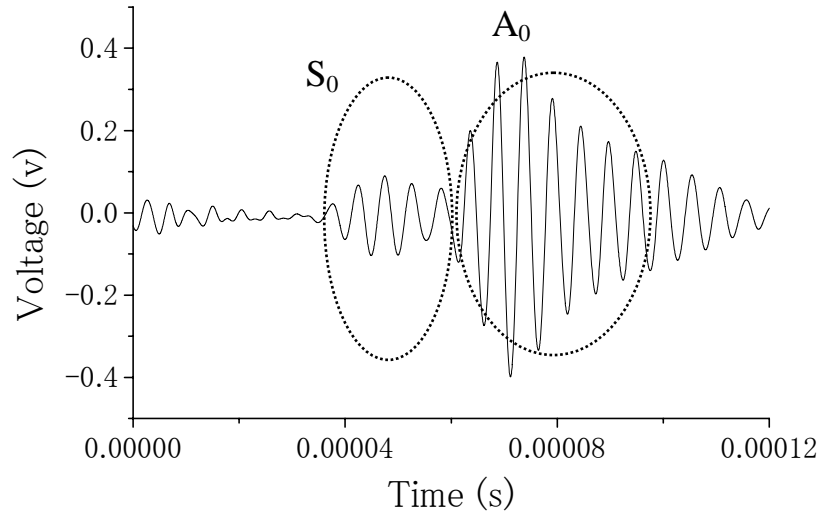


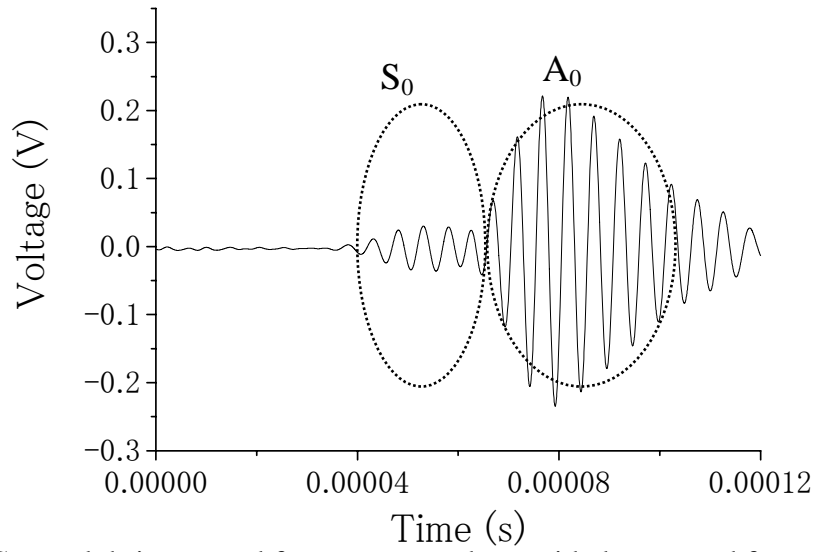
Figure 8. Influence of crack depth on reflected waves from cracks for 5 mm beam



a) Strong adhesive used for actuator and sensor



b) Grease lubricant used for actuator and strong adhesive used for sensor



c) Grease lubricant used for actuator and two-sided tape used for sensor

Figure 9. Comparison of wave forms for three kinds of bonding methods

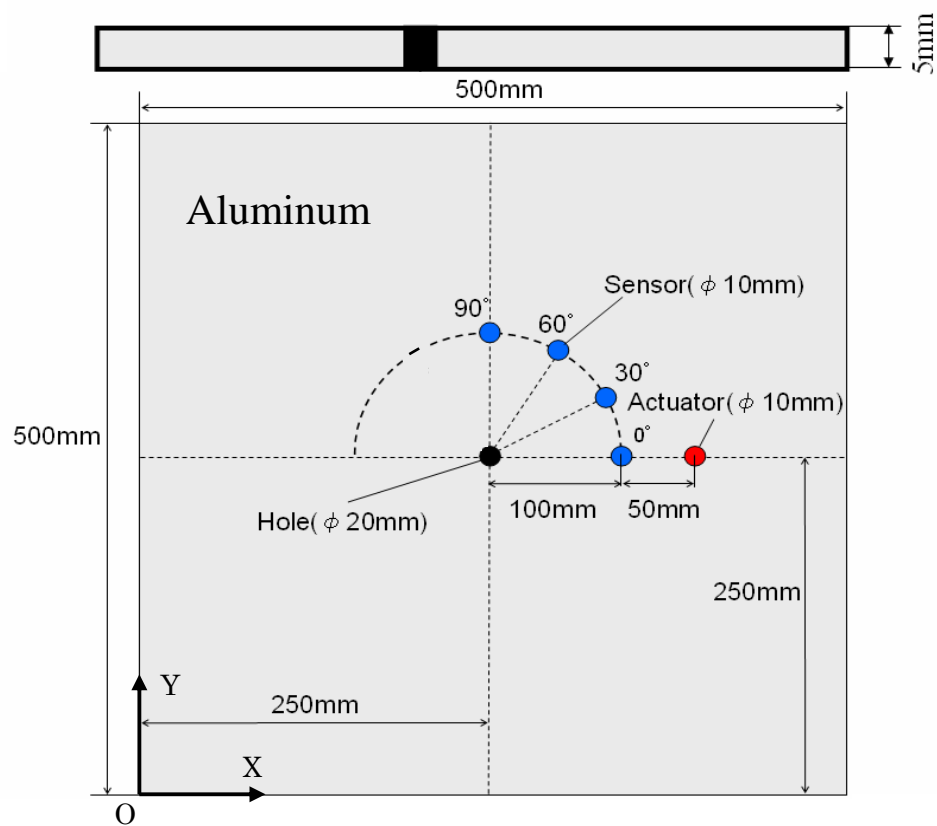


Figure 10. Schematic view of aluminum plate for FEM computation

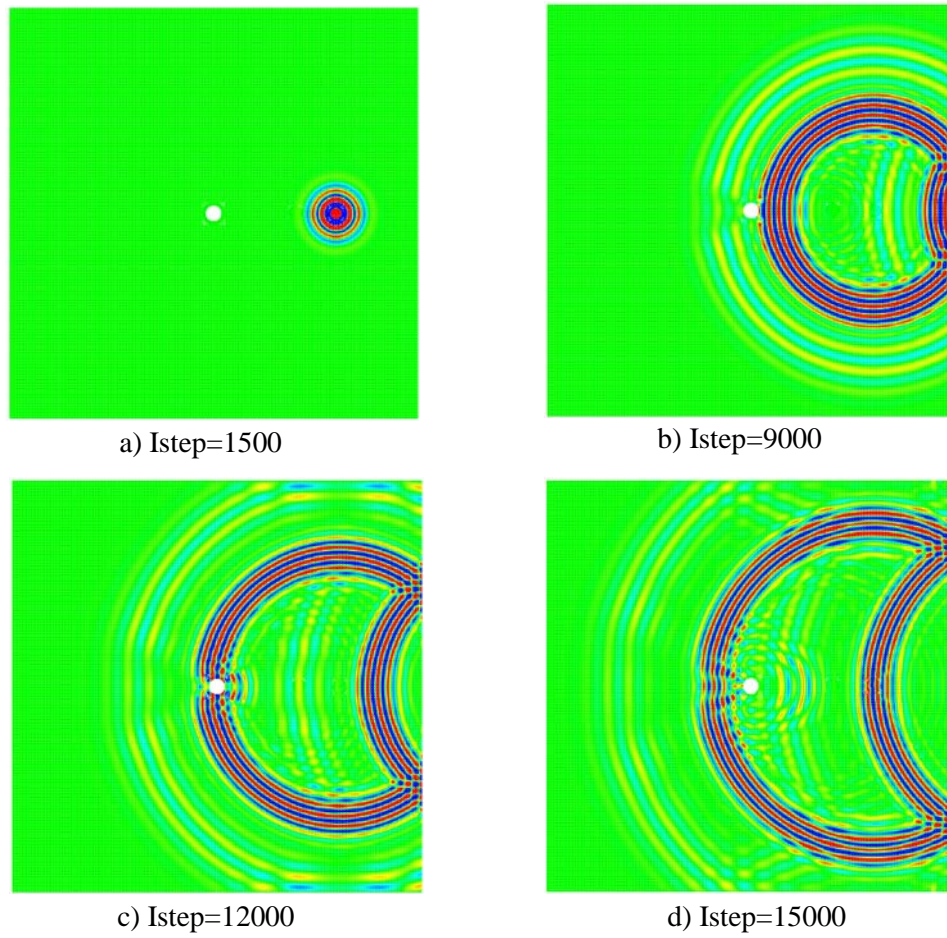


Figure 11. Configurations of wave propagation at various time steps

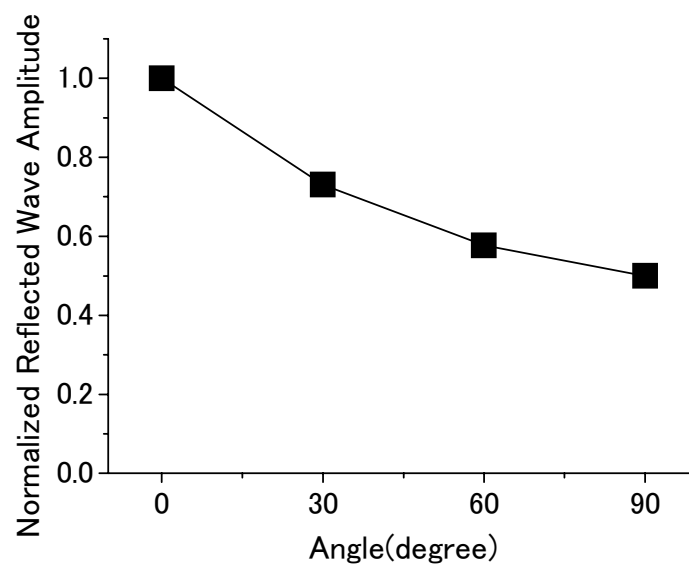
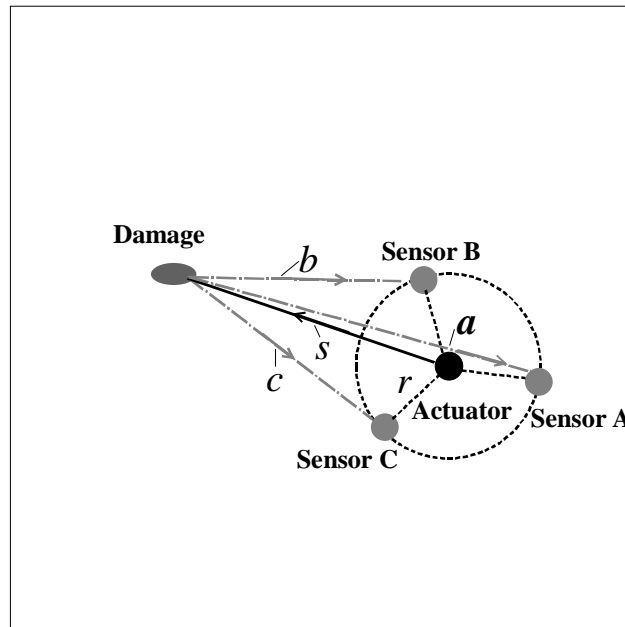
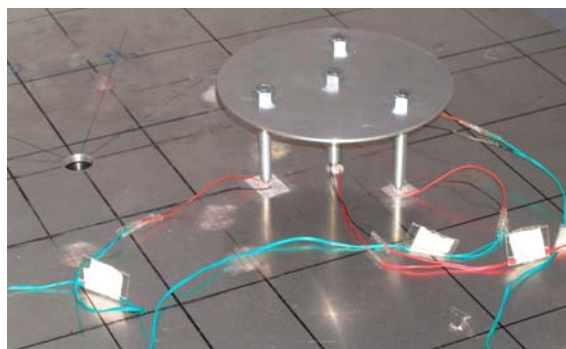


Figure 12. Normalized intensity of reflected wave from the hole versus angle of sensor



(a) Configuration of transducer set and damage



(b) A hand-made transducer set

Figure 13. A designed transducer set containing one actuator and three sensors

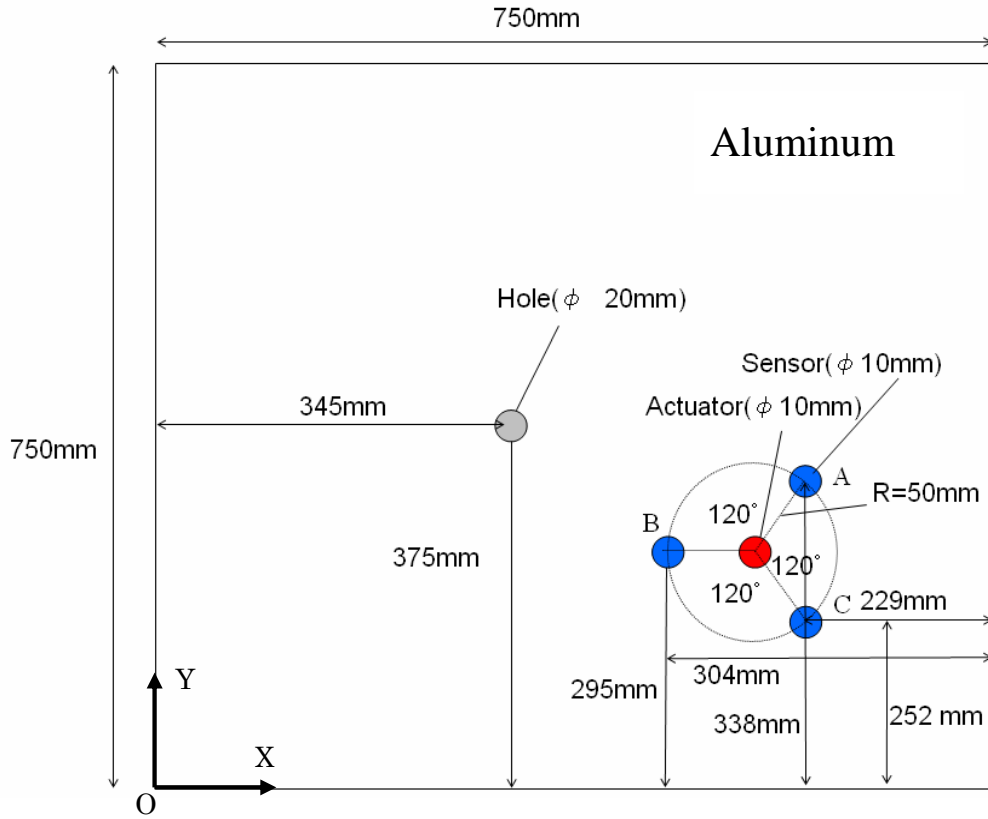


Figure 14. Schematic view of a plate with a hole and a transducer set

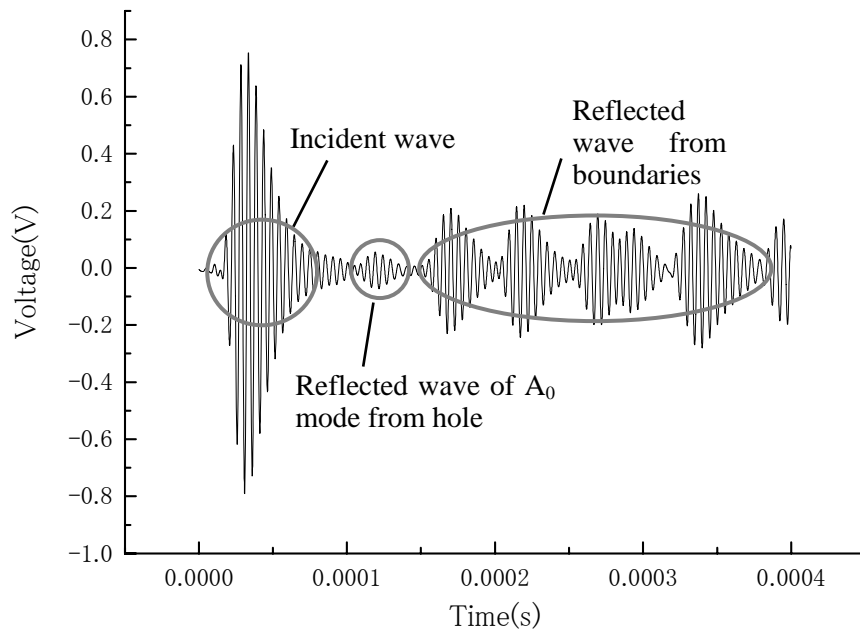


Figure 15. Signal of sensor B for a plate with a hole

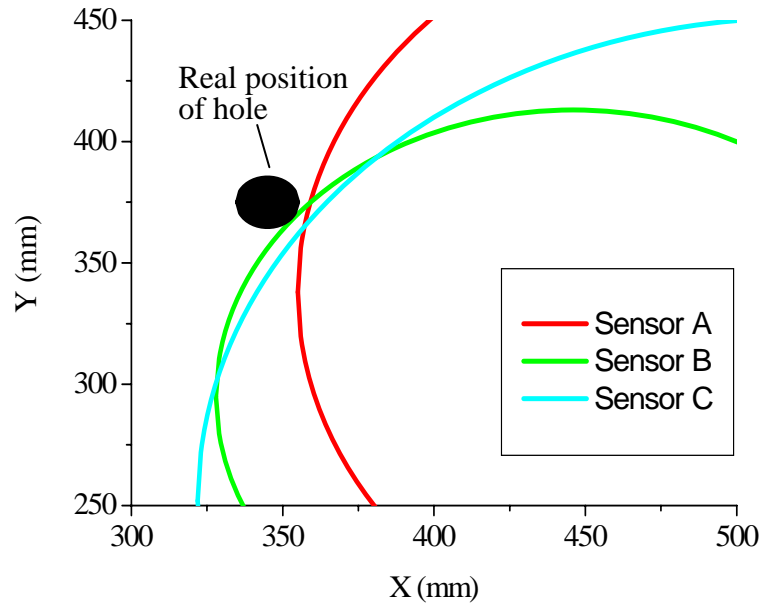


Figure 16. Identified position of hole using three circles

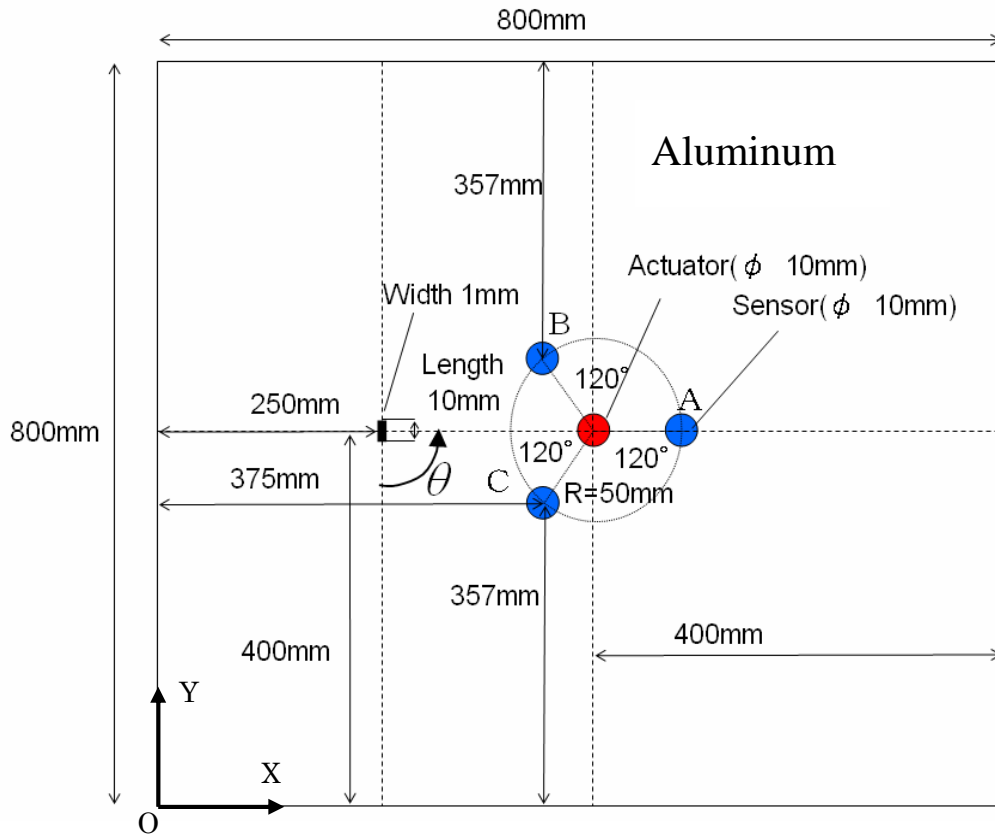


Figure 17. Schematic view of an aluminum plate with a transverse crack ( $\theta=90^\circ$ )

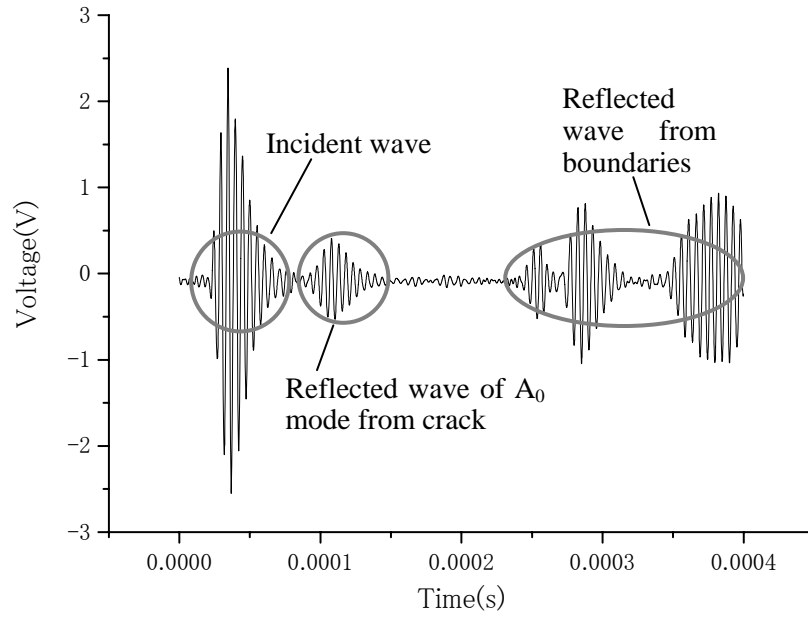
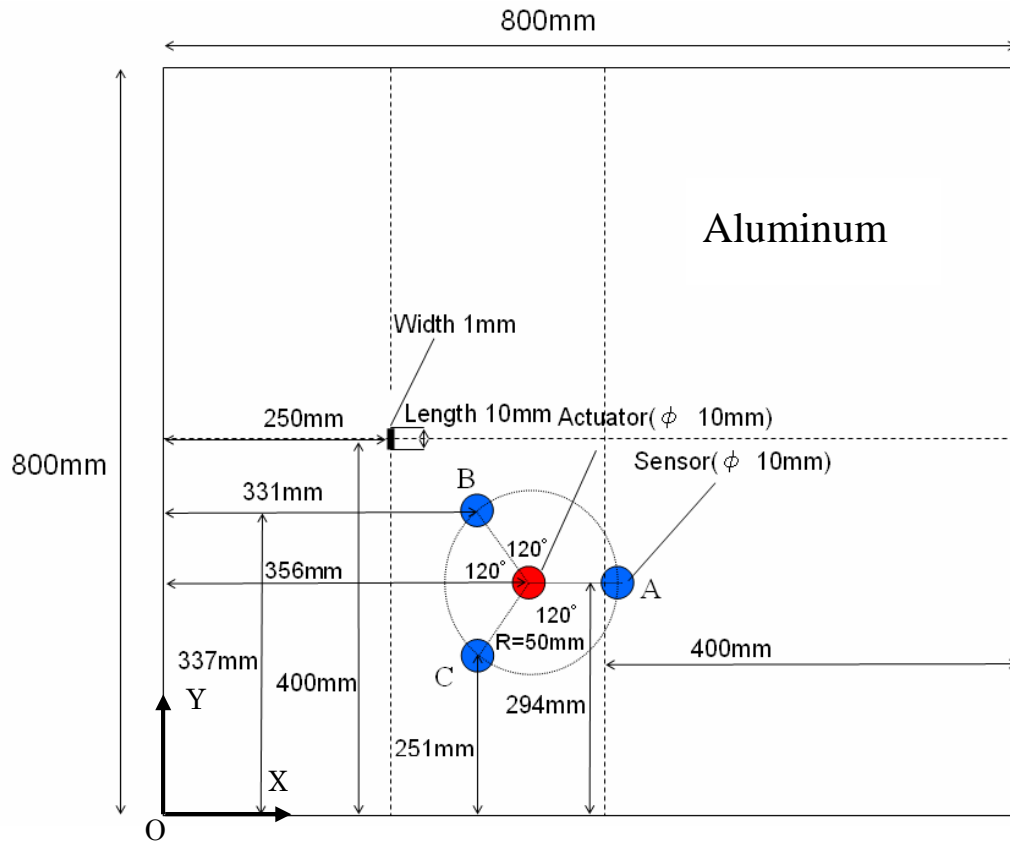


Figure 18. Signal of sensor C for a plate with a crack

Figure 19. Schematic view of an aluminum plate with a transverse crack ( $\theta=45^\circ$ )



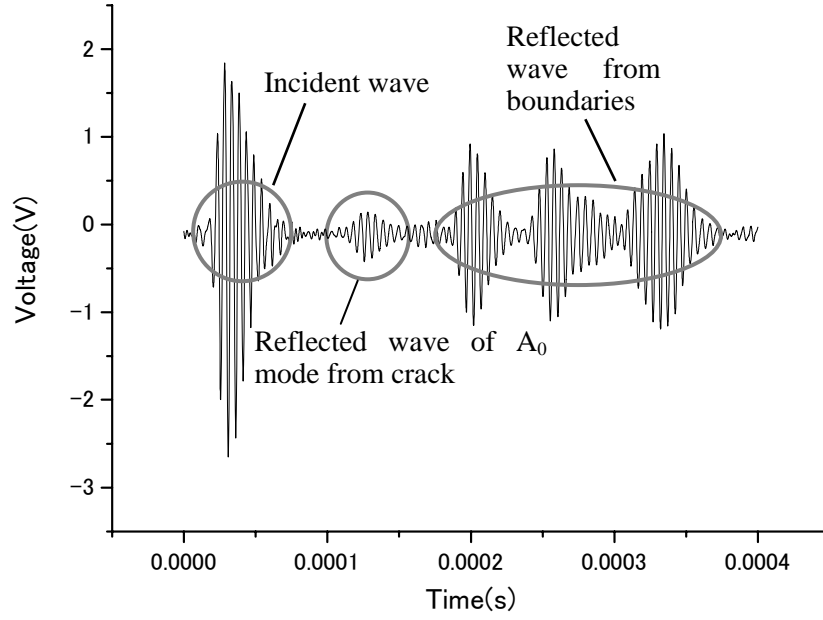


Figure 20. Signal of sensor A for a plate with a crack

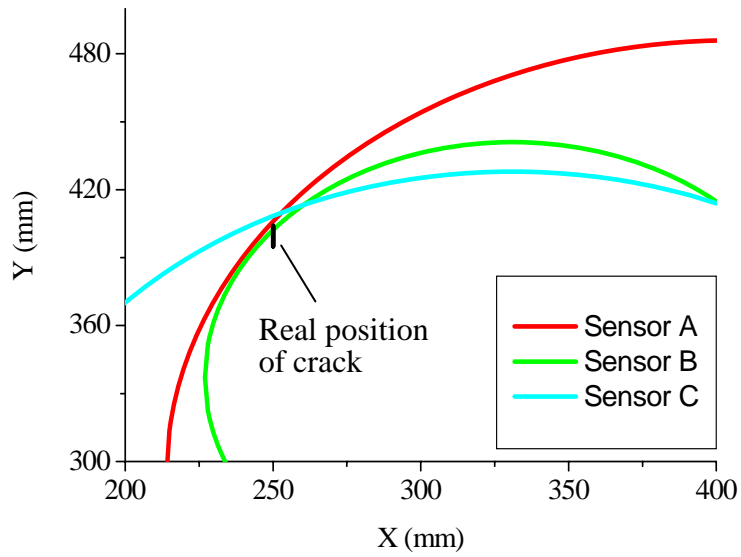


Figure 21. Identified position of crack using three circles when  $\theta=45^\circ$

Table 1. Material properties of aluminum

$E$ [GPa]	$\nu$	$\rho$ [kg/m <sup>3</sup> ]
68.9	0.3	2710

Table 2. Material properties of PZT

Young's Modulus [GPa]	Piezoelectric Coefficient [pC/N]
$E_{11}=E_{22}=62$	$d_{33}=472$
$E_{33}=49$	$d_{31}=d_{32}=-210$

Table 3. Results of identified crack position for 3 mm and 5 mm beams

	Thickness [mm]	Group velocity [m/s]	Arrival time [ms]	Position [mm]	Error [%]
Calculate	3	2068.5	0.354	1216.1	1.3
	5	2449.5	0.285	1199.1	0.1
Experimental	3	2068.5	0.349	1211.0	0.9
	5	2449.5	0.291	1206.4	0.5

Table 4. Ratio of amplitudes of  $S_0$  and  $A_0$  modes for various bonding conditions

	Actuator: Strong adhesive Sensor: Strong adhesive	Actuator: Grease lubricant Sensor: Strong adhesive	Actuator: Grease lubricant Sensor: Two-sided tape
$\frac{\text{Amplitude of } S_0 \text{ mode}}{\text{Amplitude of } A_0 \text{ mode}}$	1.20	0.25	0.14

Table 5. Experimental results of identified position of hole

	Correct values (mm)	Experimental (mm)	Error(%)
$s$	161	156	3.1
$a$	170	166	2.4
$b$	119	118	0.8
$c$	204	199	2.5

Table 6. Numerical results of identified position of hole

	Correct values (mm)	Experimental (mm)	Error(%)
<i>s</i>	161	160	0.6
<i>a</i>	170	162	4.7
<i>b</i>	119	133	11.8
<i>c</i>	204	201	1.5

Table 7. Experimental results of identified position of crack ( $\theta=90^\circ$ )

	Correct values (mm)	Experimental (mm)	Error(%)
<i>s</i>	150	143	4.7
<i>a</i>	200	200	0
<i>b</i>	132	126	4.5
<i>c</i>	132	134	1.5

Table 8. Experimental results of identified position of crack ( $\theta=45^\circ$ )

	Correct values (mm)	Experimental (mm)	Error(%)
<i>s</i>	150	154	2.7
<i>a</i>	189	192	1.6
<i>b</i>	103	104	1.0
<i>c</i>	170	177	4.1

Table 9. Experimental results of identified position of crack ( $\theta=22.5^\circ$ )

	Correct values (mm)	Experimental (mm)	Error(%)
<i>s</i>	150	150	0.0
<i>a</i>	175	168	4.0
<i>b</i>	101	93	7.9
<i>c</i>	185	193	4.3

# **Delamination detection of cross-ply laminated composite beams using $S_0$ Lamb mode**

Ning Hu <sup>1</sup>, Takahito Shimomukai <sup>1</sup>, Cheng Yan <sup>2</sup> and Hisao Fukunaga <sup>1</sup>

<sup>1</sup>*Department of Aerospace Engineering, Tohoku University, Aramaki-Aza-Aoba 6-6-01, Aoba-ku, Sendai 980-8579, Japan*

<sup>2</sup>*School of Engineering Systems, Queensland University of Technology, 2 George St. GPO Box 2434, Brisbane, QLD 4001, Australia*

The corresponding author's information:

Title: Associate Professor (Ning Hu)

Affiliation: Department of Aerospace Engineering, Tohoku University

Address: Aramaki-Aza-Aoba 6-6-01, Aoba-ku, Sendai 980-8579, Japan

E-mail: [hu@ssl.mech.tohoku.ac.jp](mailto:hu@ssl.mech.tohoku.ac.jp)

Web Page: <http://www.ssl.mech.tohoku.ac.jp/>

Running title: Delamination identification of cross-ply laminated beam

## Abstract

In this work, a Lamb wave based technique has been developed for delamination detection in cross-ply laminated beams. By measuring the propagation speed of  $S_0$  Lamb mode and the traveling time of a signal reflected from a delamination site, the location of the delamination can be identified. It has been also confirmed by the experiment that the location of a delamination can be accurately determined by only using the data collected from the sensors in a defect-containing beam, without referring to the *baseline* signals. Finally, to gain a better understanding of the complex interaction between a Lamb wave and a long delamination, numerical simulations have been carried out using finite element method (FEM). The signal modes generated at the boundaries of the delamination have been analyzed.

Keywords: Non-destructive testing, polymer-matrix composites, delamination, Finite element analysis, smart materials

## 1. Introduction

Recently, Lamb waves have been increasingly used in structural health-monitoring in various engineering structures. Consequently, some relevant techniques for detecting delaminations in composite laminates have been developed [1-3]. Among these techniques, a two-stage model has been commonly adopted by which the difference between the signals from a defective structure and an intact structure can be used to define the so called *residual error*. Generally, these signals generated were complex in nature, featured by different group speed, amplitude of wave, etc. [1-3]. Therefore, *baseline* signals acquired from an intact structure are essential for calibration and delamination detection in these techniques, especially for monitoring the propagation of a damage with high accuracy. Also, tremendous effort has been put to the delamination identification, which could be treated as a problem of inverse pattern recognition using calibrated numerical methods such as artificial neural network [4]. The interaction between Lamb waves and delaminations has also been investigated numerically and theoretically [5-7]. However, the complex wave scattering phenomenon in a delamination area has not been clearly understood in these studies. Also, it is still difficult to identify the accurate location of a delamination area, where the strongest and observable wave is assumed to be reflected back to the sensors.

In this study, a technique for delamination identification using  $S_0$  Lamb mode,

without referring to the baseline data, has been developed. Through measuring the propagation speed of a wave and the traveling time of a reflected  $S_0$  mode from a delamination, the delamination position can be accurately identified. Moreover, to understand the complex interaction of  $S_0$  mode with a long delamination, the numerical simulations have been carried out.

## 2. Experiments and numerical analyses

### 2.1 Materials and experimental procedure

As shown in Fig. 1, a CFRP laminated composite beam of stack sequence of  $[0_{10}/90_{12}/0_{10}]$  was used. Delaminations with different lengths, i.e., 30 mm, 20 mm and 10 mm, respectively, were intentionally created at the interface between the 10<sup>th</sup> and 11<sup>th</sup> plies by inserting a Teflon film with a thickness of  $25 \mu\text{m}$ . A PZT actuator was attached on the top surface of the left end of the beam. The PZT actuator had a diameter of 10 mm and a thickness of 0.5 mm. In this case, the following generated waves from the actuator merged into the reflected waves from the left end of beam, which leads to a simpler signal.

$$P(t) = \begin{cases} 0.5[1 - \cos(2\pi ft / N) \sin(2\pi ft)], & t \leq N / f \\ 0, & t > N / f \end{cases} \quad (1)$$

where  $f$  is the central frequency in Hz and  $N$  is the number of sinusoidal cycles within a pulse. In this experiment, the signal with  $f=100$  kHz and  $N=5$  was used and the electrical voltage on the actuator was 10 V.

The same PZT unit was used as a sensor to pick up the reflected wave from a

delamination. Its material properties are:  $E_{11}=62$  GPa,  $E_{33}=49$  GPa,  $d_{33}=472$  pC/N, and  $d_{31}=-210$  pC/N. In this study,  $S_0$  mode was employed because its propagation speed is much higher than that of  $A_0$  mode, confirmed as 4 times higher from our testing. Therefore, it is expected that in a specified time domain, no  $A_0$  mode will be collected due to its slow speed, making the analysis of  $S_0$  modes much easier. Without the baseline data, it is still easy to estimate the arrival of the reflections from the beam boundaries, provided that the wave propagation speed and the dimensions of the beam are known. Then, if the reflected blob from the delamination is not overlapped with the reflections from the boundaries, it can be simply collected by the sensor. It is still a technical challenge when the delamination is located close to the beam boundaries and the reflected blob of the delamination is completely overlapped with the reflections from the boundaries.

## *2.2 Finite element analysis procedure*

To explore the interaction of  $S_0$  mode with the delamination, a three-dimensional hybrid element proposed by the authors [8] and the explicit time integration algorithm were used in the finite element simulations. The contact effects in the delamination area were neglected. The same signal stated in Eq. (1) was also used here. Furthermore, the actuator and the sensor were discretized using 3D brick elements with a proper constitutive law. If an electrical field is applied on the actuator on the top surface of the beam, it will stretch or contract along the length direction, which can result in axial force and bending moment



in the beam simultaneously. Then, both  $S_0$  and  $A_0$  modes can be automatically generated.

### 3. Results and discussion

#### 3.1 Experimental analysis

Firstly, to evaluate the wave propagation speed, an intact beam with two sensors attached, was employed. The distance between the two sensors was 420 mm. By using the wavelet transformation technique [9], the arrival times of the incident waves to the two sensors were determined and the wave propagation speed of  $S_0$  mode at  $f=100$  kHz was estimated as 6210 m/s. To verify the experimental results, the theoretical wave speed of the  $S_0$  mode was estimated based on the transfer matrix method [10]. The calculated speed was 6467 m/s if the material properties of CFRP were taken as  $E_{11}=115$  GPa,  $E_{22}=E_{33}=9$  GPa,  $G_{12}=G_{23}=G_{13}=3$  GPa,  $\nu_{16}=0.016$ ,  $\nu_{23}=0.45$ ,  $\nu_{31}=0.32$  and  $\rho=1600$  kg/m<sup>3</sup>. On the other hand, the corresponding propagation speed of  $A_0$  mode was estimated as 1506 m/s, much lower than the  $S_0$  mode. The higher theoretical wave speed of  $S_0$  mode may be due to the transfer matrix method used here, which is actually for an infinite plate. For a beam with a finite width, the influences of Poisson's ratio and boundary conditions are expected.

A comparison of the signals from an intact beam and a delaminated one (a 30 mm delamination) is shown in Fig. 2. It is clear that there is a reflected wave in the signals from the delaminated beam, which is located between the incident and the reflected waves. However, no clear reflected wave could be detected when the delamination length was

reduced to 10 mm. No  $A_0$  mode can be observed in Fig. 2, since its incident wave is not fast enough to reach the sensor within 300  $\mu\text{s}$ . For a signal with  $f=100$  kHz and  $N=5$ , the minimum detectable length of the delamination was 20 mm, which is about 1/3 of the wavelength of the  $S_0$  mode at 100 kHz. It is reasonable to assume that a higher excitation frequency may have the benefit of detecting smaller delaminations. Once the arrival time of a reflected wave from the delamination is determined, the difference between the arrival times of the incident and reflected waves can be used to detect the delamination position, as shown in Fig. 3. For the 20 mm long delamination, a slightly higher error in the delamination position is observed. The reason is the overlap between the reflected signals from the delamination and those from the right end of the beam, causing an increased error in determination of the arrival time of a reflected wave from the delamination.

### *3.2 Numerical simulation*

A comparison between the experimental result and numerical simulation is shown in Fig. 4. A good agreement between the experimental results and the simulation is observed. For convenience, the amplitude of the first arrival  $S_0$  mode in the simulated waves was calibrated using the experimental data. The attenuation coefficients of the CFRP in the numerical model were determined by matching the amplitudes of the reflected waves from the right end of the beam to the experimental data. When the actual sensor thickness, i.e., 0.5 mm, was used in numerical simulations, a small reflected wave from the sensor could

be observed immediately next to the incident wave. This was also confirmed by the experimental result. Corresponding to a 0.05 mm sensor thickness, however, no obvious reflection from the sensor could be observed in the numerical simulation. Therefore, the sensor thickness of 0.05 mm was eventually chosen in the simulations. Note that the selection of sensor thickness does not affect the simulation results as the calculated amplitudes will be calibrated using the experimental data. Similar to the experimental results, the numerical simulation showed that the reflected wave from the 10 mm delamination was very weak.

To understand the effect of delamination position along the through-thickness direction on the propagation of a Lamb wave, a 30 mm delamination was created in the midplane, i.e., between the 16th and the 17th plies. With the signal of  $f=80$  kHz and  $N=5$ , the comparison between the numerical and experimental results is shown in Fig. 5. In Fig. 5, no obvious reflected waves from the delamination can be observed. This finding is consistent with the work of Guo *et al.* [5]. They showed that the delamination at the positions of zero shear stress along the through-thickness direction, such as the midplane of a beam had no effect on Lamb wave propagation in a  $S_0$  mode.

To examine the capability of the numerical simulation to identify the location of a delamination, the length of delamination  $L$  (Fig. 6(a)) was increased from 30 to 90 mm. The length of the beam was also increased up to 1500 mm. Under a condition of  $f=100$

kHz and  $N=5$ , the propagation speed of  $S_0$  mode was firstly calculated in an intact beam with two sensors. The estimated propagation speed was 6260m/s, which is very close to the experimental measurement. Based on this speed, the numerically identified positions for various delamination lengths are shown in Fig. 6(b). It is surprising to note that all predicted positions are beyond the right end of the delaminations. It has been demonstrated that a higher propagation speed of  $S_0$  mode in the delaminated  $0^\circ$  layer can make the predicted delamination positions behind the actual delaminations [1, 3]. From the FEM simulations, the estimated speed of  $S_0$  mode in the  $0^\circ$  delaminated layer was 8483 m/s. If we use this speed in the delaminated region only (in the intact region, we still use 6260 m/s), with the known left end of the delamination, the predicted delamination positions or the reflected positions of  $S_0$  mode are shown in Fig. 6(c). Comparing it with Fig. 6(b), we can find that there is no obvious difference in the delamination positions for short delaminations, e.g. 30 and 50 mm. However, for a longer delamination (70 and 90 mm), an increased deviation from the actual delamination is observed when 8483 m/s was used in the prediction. It implies that the use of the actual wave speed in the delamination area can not improve the prediction and a reflected wave with observable intensity is normally from the right end of the delamination.

To gain a better understanding of this complex interaction, a beam with a length of 1500 mm and a 200 mm long delamination was examined using the numerical simulation.

Under a condition of  $f=100$  kHz and  $N=5$ , the wave signals corresponding to different time domains are shown in Fig. 7. The transverse deflections at various mesh points on the top surface of the beam were used. Fig. 7 also shows the subtraction between the wave signals from the intact and the delamination-containing beams, which can amplify the scattered wave signals from the delamination. The typical sensor signal for accurately evaluating the arrival times of various waves is shown in Fig. 8.

At the time domain of  $139 \mu\text{s}$ , the  $S_0$  mode arrives at the left end of the delamination and then reflects from or transmits from the left end, as shown Fig. 7 (a) and Fig. 7(b), respectively. At  $182 \mu\text{s}$ , the  $S_0$  mode passes through the right end of the delamination, Fig. 7(c). Fig. 7(d) shows two separate reflected modes, i.e.,  $A_0$  and  $S_0$  from the left end of the delamination. In principle, it is easy to distinguish a  $S_0$  from an  $A_0$  mode by the propagation speed and wave length. However, the amplitude of the reflected  $S_0$  mode is smaller than that of the  $A_0$  mode. This can be explained by the fact that the bending deformation in a laminated beam is much higher as compared to the axial deformation. Also, when the  $S_0$  mode travels through the left end of delamination, a new transmitted  $A_0$  mode is generated, Fig. 7(d). The reflected waves from the right end of the delamination, consisted both  $A_0$  and  $S_0$  modes, can be also observed in Fig. 7(d). Corresponding to  $236 \mu\text{s}$ , the incident  $A_0$  mode from the actuator does not reach the sensor, Fig. 7(e). The reflected  $S_0$  mode from the left side of the delamination has already passed through the

sensor, Fig. 7(f). However, at the same time point in Fig. 8, this reflected  $S_0$  mode cannot be detected by the sensor due to its small amplitude. Also, the reflected  $S_0$  mode from the right end of the delamination, which is surpassing the reflected  $A_0$  mode from the left end of the delamination, can be observed, as shown in Fig. 7(f). A new transmitted  $A_0$  mode and the transmitted  $S_0$  mode from the right end of the delamination can be clearly observed, Fig. 7(f). At 303  $\mu\text{s}$ , as shown in Fig. 7(g), the incident  $A_0$  mode does not arrive at the sensor. As indicated in Fig. 7(h), the reflected  $S_0$  mode from the right end of the delamination completely surpasses the reflected  $A_0$  mode from its left end. This reflected  $S_0$  mode has already passed through the sensor position. From Fig. 8, the arrival time of the reflected wave from the delamination is identified as around 275  $\mu\text{s}$ . The reflected wave actually arrives at the sensor between the time points shown in Figs. 7(f) and 7(h), i.e., 236  $\mu\text{s}$  and 303  $\mu\text{s}$ . Therefore, the reflected wave signal detected clearly by the sensor is considered to be the reflected  $S_0$  mode from the right end rather than the left end of the beam, due to its higher intensity. Based on the numerical simulations above, the very complex interaction between the different signal modes and the boundaries of a delamination can be identified. When only a single  $S_0$  mode passes through a delamination, four modes will be generated at one end of the delamination, including two transmitted  $A_0$  and  $S_0$  modes, and two reflected  $A_0$  and  $S_0$  modes. However, the reflected  $S_0$  mode received by a sensor is from the right end of the delamination. Further study is required to

understand why the stronger reflections are from the right end of a delamination. One possible explanation is that the delaminated region is of lower bending stiffness, which can be considered to be a softer region. When a wave propagates from a harder or intact region into a softer region, the reflections become weak. In contrast, when the wave propagates from a softer region into a harder one, a stronger reflection is expected.

#### **4. Conclusions**

In this work, by using  $S_0$  Lamb mode, a technique for identifying a delamination in cross-ply laminated composite beams has been developed. The delamination position can be identified if the arrival time of a reflected wave from a delamination and the wave propagation speed of  $S_0$  mode are known. One of the advantages of this approach is the baseline data acquired from intact beams are not required. Extensive finite element simulations have been conducted to investigate the interaction of  $S_0$  mode with various delaminations. It has been found that when a single  $S_0$  mode passes through two ends of a delamination, four modes will be generated at even one end, i.e., reflected  $A_0$  and  $S_0$  and transmitted  $A_0$  and  $S_0$  modes. When a single  $S_0$  mode propagates into a delamination, reflected  $S_0$  mode with high amplitude is generated from the end point of the delamination where the waves propagate out, suitable for sensor detection in practice.

#### **Acknowledgements**

This work is partly supported by the Award from AFOSR numbered by AOARD-06-4066 and Natural Science Foundation Project of CQ CSTC.

## References

- [1] Toyama N, Noda J, Okabe T. Quantitative damage detection in cross-ply laminates using Lamb wave method. *Compos Sci and Technol* 2003, 63: 1473-79.
- [2] Rosalie SC, Vaughan M, Bremner A, Chiu WK. Variation in the group velocity of Lamb waves as a tool for the detection of delamination in GLARE aluminium plate-like structures. *Compos Struct* 2004; 66: 77-86.
- [3] Takeda N, Okabe Y, Kuwahara J, Kojima S, Ogisu T. Development of smart composite structures with small-diameter fiber Bragg grating sensors for damage detection: Quantitative evaluation of delamination length in CFRP laminates using Lamb wave sensing. *Compos Sci Technol* 2005; 65: 2575-87.
- [4] Su Z, Yang C, Pan N, Ye L, Zhou LM. Assessment of delamination in composite beams using shear horizontal (SH) wave mode. *Compos Sci Technol* 2007; 67: 244-51.
- [5] Guo N, Cawley P. The interaction of Lamb waves with delaminations in composite laminates. *J Acoust Soc Am* 1993; 94: 2240-6.
- [6] Wang CH, Rose LRF. Wave reflection and transmission in beams containing delamination and inhomogeneity. *J Sound & Vibration* 2003; 264: 851-72.
- [7] Mahapatra DR, Gopalakrishnan S. A spectral finite element model for analysis of axial–flexural–shear coupled wave propagation in laminated composite beams. *Compos Struct* 2003; 59: 67-88.
- [8] Cao YP, Hu N, Lu J, Fukunaga H, Yao ZH. A 3D brick element based on Hu-Washizu variational principle for mesh distortion. *Int J Numer Meth Engrg* 2002; 53: 2529-48.
- [9] Jeong H, Jang YS. Wavelet analysis of plate wave propagation in composite laminates. *Compos Struct* 2000; 49: 443-50.
- [10] Nayfeh AH, Chimenti DE. Elastic wave propagation in fluid-loaded multi-axial anisotropic media. *J Acoust Soc Am* 1991; 89: 542-9.



### Captions of Figures

Figure 1. Schematic view of delaminated beam with actuator and sensor (unit: mm)

Figure 2. Comparison between signals of delaminated and intact beams (a 30 mm delamination between the 10<sup>th</sup> and the 11<sup>th</sup> plies)

Figure 3. Delamination positions identified experimentally

Figure 4. Comparison of experimental and numerical results for a 30 mm delamination between the 10<sup>th</sup> and the 11<sup>th</sup> plies

Figure 5. Comparison of experimental and numerical results for a 30 mm delamination at the mid-plane between the 16<sup>th</sup> and the 17<sup>th</sup> plies

Figure 6. Numerical identification of positions of various delaminations: (a) schematic of the beam for numerical simulation (unit: mm); (b) results using 6260 m/s; (c) results using 8483 m/s in 0° delaminated layer

Figure 7. Wave signals of a beam with a delamination of length of 200 mm, and signal differences of intact and delaminated beams: (a) 139  $\mu$ s (wave signal of a delaminated beam); (b) 139  $\mu$ s (difference of wave signals of intact and delaminated beams); (c) 182  $\mu$ s (wave signal of a delaminated beam); (d) 182  $\mu$ s (difference of wave signals of intact and delaminated beams); (e) 236  $\mu$ s (wave signal of a delaminated beam); (f) 236  $\mu$ s (difference of wave signals of intact and delaminated beams); (g) 303  $\mu$ s (wave signal of a delaminated beam); (h) 303  $\mu$ s (difference of wave signals of intact and delaminated beams)

Figure 8. Sensor signal for a delamination of length of 200 mm

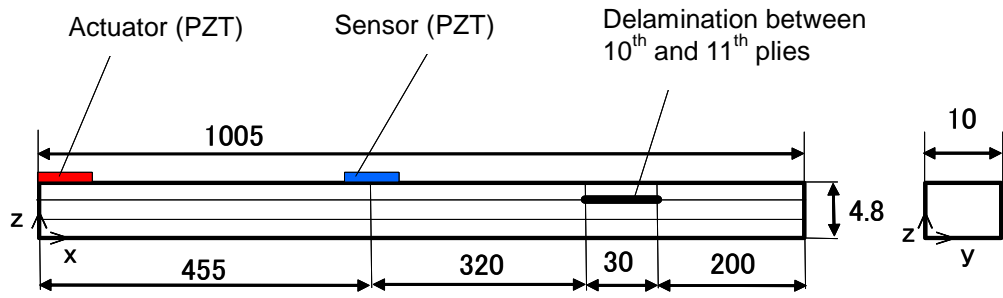


Fig. 1 Schematic view of delaminated beam with actuator and sensor (unit: mm)

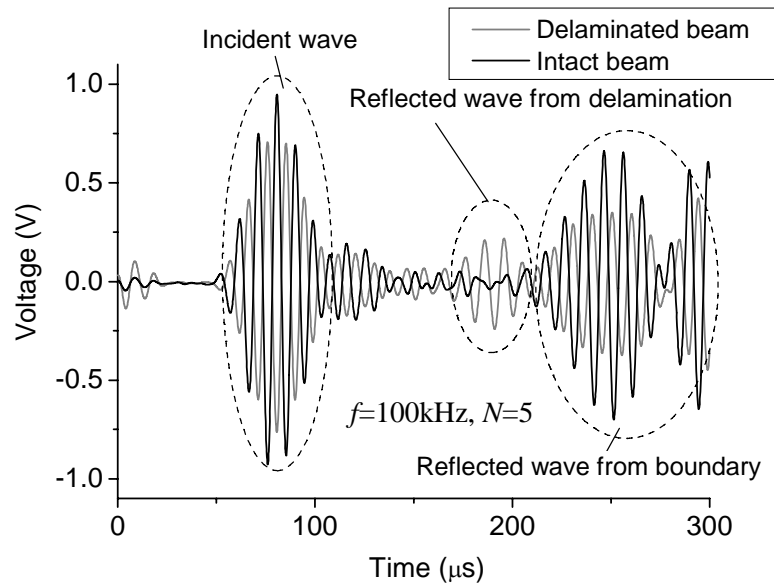


Fig. 2 Comparison between signals of delaminated and intact beams (a 30 mm delamination between the 10<sup>th</sup> and the 11<sup>th</sup> plies)

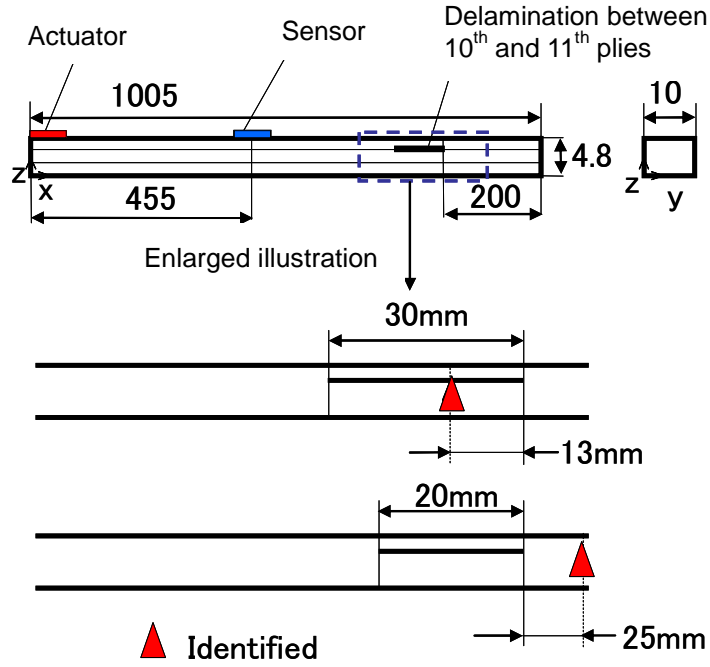
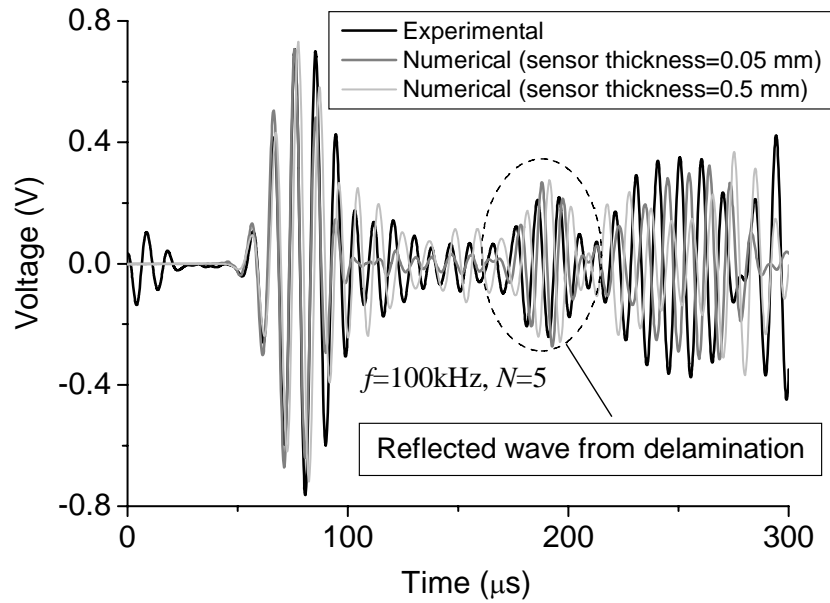


Fig. 3 Delamination positions identified experimentally

Fig. 4 Comparison of experimental and numerical results for a 30 mm delamination between the 10<sup>th</sup> and the 11<sup>th</sup> plies

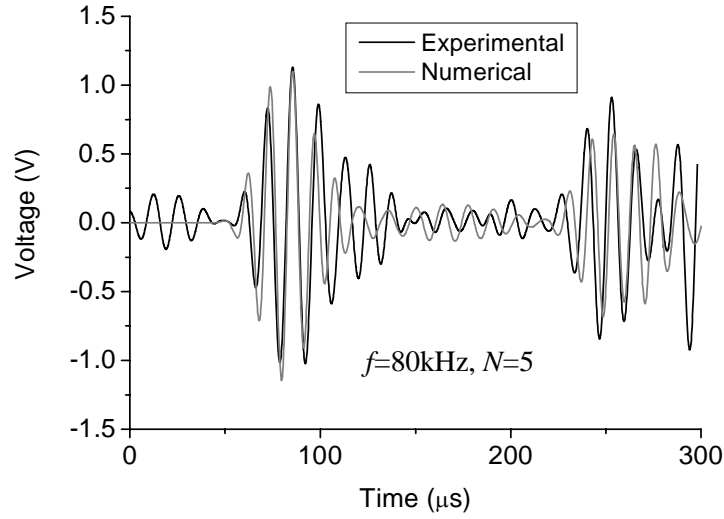
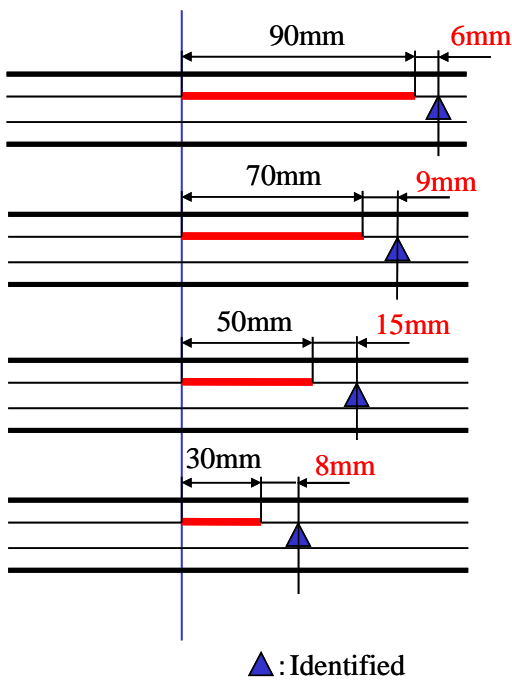
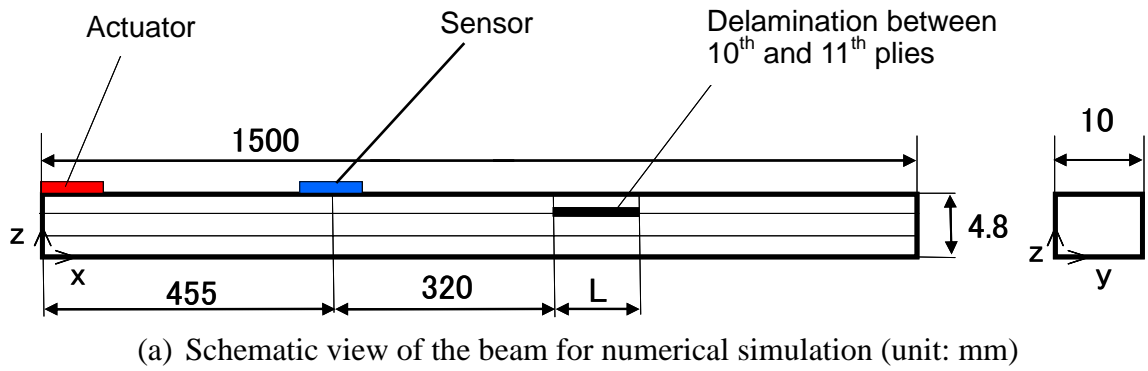
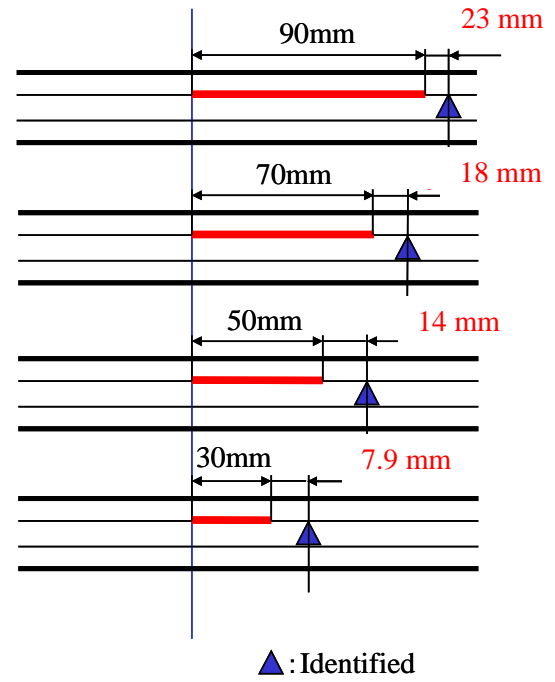


Fig. 5 Comparison of experimental and numerical results for a 30 mm delamination at the mid-plane between the 16<sup>th</sup> and the 17<sup>th</sup> plies

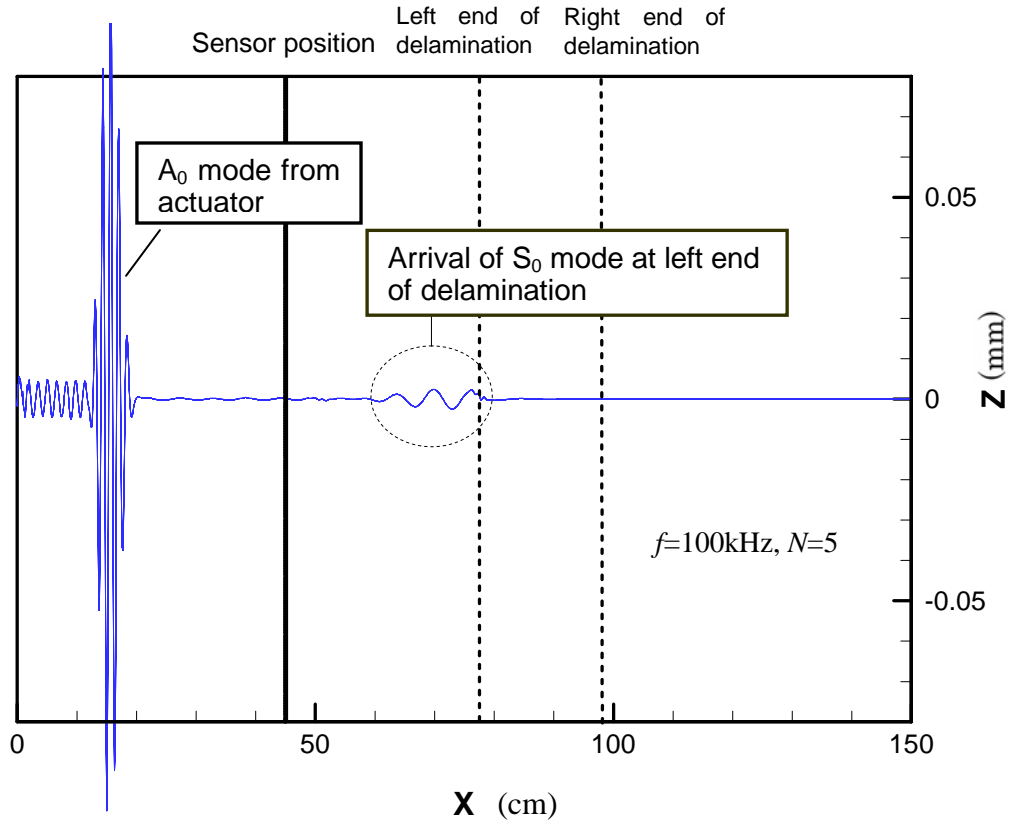
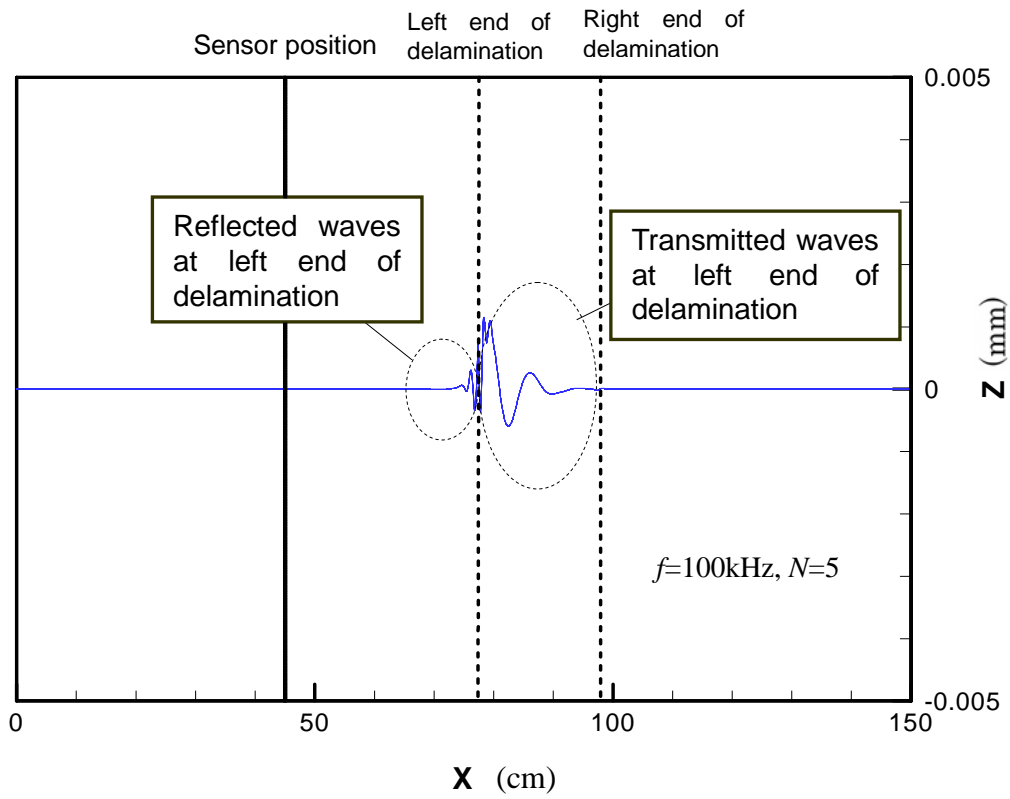


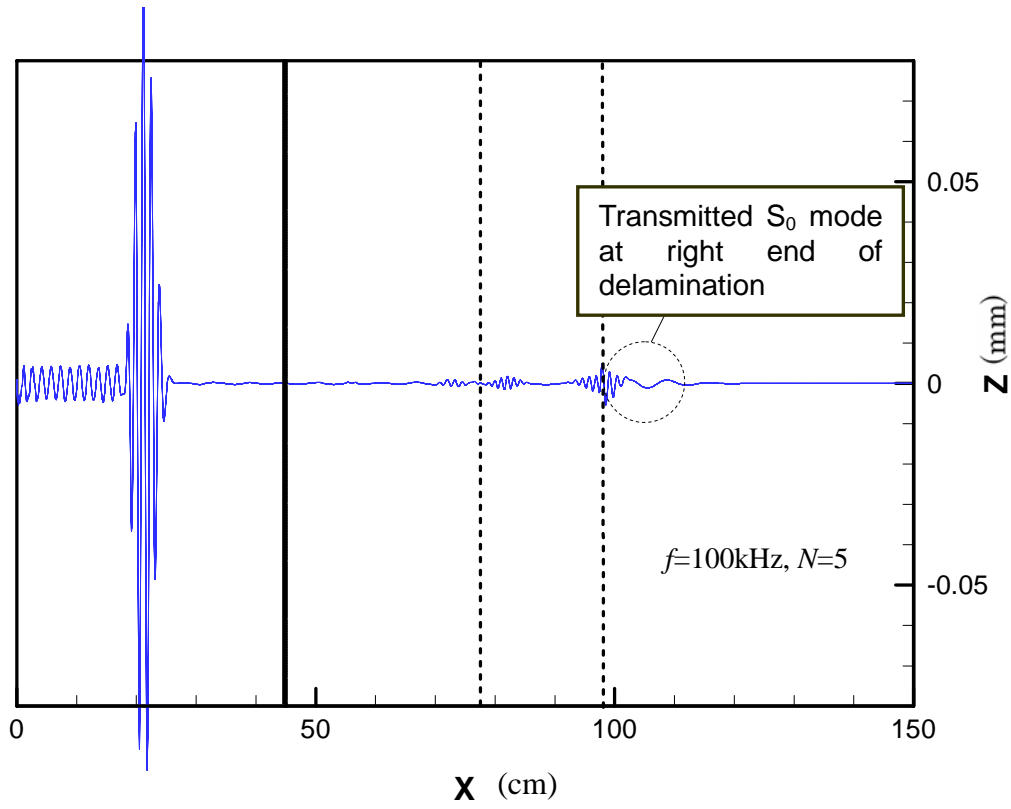
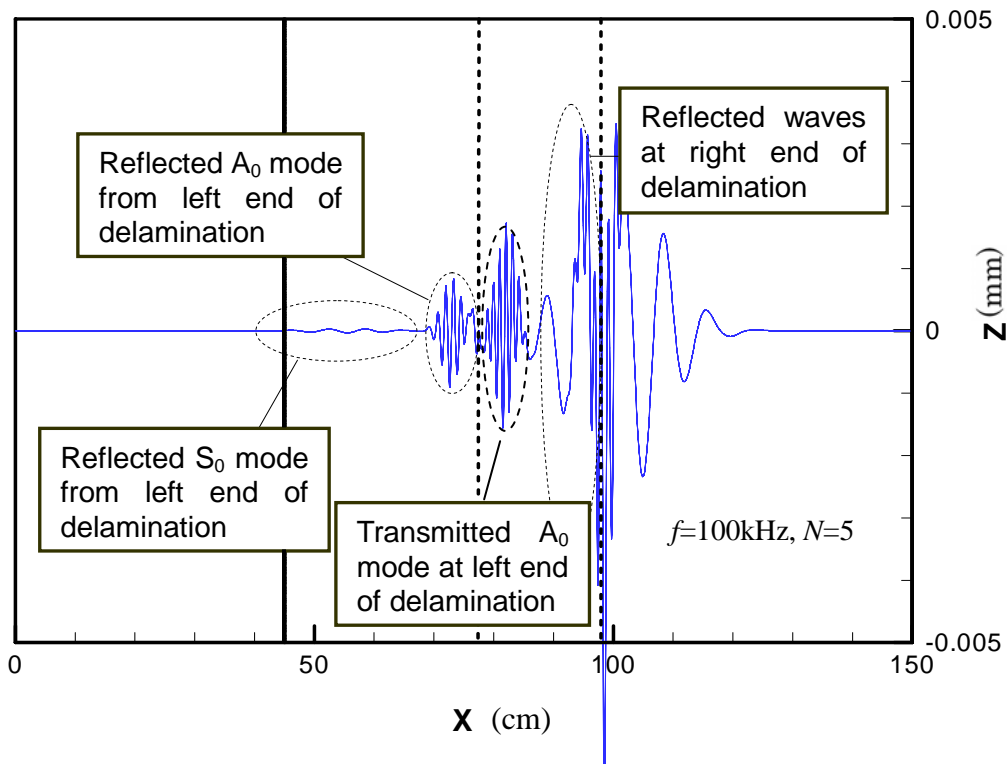
(b) Results using 6260 m/s

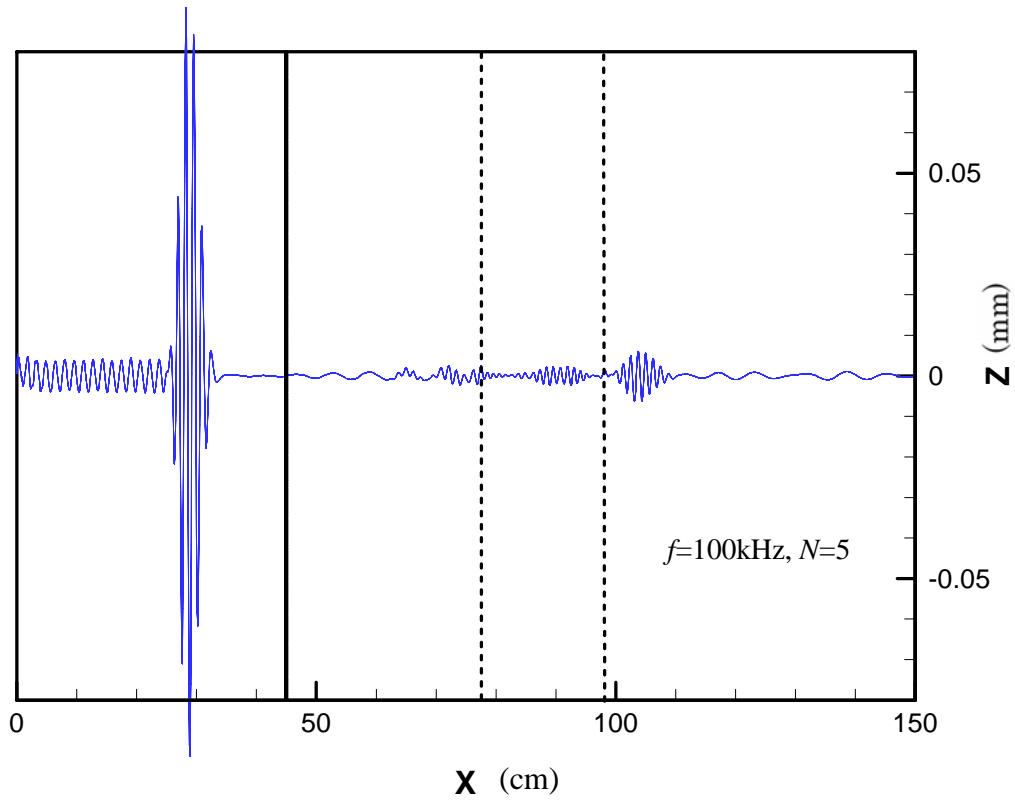
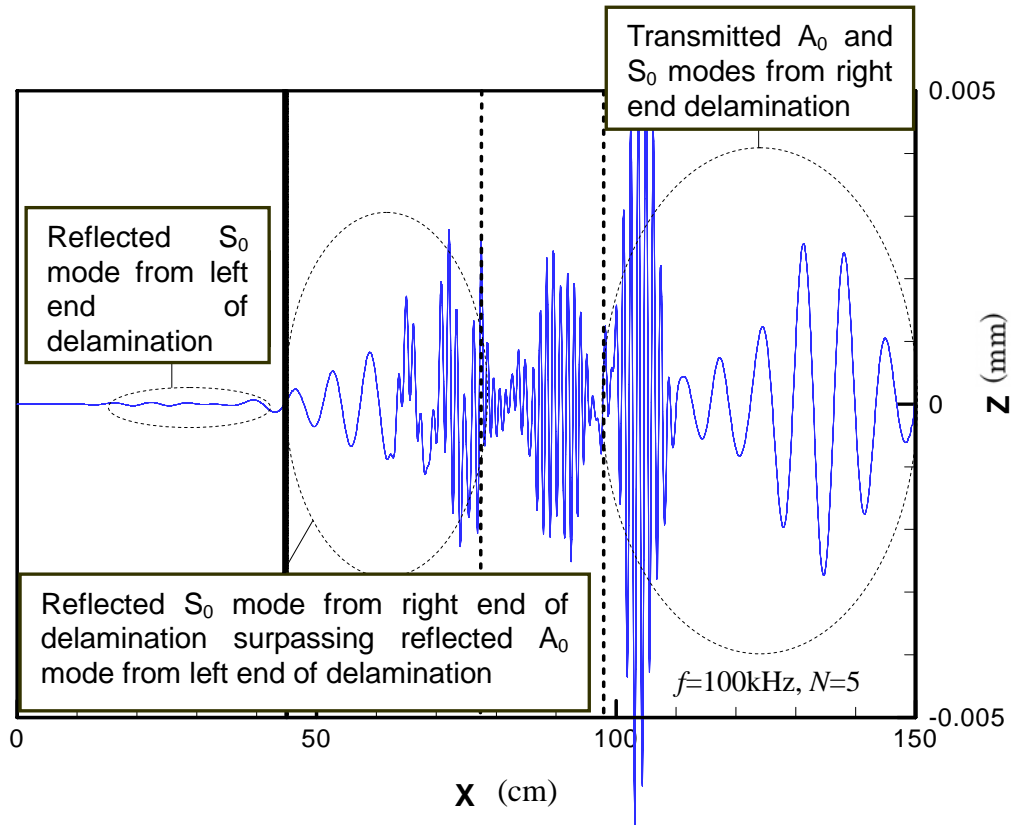


(c) Results using 8483 m/s in 0° delaminated layer

Fig. 6 Numerical identification of positions of various delaminations

(a) 139  $\mu\text{s}$  (wave signal of a delaminated beam)(b) 139  $\mu\text{s}$  (difference of wave signals of intact and delaminated beams)

(c)  $182 \mu\text{s}$  (wave signal of a delaminated beam)(d)  $182 \mu\text{s}$  (difference of wave signals of intact and delaminated beams)

(e)  $236 \mu\text{s}$  (wave signal of a delaminated beam)(f)  $236 \mu\text{s}$  (difference of wave signals of intact and delaminated beams)

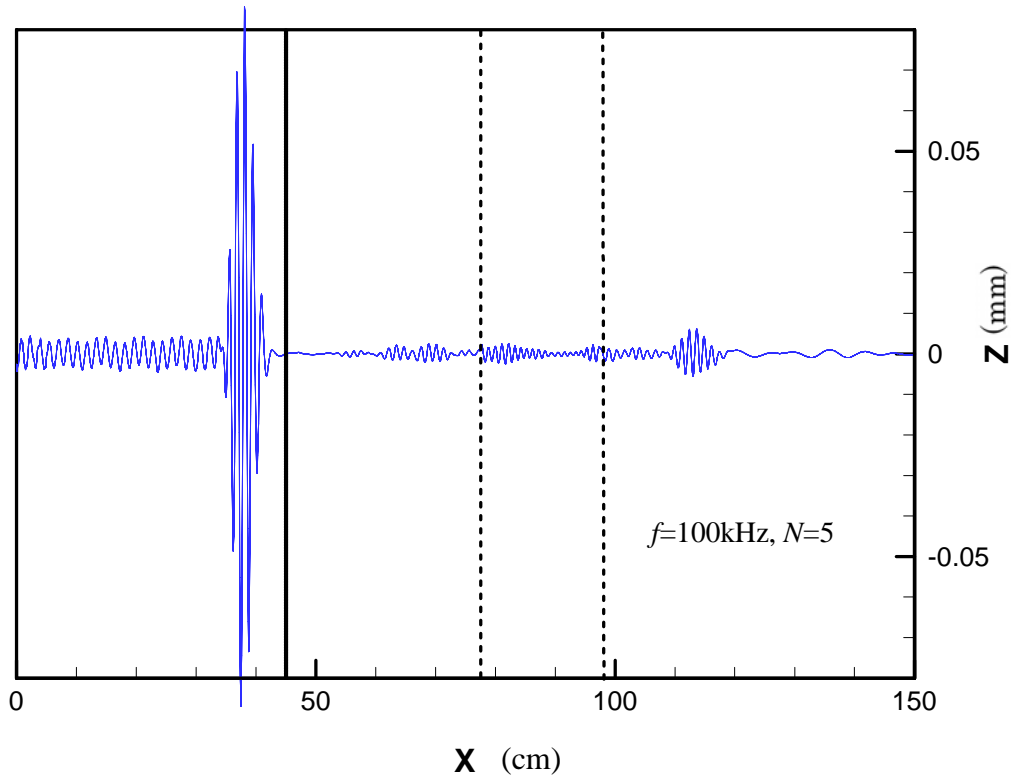
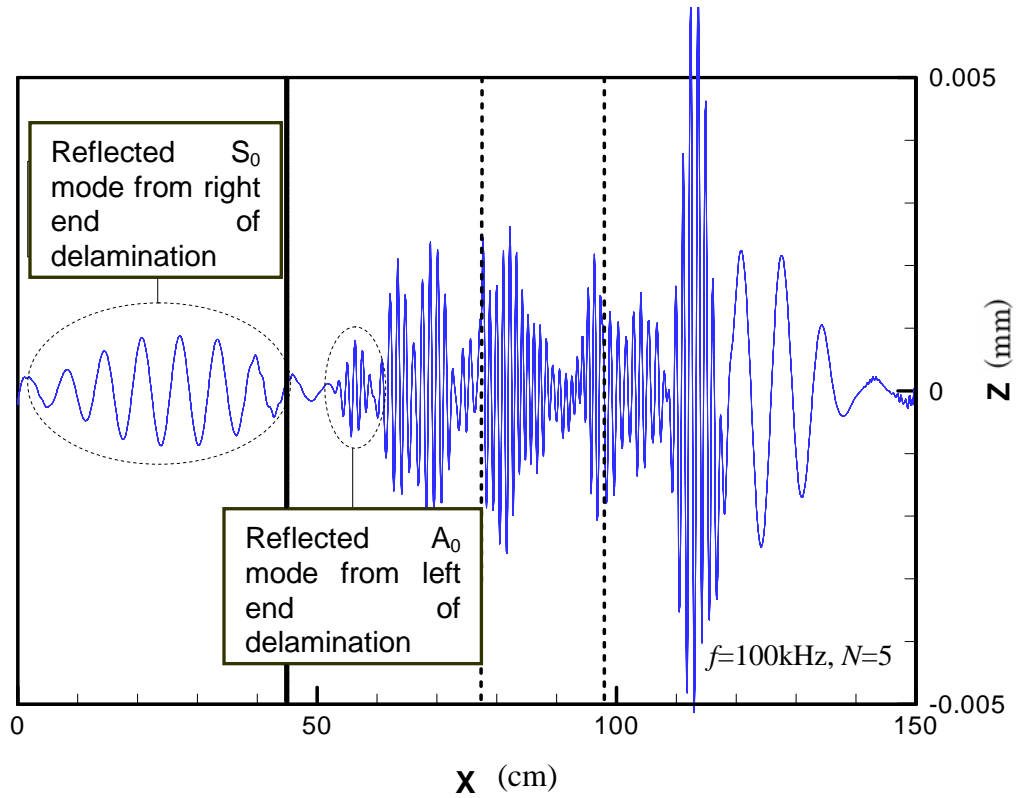
(g)  $303 \mu\text{s}$  (wave signal of a delaminated beam)(h)  $303 \mu\text{s}$  (difference of wave signals of intact and delaminated beams)

Fig. 7 Wave signals of a beam with a delamination of length of 200 mm, and signal differences of intact and delaminated beams



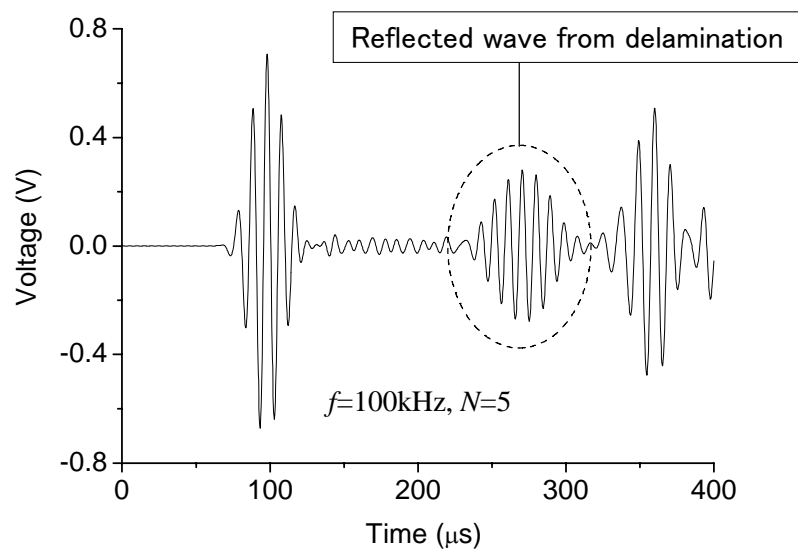


Fig. 8 Sensor signal for a delamination of length of 200 mm